Gaia-ESO Survey: Empirical classification of VLT/Giraffe stellar spectra in the wavelength range 6440–6810 Å in the γ Velorum cluster, and calibration of spectral indices[⋆,⋆⋆]

F. Damiani[1], L. Prisinzano[1], G. Micela[1], S. Randich[2], G. Gilmore[3], J. E. Drew[4], R. D. Jeffries[5], Y. Frémat[6],
E. J. Alfaro[7], T. Bensby[8], A. Bragaglia[9], E. Flaccomio[1], A. C. Lanzafame[10], E. Pancino[9,11], A. Recio-Blanco[12],
G. G. Sacco[2], R. Smiljanic[13,14], R. J. Jackson[5], P. de Laverny[12], L. Morbidelli[2], C. C. Worley[3], A. Hourihane[3],
M. T. Costado[7], P. Jofré[3], K. Lind[3], and E. Maiorca[2]

(Affiliations can be found after the references)

ABSTRACT

We present a study of spectral diagnostics available from optical spectra with $R = 17\,000$ obtained with the VLT/Giraffe HR15n setup, using observations from the *Gaia*-ESO Survey, on the γ Vel young cluster, with the purpose of classifying these stars and finding their fundamental parameters. We define several spectroscopic indices, sampling the amplitude of TiO bands, the Hα line core and wings, and temperature- and gravity-sensitive sets of lines, each useful as a $T_{\rm eff}$ or $\log g$ indicator over a limited range of stellar spectral types. Hα line indices are also useful as chromospheric activity or accretion indicators. Furthermore, we use all indices to define additional global $T_{\rm eff}$- and $\log g$-sensitive indices τ and γ, valid for the entire range of types in the observed sample. We find a clear difference between gravity indices of main-sequence and pre-main-sequence stars, as well as a much larger difference between these and giant stars. The potentially great usefulness of the (γ, τ) diagram as a distance-independent age measurement tool for young clusters is discussed. We discuss the effect on the defined indices of classical T Tauri star veiling, which is however detected in only a few stars in the present sample. Then, we present tests and calibrations of these indices, on the basis of both photometry and literature reference spectra, from the UVES Paranal Observatory Project and the ELODIE 3.1 Library. The known properties of these stars, spanning a wide range of stellar parameters, enable us to obtain a good understanding of the performances of our new spectral indices. For non-peculiar stars with known temperature, gravity, and metallicity, we are able to calibrate quantitatively our indices, and derive stellar parameters for a wide range of stellar types. To this aim, a new composite index is defined, providing a good metallicity indicator. The ability of our indices to select peculiar, or otherwise rare classes of stars is also established. For pre-main-sequence stars outside the parameter range of the ELODIE dataset, index calibration relies on model isochrones. We check our calibrations against current *Gaia*-ESO UVES results, plus a number of Survey benchmark stars, and also against *Gaia*-ESO observations of young clusters, which contribute to establishing the good performance of our method across a wide range of stellar parameters. Our gravity determination for late-type PMS stars is found to be accurate enough to let us obtain gravity-based age estimates for PMS clusters. Finally, our gravity determinations support the existence of an older pre-main-sequence population in the γ Vel sky region, in agreement with evidence obtained from the lithium depletion pattern of the same stars.

Key words. stars: fundamental parameters – stars: pre-main sequence – open clusters and associations: individual: gamma2 Velorum

1. Introduction

The γ Vel cluster was discovered in X-rays by Pozzo et al. (2000), in a ROSAT observation of the Wolf-Rayet binary γ² Vel itself. Its age and distance have been recently estimated as about 5–10 Myr and 356 ± 11 pc by Jeffries et al. (2009), in a study based on deep optical photometry and *XMM-Newton* X-ray observations. Star formation appears to have ceased long ago, as there is no sign of ongoing formation events (Hernandez et al. 2008); the cluster pre-main-sequence (PMS) stars also show only rare evidence of disks (Hernandez et al. 2008), and most of them are therefore weak-line T Tauri stars (WTTS), with no accretion of circumstellar material on the stellar surface.

The γ Vel cluster was observed in the framework of the *Gaia*-ESO Survey (Gilmore et al. 2012), consisting of VLT/FLAMES observations of 80–100 open clusters (of all ages, except embedded ones), and selected Milky Way field star samples, with 300 nights allocated over 5 years. Survey observations started on 31 December 2011, and γ Vel was one of the earliest observed clusters. The FLAMES fiber positioner was used to feed both UVES and Giraffe spectrographs, for the brighter and fainter cluster stars respectively. We focus here on the Giraffe observations, all made using the HR15n setup, with $R \sim 17\,000$, in the band $\lambda\lambda 6440$–6815 Å. This setup has the advantage of observing both the Hα line and the Li I resonance line at 6707.7 Å, of great interest when studying young stars, and PMS stars in particular. On the other hand, this has not been the band of choice for deriving stellar fundamental parameters such as effective temperature $T_{\rm eff}$, gravity $\log g$, or metal abundance z. This wavelength range is barely mentioned in stellar classification textbooks such as Jaschek & Jaschek (1990), or Gray & Corbally (2009). Curve-of-growth methods, often based on the study of a multitude of Fe I/Fe II lines, are also not applicable here,

essentially because of the paucity and weakness of Fe II lines in this range. Therefore, it is important to investigate whether stellar spectra obtained with this instrumental setup do contain indicators useful to derive these fundamental parameters, and with what degree of uncertainty. Since all stars later than F spectral type in both young and old clusters in the *Gaia*-ESO Survey will be observed using the HR15n Giraffe setup, the solution to this problem has a general interest for the entire Survey. As we discuss below, the *Gaia*-ESO Survey observations of the γ Vel cluster offer several advantages for this type of investigations.

We initially consider likely members of the γ Vel cluster, which have a homogeneous near-solar metallicity, as recently determined by Spina et al. (2014) using *Gaia*-ESO UVES data. This also agrees with existing studies of metallicity in other nearby star-formation regions (Padgett 1996; Santos et al. 2008; D'Orazi et al. 2009a; Biazzo et al. 2011). Many stars in the stellar sample considered here are however not cluster members, and are therefore of unknown metallicity. On the basis of the γ Vel dataset spectra we are able to define temperature- and gravity-sensitive indices, as well as indices probing PMS accretion and veiling.

Then, we consider the issue of calibrating quantitatively the temperature, gravity, and metallicity dependence of the newly defined indices on the basis of additional data. The indices are optimized to take advantage of the HR15n setup resolution ($R \sim 17\,000$), and there are not many public sets of stellar spectra with high enough spectral resolution, in the same wavelength range, useful to our purposes. We have nevertheless been able to calibrate indices on the basis of two sets of public spectral libraries; these results were then checked for consistency against (1) current *Gaia*-ESO Survey results obtained from UVES spectra of several hundreds stars, and a few tens common UVES-Giraffe targets; (2) about two dozen *Gaia*-ESO Survey benchmark stars with accurately known properties; and (3) *Gaia*-ESO Survey HR15n datasets of young clusters.

This paper is structured as follows: in Sect. 2 the observed sample is described, while in Sect. 3 we describe the preliminary data preparation; then in Sect. 4 we study several spectroscopic diagnostics available from these observations, ranging from molecular bands, to Hα, to lesser-known lines in the HR15n range, and we define sets of new spectral indices, especially suited as $T_{\rm eff}$ and $\log g$ diagnostics. Section 5 presents an initial photometric calibration of our new $T_{\rm eff}$ indicator. In Sect. 6 we discuss the choice of the reference spectra for general calibration, their merits and disadvantages. In Sect. 7 we describe the calibration of indices made from each of these spectral sets, and the relevant consistency checks. In Sect. 8 we discuss all results obtained, how they can be applied to other observations, and also what can be possible future developments of this work. A summary is provided in Sect. 9.

2. Observed sample composition in the γ Vel dataset

The VLT/FLAMES/Giraffe fiber-fed spectrograph allows multi-object spectroscopy of up to ~130 objects at a time. Simultaneous to the observations described here, FLAMES/UVES observations were also performed, but are not discussed in this work. The target sample was chosen to be inclusive of all possible candidate cluster members (Bragaglia et al., in prep.), on the basis of the $(V, V - I_{\rm c})$ color–magnitude diagram (CMD), using the photometric catalog from Jeffries et al. (2009). The CMD of Fig. 1 shows all γ Vel
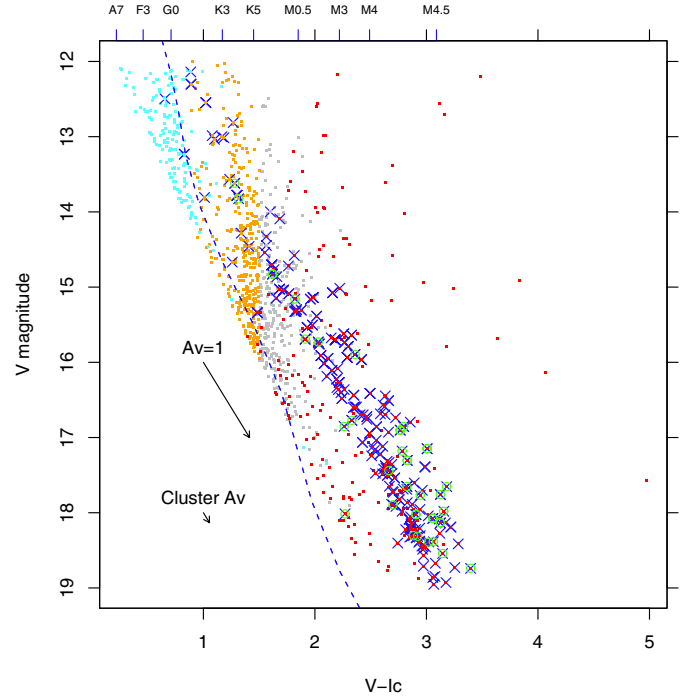
Fig. 1. The $(V, V - I_{\rm c})$ color–magnitude diagram of stars in the γ Vel cluster region observed with Giraffe and with $S/N > 15$. Here and in all following figures color-coded symbols are consistently used: blue crosses are candidate cluster members, cyan dots are A to early-G stars, red dots are late-K and M stars, and orange and gray dots are the remaining stars; see Sect. 4.1 for details. Stars with wide Hα emission are indicated with green circles. The unreddened ZAMS from Siess et al. (2000) at the cluster distance is shown as a blue dashed line. The large arrow indicate a reddening vector for $A_V = 1$, while the small arrow indicates the low estimated reddening for the cluster. In the top axis, spectral types corresponding to unreddened main-sequence stars are indicated.

stars observed with Giraffe in the Survey with signal-to-noise ratio $(S/N) > 15$ on individual spectra, down to the Survey limiting magnitude $V = 19$. Throughout this paper we use consistent color/symbol codes for scatter plots: red dots are stars exhibiting molecular bands, cyan dots early-type stars with wide Hα absorption, orange and gray dots the remaining (mostly GK) stars; see Sects. 4.1 and 4.2 for details. Blue crosses indicate bona-fide cluster members, selected by the presence of at least two indicators among: X-ray emission (from Jeffries et al. 2009), lithium $EW > 150$ mÅ, radial velocity (RV) in the range 10–22 km s^{-1} (the latter two membership indicators for γ Vel stars are studied by Jeffries et al. 2014; and Prisinzano et al., in prep.). To these membership criteria we have added the presence of wide Hα emission (green circles, see Sect. 4.2), considered sufficient by itself (as distinctive of Classical T Tauri Stars – CTTS). Each of the other membership indicators above, taken alone, did instead not seem to guarantee a clean enough candidate member list. This member selection cannot be considered either complete (e.g., the X-ray data do not cover the whole cluster), nor entirely free of contaminants (like slightly older lithium-rich G stars), but is found to be accurate enough for the purposes of this work. A much more detailed membership study of the cluster will be presented by Prisinzano et al. (in prep.).

The putative members (labeled "M" in Table 3) define the cluster locus, which for types later than about G0 lies distinctly above the ZAMS (blue dashed line) at the cluster distance

(356 pc, Jeffries et al. 2009), indicating their PMS nature corresponding to the cluster young age. ZAMS colors are taken from Siess et al. (2000), with color calibration from Kenyon & Hartmann (1995). The absence of stars below a cutoff line in the CMD is caused by the sample selection for the Survey observation (discussed by Bragaglia et al., in prep.), while the complete photometric database (from Jeffries et al. 2009, their Fig. 1) shows many stars below that line. In γ Vel, the parental molecular cloud appears to have dissipated, with no excess dust and gas remaining in the cluster region. This is also entirely consistent with the low value of extinction found toward cluster stars by Jeffries et al. (2009), namely $E(B - V) = 0.038 \pm 0.016$ mag, or $A_V = 0.13 \pm 0.055$ mag (and $E(V - I) = 0.055 \pm 0.023$), also shown in Fig. 1. The reddening of foreground stars is expected to be even lower than this value.

The fact that $E(V - I)$ is so small for cluster members, and even smaller for main-sequence (MS) foreground stars, together with the fact that nearly all cluster members have normal photospheric spectra (without veiling or strong emission lines), make the $V - I_c$ color index a good proxy for $T_{\rm eff}$, once the MS/PMS status of a star is ascertained. The relatively small distance has enabled cluster stars as late as mid-M to be observed with Giraffe. The predominance of WTTS over CTTS is also of advantage, since it permits a study of stellar properties, uncomplicated by accretion phenomena. At the same time, the study of the few CTTS present enables to check whether methods used to study WTTS may be extended to accreting stars as well.

Above the observational cutoff line, Survey targets were selected randomly, and therefore include a substantial number of field stars. The spectral-type range expected for un-reddened stars (thus including MS/PMS stars) is late-A to mid-M. Figure 1 shows that the selection limit for the Survey corresponds roughly to the unreddened ZAMS at the cluster distance: therefore, low-reddening ZAMS stars can belong to the observed sample only up to a distance of 710 pc for late-A stars, and of 280 pc for mid-M stars. Thus, this main-sequence subsample of all observed stars is not expected to have reddening higher than the cluster itself (or only a little more for stars earlier than G0), i.e. the bulk of observed MS or PMS stars has negligible or little reddening, $A_V < 0.2$ mag. Early-type stars, which are rare objects and are thus a priori expected to make only a small fraction of the observed sample, can enter it even if they are MS stars found at high distances and reddening. Apart from MS/PMS stars, the observed sample certainly comprises many giant stars (suggested from the excess of data points in the CMD of Fig. 1 between $1.3 < V - I_c < 2$), observable up to large distances. Moreover, most giant stars are expected to belong to the red clump, in which they spend a relatively long part of their evolved-star lifetime, several magnitudes above the main sequence: this implies that most giants in the observed sample are likely to be much more distant than MS/PMS sample stars. For this reason most giant stars in the observed sample are expected to be substantially reddened. Therefore, MS/PMS stars and giants are expected to make two mostly distinct, reddening-segregated subsamples.

Overall, the γ Vel Giraffe observed sample comprises 1802 spectra of 1242 distinct stars; 439 stars (35% of the sample) were observed more than once. Duplicated spectra of the same star are here analyzed individually. Such a large sample of spectra permits a study of spectral diagnostics with very good statistics, for the different populations contained in the sample. Tasks within the *Gaia*-ESO Survey consortium are distributed among several distinct Working Groups (WG). In particular, the initial reduction of Giraffe spectra is made by the
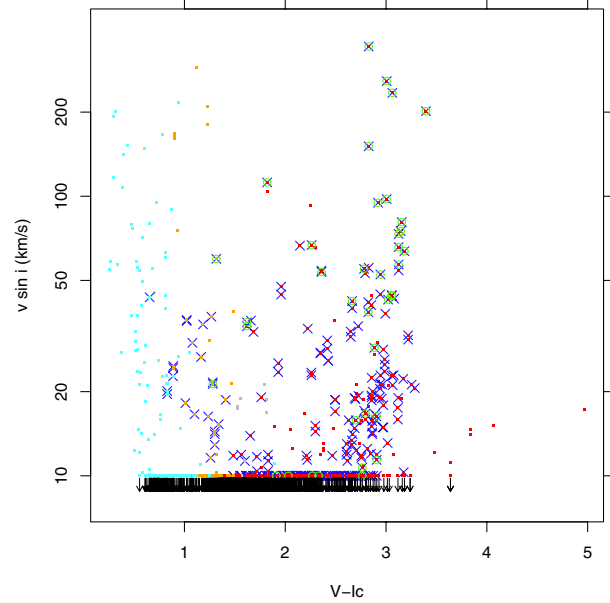
Fig. 2. Rotational velocity $v \sin i$ vs. $V - I_c$. A significant number of cluster candidate members are fast-rotating stars, especially at the latest spectral types. Symbols are as in Fig. 1. Sources with released $v \sin i$ values lower than 10 km s^{-1} are marked as upper limits (arrow symbols).

Cambridge Astronomical Survey Unit (CASU) within WG7, and provides wavelength-calibrated, sky-subtracted, barycentrically-corrected spectra (Lewis et al., in prep.). Radial-velocity (RV) measurements, $v \sin i$ and other directly-measured parameters are also provided for Giraffe data by CASU (Koposov et al., in prep.), as part of WG8 activities. These spectra and RVs, from data release GESiDR1Final, form the basis for the work discussed in this paper. The spectral range is 6444–6816 Å, and the pixel size is 0.05 Å. Results presented here contribute to the activities of WG12, whose task is spectrum analysis for young and PMS clusters, WG10, dealing with analysis of FGK star spectra of field and older cluster stars, and WG14, dealing with peculiar stars.

3. Data preparation

In this work we define several spectral indices, computed as in several previous studies over fixed wavelength ranges comprising crucial line features. In the following, we repeatedly remark the effect of fast rotation on the spectral indices we define, which is particularly relevant for some of the γ Vel probable members (young and fast-rotating stars, mostly of late type). Therefore, we show for general reference a $(V - I_c, v \sin i)$ diagram in Fig. 2, made using the GESiDR1Final released $v \sin i$ values[1].

The continuum shape has impact on the spectral indices which will be defined in the next section, both because asymmetric[2] (molecular band-strength) indices are sensitive to continuum gradients, and also because indices which are symmetric, but computed over a relatively large wavelength region (e.g., the Hα wings), are sensitive to second derivatives in the continuum. We have therefore normalized the spectra ourselves,

---

[1] In several cases, the released $v \sin i$ values are exceedingly low, e.g., 1 km s^{-1} or less, considering the instrumental resolution: these are here considered as upper limits at 10 km s^{-1}, consistently with the work by Jeffries et al. (2014), on the same data.

[2] Namely, with a blue-red asymmetry in the used wavelength regions.
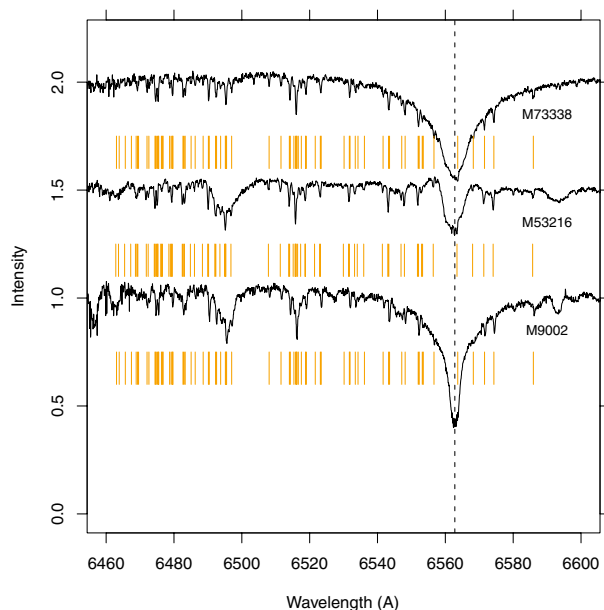
Fig. 3. Three examples of fast-rotating early-type star spectra with evident telluric-line contamination (orange segments). The dashed line indicates the Hα line wavelength. Spectra are labeled with the sequential star number from Jeffries et al. (2009).

using a fifth-degree polynomial. The choice of such a low polynomial order is important, since it ensures that wide features in the spectrum, such as broad molecular bands and Hα wings are not "fitted" by the continuum normalization procedure, but their shape is preserved. In order to avoid problems arising from both strong Hα emission or wide absorption, we did not use in the fitting procedure a 40 Å wide region centered on Hα. Thus, this normalization step is rather different from, e.g., pseudo-continuum recovery in M stars, which is meant to trace the detailed shape of molecular bands, over which individual spectral lines are found superimposed. We remark that the adopted normalization recipe deliberately sets to unity the local average spectrum intensity, but not necessarily the true continuum level: this is irrelevant for our indices definition. We emphasize that the adopted normalization procedure is an integral part of the procedure described in the following sections: with a different normalization recipe results are not guaranteed to remain unchanged.

The released spectra are not corrected for telluric lines. Therefore, in the cases where telluric contamination was strong, we did the correction ourselves. Identification of lines as telluric was made by considering the spectra of (possibly fast-rotating) early-type stars, and looking at narrow lines which were fixed in (observed) wavelength, regardless of the star RV (most early-type stars do not belong to the cluster, and their RV are broadly distributed). An average, template telluric-line spectrum was thus computed, which yielded good results when subtracted from all massive stars, with the only difference of a scaling factor. For a given Observing Block (OB), all stars are observed simultaneously and the scaling factor for the telluric absorption spectrum is the same for all of them: therefore, the template telluric-line spectrum, with the OB-dependent scaling factor, was divided off from all stars in the same OB. Only a few OBs were lacking early-type stars to use this method; in these cases, the stars with the highest S/N and the fastest rotation were used to determine the scaling factor of the template telluric spectrum. The contaminating telluric lines were found only in the short-wavelength side of the HR15n range,

between 6460–6587 Å, including Hα and other very useful features which will be introduced below. The red part of the HR15n range (including the lithium line) is unaffected. Examples of the strongest telluric-contaminated spectra are shown in Fig. 3.

Finally, released RV values for about 80 stars did not appear to be correct and we derived them independently from the cross-correlation function (CCF) with ten different templates, chosen from among slowly-rotating, high-S/N stars in the γ Vel dataset, without emission lines, and spanning the entire range of (visually defined) spectral types. Our redetermined RV values have a likely larger error (∼1–2 km s^{-1}) compared to that typical of GESiDR1Final released RVs (Jeffries et al. 2014), but this is not critical for the present work. In most cases, the incorrect RV values were due to SB2 nature, and are being revised in forthcoming data releases. After inspection of all spectra (and their CCFs), we discard all the SB2 systems (labeled in Table 3) from our analysis[3].

4. Definition of spectral indices

The range of spectral types expected for observed stars is so wide that, in order to classify them with some level of detail, a hierarchical classification is necessary, to distinguish in the first place between early-type, intermediate, and late-type stars. Then we proceed to consider if more refined indicators of, e.g., luminosity class, stellar activity, accretion, are available from the observed spectra. In this section we introduce such a classification scheme, first using molecular bands and the Hα line, and subsequently turning our attention to other groups of interesting spectral lines.

It may be useful to consider the expected locations of stars of different ages/masses in the $(T_{\rm eff}, \log g)$ plane. Figure 4 shows model isochrones in such a plane, for both PMS stars in the age range 0.1–50 Myr and ZAMS stars (solid lines, from Siess et al. 2000), and evolved stars in the age range 10 Myr–10 Gyr and $Z = 0.019$ (dashed lines, from Padova group, Marigo et al. 2008 with corrections from Case A in Girardi et al. 2010[4]). The bulk of field giants are expected to be comprised between the 1–10 Gyr isochrones. The 5–10 Myr isochrones, where we expect to find γ Vel cluster members, cross the giant-star region for $T_{\rm eff} > 5500$ K, but become increasingly separated from giants at lower $T_{\rm eff}$ values. At the same time, $\log g$ in such cold cluster members is at least 0.5 dex lower than ZAMS stars of same $T_{\rm eff}$. Therefore, the latest-type stars are the most promising place where to expect differences in gravity-sensitive features between giants and PMS stars in particular, and to a lesser extent between PMS and ZAMS stars. At $T_{\rm eff}$ above 5500–6000 K, the $\log g$ of PMS stars is similar to that of giants, making their discrimination impossible, while remaining slightly above ZAMS $\log g$ values.
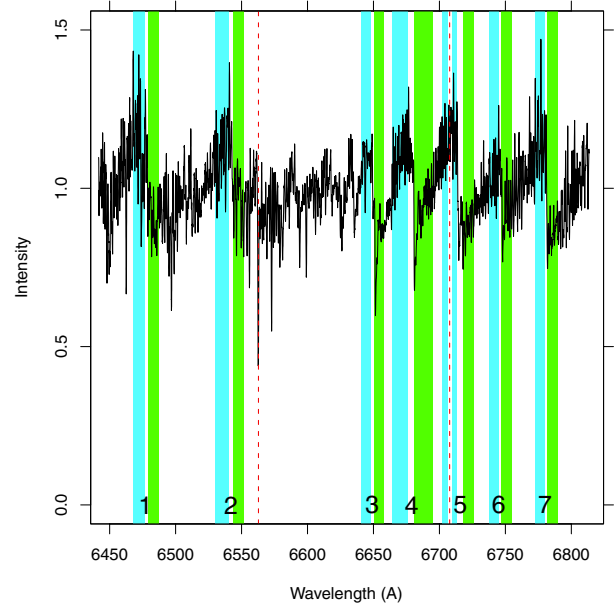
4.1. Molecular bands

Molecular bands, especially from TiO, are an unmistakable characteristic of M stars. The strongest TiO molecular bands fall at

---

[3] Values of spectral indices for SB2 systems are however included in Table 3 since they may be of some use, with due care, to infer some rough average properties of the components; this is also true of spectra with low S/N: also in this case, the choice of the most appropriate threshold for rejection of noisy results is left to the prospective user, being dependent on their specific needs.

[4] Isochrones available through http://stev.oapd.inaf.it/cgi-bin/cmd
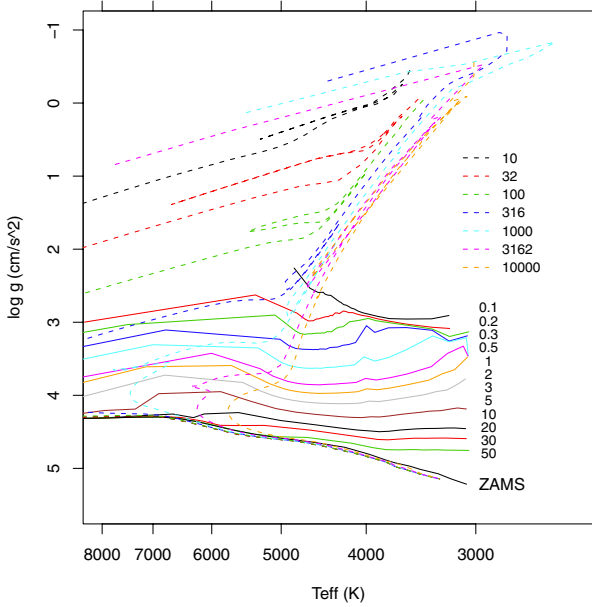
Fig. 4. Model isochrones in the $(T_{\rm eff}, \log g)$ plane, for both PMS stars in the age range 0.1–50 Myr and ZAMS stars (solid lines, from Siess et al. 2000), and evolved stars in the age range 10 Myr–10 Gyr (dashed lines, from Marigo et al. 2008). Isochrone ages are labeled in Myr units.

Fig. 5. HR15n spectrum of a mid-M star in the γ Vel dataset, showing several prominent molecular bands. Vertical red dashed lines indicate Hα and the Li I line at 6707.76 Å. Cyan and green regions indicate respectively "peaks" and "valleys" of bands selected empirically for study here, identified by numbers 1–7 (above bottom axis).

redder wavelengths than the Giraffe HR15n range (e.g., $\lambda >$ 7000 Å), but a few bands are clearly seen in the HR15n range as well. Several spectral indices based on molecular bands were extensively studied by e.g., Kirkpatrick et al. (1991), Reid et al. (1995), Briceño et al. (1998), Jeffries et al. (2003, for NGC 2547), Lyo et al. (2004, 2008, for η Cha and ϵ Cha), Riddick et al. (2007, and references therein), Lawson et al. (2009), Shkolnik et al. (2009). In nearly all these studies, with the exception of the "TiO 1" index defined by Reid et al. (1995), the spectral region used to define interesting indices is outside the HR15n range. Again in Reid et al. (1995), the "CaH 2" index is defined using a spectral window (6814–6846 Å) just beyond the red limit of the HR15n band; some CaH lines (reported to be a gravity indicator) fall inside the HR15n band as well, longward of 6750 Å (Kirkpatrick et al. 1991). By studying the HR15n band, we are therefore going to explore poorly studied molecular indicators, which are the subject of this section.

Figure 5 shows the Giraffe HR15n normalized spectrum of a mid-M star (star 2358 in Jeffries et al. 2009, with $V - I_{\rm c} =$ 3.239), with several prominent molecular bands: those studied here are labeled with numbers from 1 to 7 near the bottom axis. Wavelengths shown are in the stellar rest frame. Vertical red dashed lines indicate Hα and the Li I line at 6707.76 Å. The molecular bands cause the spectrum to show "valleys" and "peaks": we have indicated with a cyan background selected "peak" regions, and with green background its corresponding "valley" regions to the right. For each of the bands $n = 1-7$ we define an adimensional band-strength index μ_n, as

$$\mu_n = \left\langle f^{An} \right\rangle / \left\langle f^{Bn} \right\rangle, \qquad (1)$$

where f is the (normalized) spectrum intensity, the symbol $\langle f \rangle$ indicates flux average, and superscripts An and Bn refer to "peak" and "valley" wavelength ranges, respectively, for index μ_n. The wavelength ranges used are listed in Table 1. Values of μ_n for our sample stars are listed in Table 3.

In order to obtain the best results from this method, we made a careful choice of the band boundaries. First, we have purposely left a minimum separation of 2 Å between the right end of an interval and the left end of the next, to minimize the effect on μ_n of the smearing of bands caused by fast stellar rotation. In this case, "peak" and "valley" regions increasingly contaminate each other (the effect of other, narrow absorption lines being much smaller), with the contaminated wavelength interval being proportional to $v \sin i$. At these wavelengths 2 Å correspond to about 90 km s^{-1}, and very few of our spectra show $v \sin i$ exceeding this value (Fig. 2). Indices μ_n are therefore expected to be affected by rotation only for few stars with $v \sin i > 90$ km s^{-1}. Next, the μ_2 defining range is such that it avoids contamination by the neighboring [N II] line, often strongly in emission in CTTS. In the same way, the μ_4 range is designed to avoid the He I λ6678 emission line, and the μ_5 range avoids the [S II] λ6716 emission line. Finally, since the lithium λ6707.7 line is neither a $T_{\rm eff}$ nor $\log g$ indicator, we excluded a 3 Å interval centered on the Li line from the "peak" region of the μ_5 range (as indicated in Fig. 5). This choice makes μ_5 totally insensitive to Li EW variations in stars with $v \sin i$ up to ~70 km s^{-1}, and only a little above it.

The relatively wide wavelength ranges used to define indices μ_n make these indices to have a generally high S/N: in the worst case of spectra with $S/N = 15$ (per pixel) the statistical 1σ errors on μ_n fall in the range 0.0086–0.012; most stars have however much higher S/N, and errors on μ_n are thus significantly lower than these worst-case limits.

Figures 6 and 7 show the dependence of the seven indices μ_n on $V - I_{\rm c}$: the general increase in the indices toward redder, cooler stars is similar but not identical among the different cases. Only stars with S/N (per pixel) >15 are shown. Index μ_2 is affected by the extreme Hα wings in the earliest-type stars in our sample (cyan dots); index μ_6 appears to saturate for the reddest (non-member) stars in the sample, but not for members (blue crosses), which may indicate a dependence on $\log g$ in addition

Table 1. Wavelength ranges for definition of spectral indices.

Index	A range(s) Å	B range(s) Å
μ_1	6468–6477	6479–6487
μ_2	6530–6540	6544–6552
μ_3	6641–6648	6651–6658
μ_4	6664–6676	6681–6695
μ_5	(6702–6706.26)+(6709.26–6713)	6718–6726
μ_6	6738–6745	6747–6755
μ_7	6773–6780	6782–6790
$\alpha_w{}^a$	(6556.8–6560.8)+(6564.8–6568.8)	(6532.8–6542.8)+(6582.8–6592.8)
α_c	6560.8–6564.8	(6532.8–6542.8)+(6582.8–6592.8)
β_t	6492.6–6502.6	(6487–6489)+(6505–6507)
β_c	(6495.9–6499.3)+(6489–6492)^b	(6487–6489)+(6505–6507)
γ_1	(6759–6761)+(6763.5–6765.5)+ (6768.4–6770.0)+(6771.7–6774.1)	(6761.5–6763.5)+(6765.5–6768.4)+ (6770.0–6771.7)+(6774.1–6776.0)
ζ_1	6624–6626	6632.7–6634.7

Notes. $^{(a)}$ The α_w index must include a correction based on μ, see text. $^{(b)}$ The 6489–6492 Å range is summed with the main range with relative weights 1:7.

to T_{eff}, especially if compared with the lack of such saturation in the μ_3 index for the same red stars, which seem to rule out a reddening effect on the $V - I_c$ color as explanation. The larger scatter observed among member stars near $V - I_c \sim 3$ may be due only partially to the lower S/N of their spectra, near the bottom of the cluster sequence, but especially to their large $v \sin i$ (>90 km s^{-1}), more frequent in this color range than elsewhere (Fig. 2).

Indices μ_1, μ_3, μ_5, and μ_7 show the least scatter around their mean dependence on $V - I_c$, considering only member stars. Therefore, we define an average μ index as

$$\mu = 0.25(\mu_1 + \mu_3 + \mu_5 + \mu_7), \qquad (2)$$

tabulated in Table 3, and whose dependence on $V - I_c$ is shown in Fig. 7 (right). Maximum statistical 1σ error on μ is 0.0057, occurring mostly for our reddest cluster members. The strong correlation with $V - I_c$ for the redder cluster stars is very evident, and interpreted as a T_{eff} dependence. Since μ is essentially dependent on T_{eff}, with a very small (if any) dependence on $\log g$, we consider this index as our primary T_{eff} indicator for late-type stars (basically, M stars). This agrees with the generally accepted adoption of TiO bands as T_{eff} diagnostic for M stars. Stars without TiO bands are located in a narrow strip around $\mu = 1$, which is the reference or "neutral" value for such index. The observed scatter around this value enables us to define a threshold value $\mu_0 = 1.008$ above which the presence of molecular bands, however weak, can be considered certain (dashed line in the figure). We make therefore our initial classification (corresponding to color coding used throughout the paper) as follows:

– Stars with $\mu > \mu_0$ are defined here as late-type, and drawn in all figures with red dots.
– Stars with wide Hα absorption (see Sect. 4.2) are defined as early-type stars[5] (cyan dots).
– Stars showing no wide Hα absorption, nor TiO bands are defined as intermediate-type stars; if they have $V - I_c \leq 1.4$,

their position in Fig. 7 is compatible with no reddening[6], and they are plotted as orange dots.
– Stars without wide Hα or TiO bands, but having $V - I_c > 1.4$, are still intermediate-type stars, but their optical color is too red to be compatible with zero extinction (gray dots), since in this latter case TiO bands would be found in their spectra.

The "gray" stars might be not qualitatively different from the "orange" ones, but their high reddening implies that they are giants, as we argued in Sect. 2. This fact will be very useful when selecting gravity-dependent spectral features in the following. In Fig. 7 (right) a few of the (non-member) red datapoints fall at redder $V - I_c$ than the cluster-member locus: they also are high-reddening stars, which by virtue of their showing molecular bands are to be classed as M giants.

A better understanding may be gained from the study of the mutual relationships between pairs of indices μ_n, as shown in Fig. 8. Especially considering the cluster members, these indices are well correlated with one another, and this further supports using a single μ index as representative. The "saturation" affecting index μ_6 is again visible here, only for very red non-member stars. The lower right panel of Fig. 8 shows however a very interesting "double" correlation between μ_6 and μ_7, with a lower branch populated by members (and other stars), and an upper branch containing only non-members. Moreover, the upper branch joins smoothly near $\mu_6 \sim 1$ with the distribution of gray dots (i.e. reddened giants), and also by virtue of this continuity it is highly probable that stars in the upper branch are M giants. The separation we observe between the two branches, therefore, is the first example of a gravity-sensitive spectral feature in the HR15n range. This initial selection of giants enables us to define suitable template spectra among those in our dataset, which will in turn enable us to study gravity effects on other spectral features.

The index μ might be affected by variable metal abundance, or by veiling, the latter being more likely to occur in young clusters. In stars where veiling is detected and measured (which is rarely the case for γ Vel stars, see below), a veiling-corrected μ may be derived: in fact, a veiling r (ratio of veiling continuum

_____

[5] Here, early-type must be intended in a relative sense, and not as indicative of OBA stars; the Sun itself turns out to be included in this class.

[6] This is not the same as stating that their reddening is zero, however.
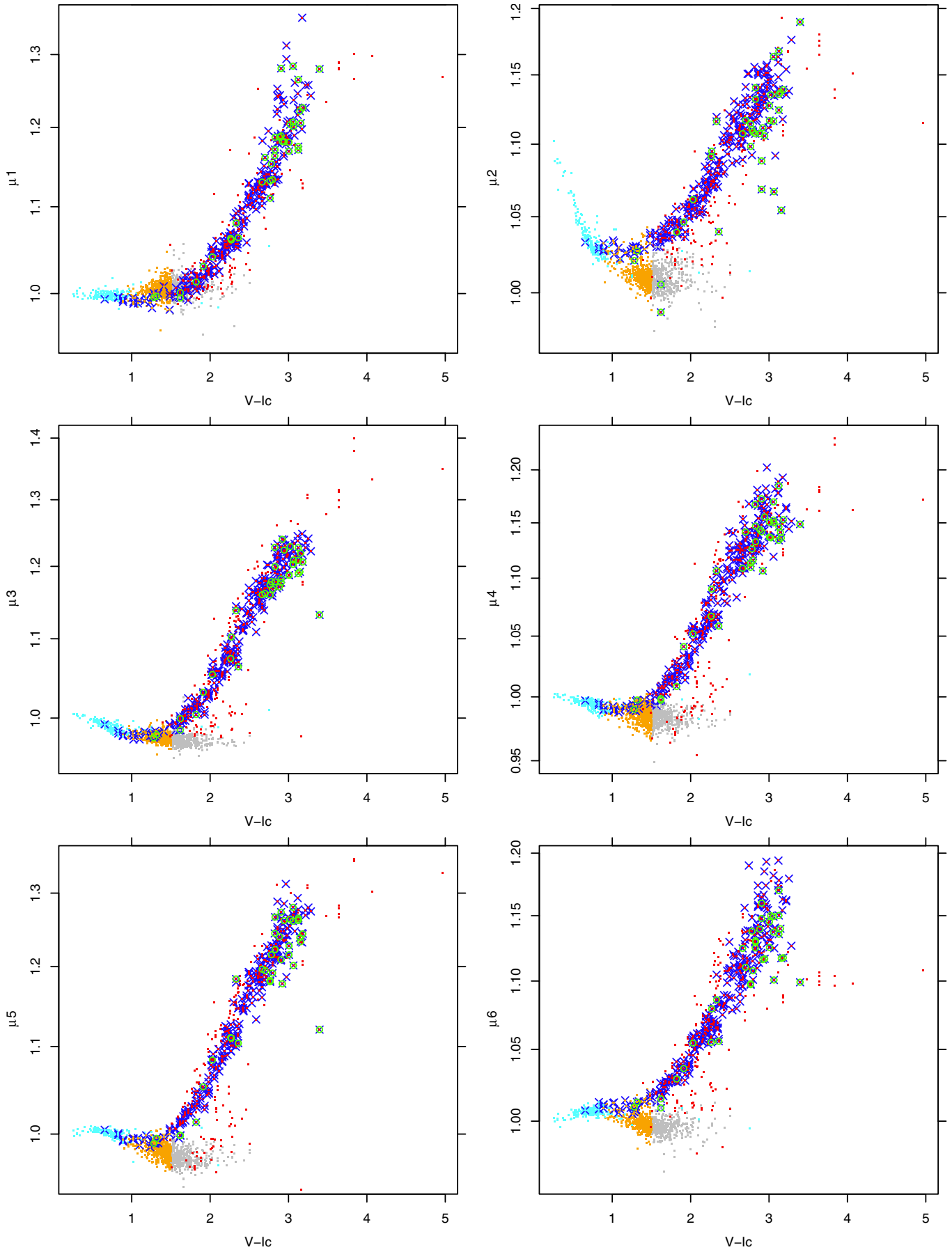
Fig. 6. Molecular indices μ_n vs. $V - I_c$, for $n = 1$–6. Symbols as in Fig. 1.
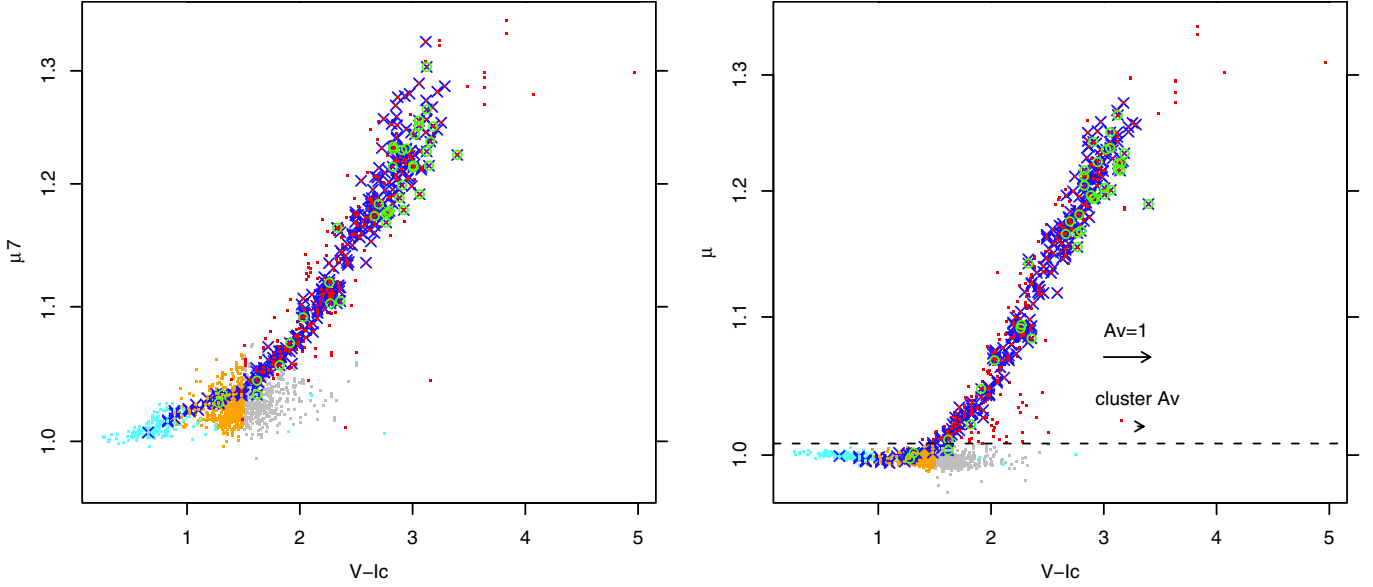
Fig. 7. (**a**), *left*): molecular index μ_7 vs. $V - I_c$. (**b**), *right*): mean molecular index μ vs. $V - I_c$. Symbols as in Fig. 1. In panel **b**), a representative reddening vector is indicated, as well as the very small cluster reddening vector. The horizontal dashed line indicates the limiting value μ_0.

level to star continuum level) causes μ to reduce its distance from its "neutral value" of 1 by a factor $\sim 1 + r$ to a good approximation; this implies that a veiling-corrected index μ^{corr} may be computed from the observed index μ^{obs} as

$$\mu^{corr} = 1 + (\mu^{obs} - 1) \times (1 + r). \qquad (3)$$

In the following, all indices shown are the observed ones, not the veiling-corrected ones, even for the few stars with veiling.

Since the (μ_{n+1}, μ_n) relations shown in Fig. 8 are reddening-independent, they may be used to discriminate true uncertainties on the μ values from residual reddening, which may instead affect the $V - I_c$ color in the $(\mu, V - I_c)$ plot, and contribute to the scatter of datapoints in it (together with photometric color variability). In order to quantify the contribution by reddening and variability to $V - I_c$ scatter, we have made a (rough) polynomial fit to both the $(\mu, V - I_c)$ correlation and the (μ, μ_4) correlation (not shown for brevity); indices μ and μ_4 are statistically independent since μ_4 does not enter in the definition of μ, and their correlation is unaffected by either reddening or variability. Fitting residuals are shown respectively in Figs. 9a and b, as a function of μ: despite the roughness of the fit and systematic trends in the residuals, around $1.05 < \mu < 1.1$ it is clear that the $V - I_c$ vs. μ fit has larger residuals among members (std.dev. = 0.012) than the μ_4 vs.μ fit (std.dev. = 0.0069), a difference which we ascribe to non-uniform reddening and/or to variability among late-type cluster stars. Subtracting (in quadrature) the two standard deviations, and considering the slope of the μ vs. $V - I_c$ relation and the $A_V/E(V - I)$ ratio, we may compute a 1σ range in extinction of $\Delta A_V = 0.12$ mag, thus comparable to the average cluster extinction itself. This percentually large variation in A_V should be considered as an upper bound, however, since Fig. 9 also confirms that some stellar variability is present, as made clear by the multiple observations of the same stars in our dataset (magenta segments). Likely, variable starspots coverage changes slightly the average T_{eff} of the star, causing a small additional spread in the measured values of μ. This may explain at least partially why statistical errors on μ computed above are significantly smaller than the spread of datapoints in the $(\mu, V - I_c)$ diagram. It may also be worth remarking

that, as discussed by Mohanty et al. (2004), magnetic fields in starspots might also affect gravity indicators, because of the additional contribution of magnetic pressure (and thus a decrease in gas pressure and apparent gravity) within a spot, with a reduction in effective gravity by up to 0.25 dex in the cases considered by Mohanty et al. (2004).

4.2. The Hα line

Besides molecular bands, a most prominent feature of many spectra in the sample is the Hα line. It occurs in an extreme variety of line shapes and intensities: from deep absorption to strong emission, from narrow to very wide, passing through barely noticeable lines. The measured quantity most commonly used to describe the line is its equivalent width (EW); however, such a simple scalar quantity does not seem adequate to parametrize the whole observed variety of Hα, to gain the best insight this line may offer on the stellar properties. If we consider, for the moment, only the issue of classification of normal photospheric spectra, the Hα line is known to become strongly saturated and develop wide absorption wings at types earlier than G0 (T_{eff} above ~6000 K), with an intensity peaking around type A0-A2, and then decreasing toward earlier types. For the purpose of this work, concerned only with stars later than mid-A, the latter decrease will not be discussed. For stars between mid-A and early-G, instead, we have tried to define a spectroscopic index measuring the Hα line wings.

Figure 10 shows the spectral region around Hα for some representative spectra in the γ Vel sample, covering most of the encountered situations as far as Hα is concerned, from earlier (bottom) to later (middle) spectral types, and including some narrow- and wide-emission stars (topmost two spectra). To define Hα spectroscopic indices, we have chosen to consider separately the emission arising from different line parts: the line core (2 Å from line center, orange in the figure), and the inner line wings (beween 2–6 Å from line center, cyan in the figure). The line reference continuum is measured between 20–30 Å on both sides from line center (green in the figure), in order to minimize the effect of the wide line wings found in early-type stars.
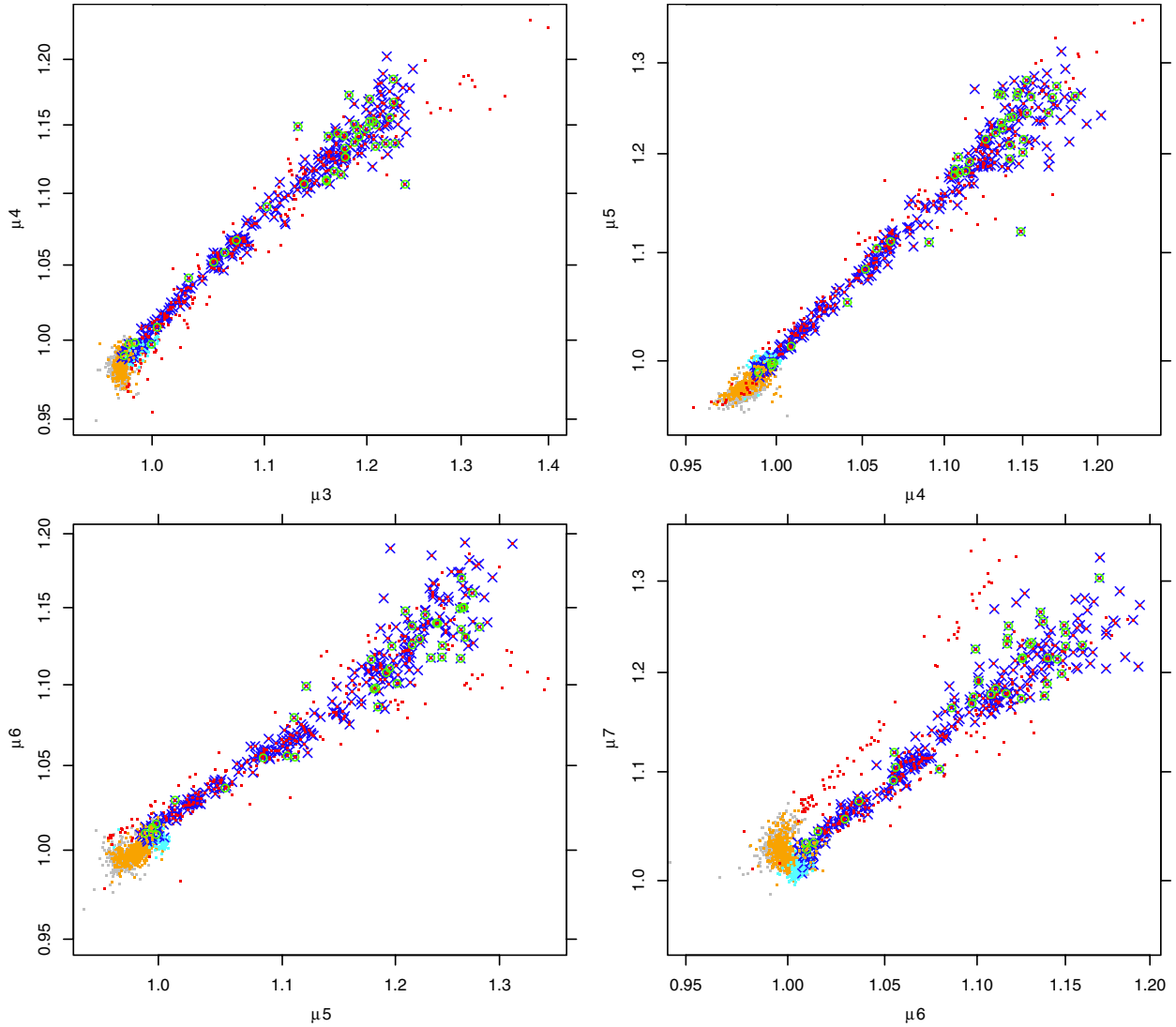
Fig. 8. Plots of indices μ_{n+1} vs. μ_n, for $n = 3-6$. Symbols as in Fig. 1.

Weak Hα lines, broadened only by rotation, are entirely contained in the line core region up to $v \sin i \sim 90$ km s^{-1}. The same is true of narrow, chromospheric-like emission lines (e.g., second spectrum from top in the figure). The wide absorption wings of early-type stars (bottom spectrum in the figure), and the wide emission profiles of CTTS (topmost spectrum in the figure), are well sampled by the inner-wings region selected. The spectral regions covering the whole wings are only suited for use in early type stars, since in late-type stars they are filled by many absorption lines (or bands), and considering them rather that just the inner wings adds both noise and systematic effects to the corresponding Hα indicator. The third spectrum from top in Fig. 10 belongs to a M star, as evident from the molecular band causing the jump near 6540 Å (sampled by our index μ_2). In these stars, the reference continuum for Hα wings index is not flat, and a correction will be needed.

Using these spectral regions, we define two indices, describing the Hα core and (inner) wing components respectively, as

$$\alpha_c = \langle f_{\text{core}} \rangle / \langle f_{\text{continuum}} \rangle, \tag{4}$$

and

$$\alpha_w = \langle f_{\text{wings}} \rangle / \langle f_{\text{continuum}} \rangle - 0.4 \times (1 - \mu). \tag{5}$$

Note the corrective term included in the α_w definition: this compensates the jump in pseudo-continuum emission near 6540 Å, as noted above, which would otherwise lead to a downward-bending α_w toward redder stars. This correction ensures instead a flat dependence on star color for all late-type stars (excluding CTTS) as can be clearly seen in Fig. 11. Strictly speaking, the correction is tied to the spectrum jump sampled by index μ_2, but since this index is also very well correlated to the average molecular index μ, we use this latter to compute the corrective term. Figure 11 also shows that for blue stars α_w is correlated with color, as expected; deviant points (redward of the main correlation) are likely reddened stars. We therefore set a threshold value $\alpha_{w0} = 0.94$, below which we classify stars as early-type (shown in all plots with cyan dots), as already anticipated in Sect. 4.1. The figure also shows that many stars have $\alpha_w > 1.1$, namely far above the spread typical of most stars, including cluster members. These stars, like the topmost spectrum of Fig. 10, have wide Hα emission lines, and are therefore candidate CTTS. We indicate them with green circles throughout all paper figures. Among the cluster members in the range $1.0 < \alpha_w < 1.1$, some upwards spread in α_w values is caused by fast rotation, which broadens an intrinsically narrow chromospheric Hα line so much that the line wings cause a small increase in α_w above unity; this
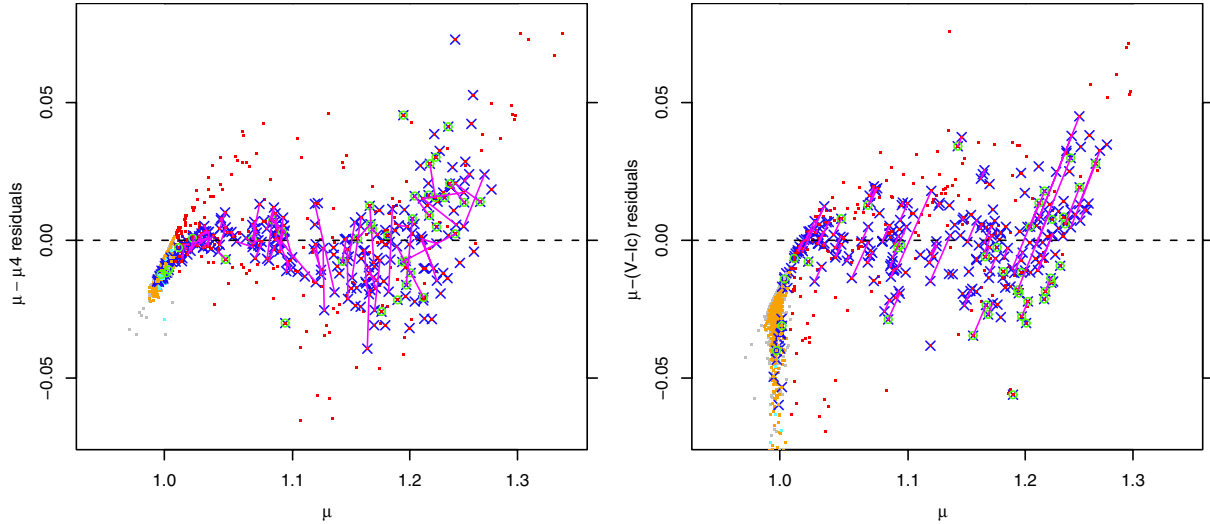
Fig. 9. (a), *left*): best-fit residuals of index μ vs. μ_4. **(b)**, *right*): best-fit residuals of μ vs. $V - I_c$. Symbols as in Fig. 1. Magenta segments connect different observations of the same stars.
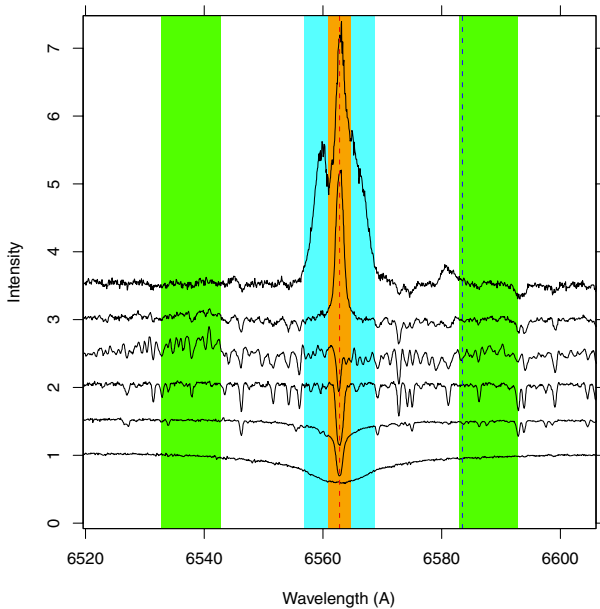
Fig. 10. Sample spectra of γ Vel stars in the Hα region, in a sequence of earlier (bottom) to later (middle) spectral types, and including some narrow- and wide-emission stars (top). Colored regions indicate wavelength ranges used to define the indices discussed in the text. Green: continuum region. Orange: Hα line core. Cyan: (inner) line wings. The two dashed vertical lines indicate the Hα line and the [N II] nebular line.
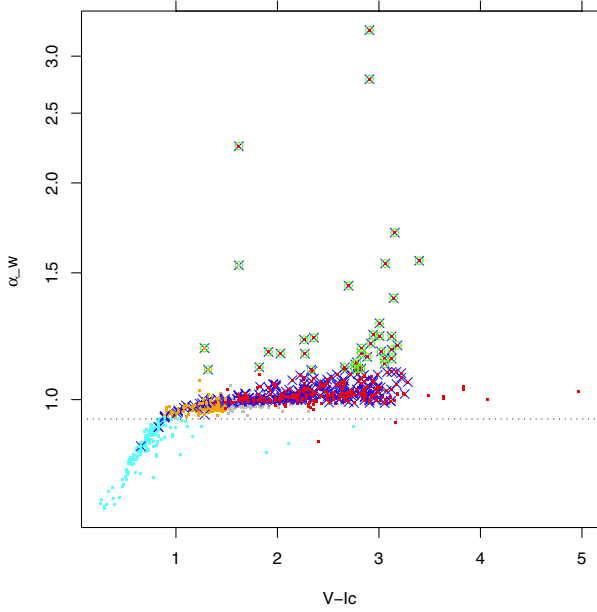
have been signaled. A better understanding of our indices ability to find some types of peculiar stars is gained in Sect. 7.1.

Since we only consider stars with average $S/N > 15$ per pixel, minimum S/N in the indices α_c, α_w are computed to be 96 and 128, respectively, corresponding to (maximum) 1σ expected errors in the indices of approximately 0.027 and 0.008, respectively, excluding CTTS. As for μ, these statistical errors are much smaller than the actual spread of datapoints in all relevant figures. The α_w and α_c values are reported in Table 3. If the Hα line is entirely contained within ± 6 Å from line rest wavelength, it is also possible to compute the line EW from our two indices, using the expression (where positive EW values mean emission)
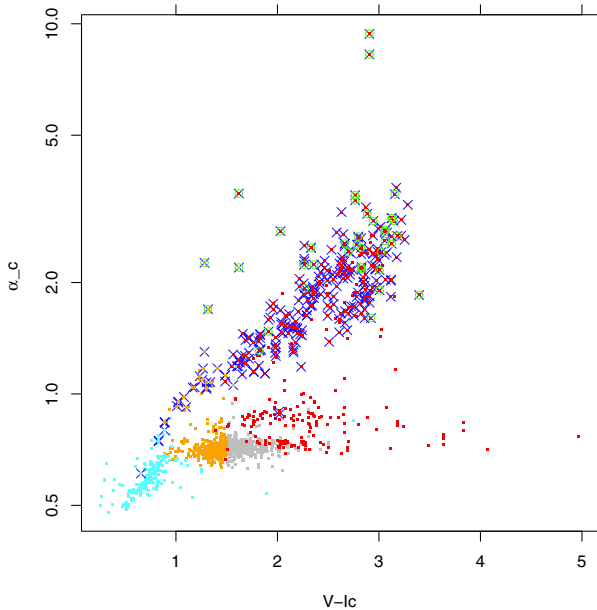
$$EW(H\alpha)(\text{Å}) = 4 \times \alpha_c + 8 \times \alpha_w - 12. \qquad (6)$$

Figure 12 shows instead the α_c index vs. $V - I_c$. This figure shows very characteristic patterns for different classes of stars: the strong Hα absorption of early-type stars makes their α_c index to attain the lowest values in the sample. Most of the cluster members, instead, are found in a characteristic band in this diagram. The very few members stars above the main cluster locus are strong emission-line stars, and the single one below it might be a spurious candidate member. For most cluster stars, this strong Hα core emission is not accompanied by emission in the Hα wings (see Fig. 11): Hα lines in these stars are therefore narrow, as characteristics of chromospheric emission, not of CTTS stars. The cluster locus in Fig. 12 describes thus the dependence of chromospheric emission on spectral type (for which $V - I_c$ is a good proxy in the particular case of γ Vel stars). Since chromospheric emission is known to decay with stellar age t as $\propto t^{-1/2}$ (Skumanich 1972), the group of non-cluster late-type stars (red dots) at lower α_c values ($\alpha_c < 1$) is likely to be identified with much older low-mass MS field stars. Moreover, we identify the small "tail" of red points attached to the cloud of (background) gray stars as M giants. Most non-cluster, intermediate-type stars (MS stars in particular) have only weak, very uniform Hα absorption.

A reddening-free α_c vs. α_w diagram (shown in Fig. 13) is the most useful diagnostics of the nature of Hα emission. Stars in the lower left part are characterized by wide Hα absorption lines; narrow Hα emission accounts for the vertical strip of datapoints around $\alpha_w = 1$; stars with wide Hα emission are candidate CTTS
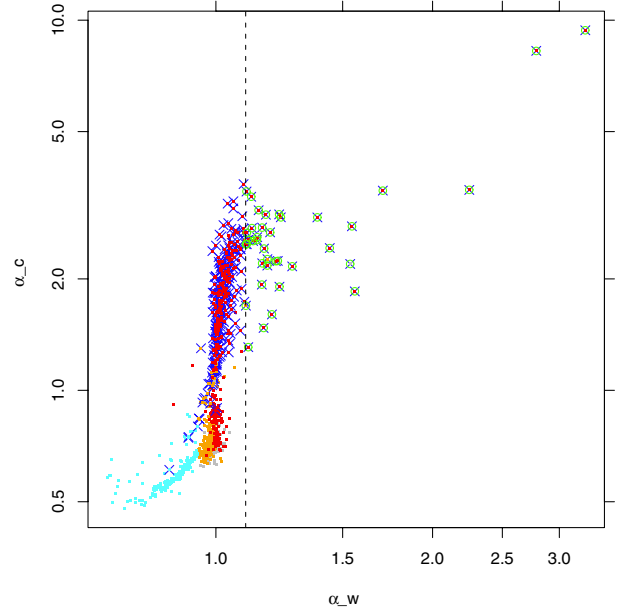
cannot however explain datapoints much above the $\alpha_w = 1.1$ threshold. Note also that because of widespread variability in PMS stars' emission lines, stars may cross the $\alpha_w = 1.1$ threshold from one observation to the next, as found also using different definitions of CTTS status. Finally, we note the presence of two stars exhibiting molecular bands (hence shown with red dots) below the threshold $\alpha_{w0} = 0.94$, well separated from all other late-type stars, and whose location in the diagram cannot be therefore ascribed to reddening. Such outliers are peculiar stars, which need to be examined individually; within the Survey, this is the main task of WG14, to which these objects

Fig. 11. The α_w Hα wing index vs. $V - I_c$ color. Symbols as in Fig. 1. The horizontal dotted line at $\alpha_w = 0.94$ shows the adopted limit for stars with wide Hα absorption. Stars (shown with green circles) with $\alpha_w > 1.1$ have instead wide Hα emission, and are therefore candidate CTTS.

Fig. 13. Index-index diagram α_c vs. α_w. Symbols as in Fig. 1. The vertical dashed line indicates the limiting value $\alpha_w = 1.1$ for selection of stars with wide Hα emission, i.e. likely CTTS.

since the hydrogen abundance is essentially the same for varying metallicity. Therefore, we consider our α_w index a primary T_{eff} indicator for early-type stars in the studied sample.

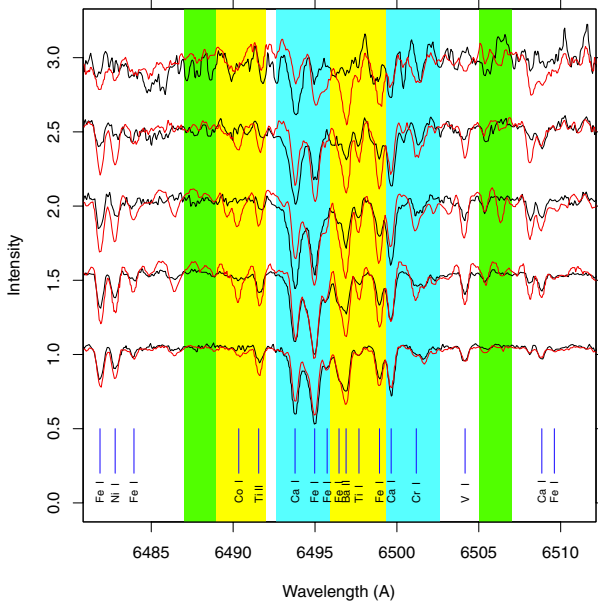### 4.3. The 6490–6500 Å region

After Hα and molecular bands, the most conspicuous feature in the HR15n spectral range is the close group of lines between 6490–6500 Å. The strongest lines in this group, observed in our spectra are those of Ca I λ6493.78, Fe I λ6494.98, Ba II λ6496.897, Fe I λ6498.94, and Ca I λ6499.65 (plus weaker lines of Fe I and Ti I, see Fig. 14). The bulk absorption of all lines in this "quintet" is a strong, characteristic feature in the spectra, which represents well the overall strength of metallic lines in the spectrum. This closely-spaced group of lines becomes easily blended with even moderately fast rotation, in which case EWs are not easily computed for the individual lines: this is again an instance where the use of a spectral index becomes of advantage.

We first define an index which measures the total intensity of the "quintet" lines as

$$\beta_t = \langle f^A \rangle / \langle f^B \rangle, \tag{7}$$

where the *A* and *B* wavelength ranges are defined in Table 1. The *B* range has the role of a reference (pseudo-)continuum. With reference to Fig. 14, the *A* range is comprised of the cyan-colored bands (and the yellow region bracketed by them), while the reference continuum is extracted from both green-colored regions on the two sides. The black spectra shown in the figure are ordered in a temperature sequence (increasing from top to bottom, from early-M to late-G types); prominent spectral lines are also indicated. Here and in following analogous plots, a temperature sequence for MS/PMS stars is defined on the basis of the μ index for late-type (M) stars, and on the basis of $V - I_c$ color for hotter stars, extinction toward these stars being low and uniform enough for a good correspondence between optical color and temperature (Sect. 2). The meaning of the yellow-colored bands, and of the red-colored spectra will be explained


Fig. 12. The "chromospheric", narrow Hα index α_c vs. $V - I_c$ color. Symbols as in Fig. 1.

(green circles rightward of the dotted vertical line). Most cluster stars have a strong narrow Hα emission, but comparatively few γ Vel cluster stars have CTTS-like Hα emission. Note also the very tight (reddening-independent) correlation between α_c and α_w for the early-type stars (cyan dots), with the notable exception of a few outlier datapoints. Explanations for these latter may include chromospheric Hα emission cores (as, e.g., for the candidate early-type members), or fast rotation, present in several of the earliest-type stars shown. Again, a detailed study of these outliers is deferred to a future work.

Hα wings for stars colder than early-A (namely, all stars in our dataset) are reported to be a gravity-insensitive feature (e.g., Gray & Corbally 2009); they are also metallicity-independent,

Fig. 14. Atlas of spectra in the 6485–6510 Å region, containing the "quintet" of strong Ca I, Fe I, and Ba II lines. These and other prominent lines are indicated near the bottom axis. Normalized, telluric-line corrected spectra for MS stars are shown in black, in a temperature sequence (hotter to the bottom), and offset by 0.5 units for clarity. Red spectra are for giant stars at similar temperatures as the respective MS spectra. Gravity-sensitive lines stand out clearly from the comparison. Spectral ranges used to compute the β_t index are indicated with cyan color (and the enclosed yellow range), while green ranges indicate the index reference continuum. Yellow ranges are instead used to compute the β_c index, with the same reference continuum as for β_t.

Fig. 15. Total "quintet" intensity index β_t vs. $V - I_c$ color, with the usual meaning of symbols.

below. Stars of the earliest spectral types are not included among the spectra shown here: they exhibit a gradual increase in the intensity of the "quintet" lines, from the earliest types toward intermediate-type stars.

The usefulness of the β_t index just defined becomes clear when plotting it vs. the $V - I_c$ color (Fig. 15). Considering for the moment only cluster members, which especially near solar temperatures have near-ZAMS gravities, we observe a very marked monotonic decrease in the β_t index, starting from its "neutral" value $\beta_t = 1$ at early-A types toward a minimum value of $\beta_t \sim 0.85$ right close to the transition between intermediate-type and late-type (M-type) stars, where molecular bands start to appear. In particular, β_t shows a well-behaved decrease in the "gap" not covered by either α_w nor μ indices: β_t provides therefore a good, highly significant T_{eff} indicator for intermediate-type stars. The ensuing increase toward unity for colder stars does not introduce ambiguity, since the μ index is able to discriminate effectively stars on the two sides of the β_t minimum. We cannot make any statement at the moment about the large cloud of (orange/gray) datapoints around $V - I_c \sim 1.5$ above the β_t minimum, since they are (background) giants, for which their reddened $V - I_c$ color is not an useful quantity.

We come now to consider the red-colored spectra shown in Fig. 14: in general, they exhibit overall similarities to the respective overplotted black-colored spectra, chosen of similar effective temperatures, as estimated from the μ index for late-type stars and overall spectrum appearance for hotter stars. The "black" and "red" series of spectra belong respectively to the lower and upper branches in Fig. 8 (lower-right panel), which were argued in Sect. 4.1 to correspond to cluster (and MS) and giant stars, respectively. Therefore, the comparison between
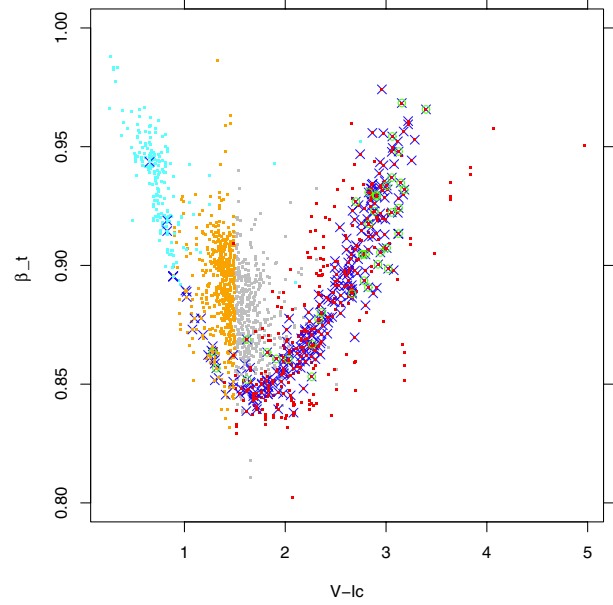
overplotted black and red spectra in Fig. 14 enables us to study gravity effects in the "quintet" lines. It is immediately clear that most of the quintet lines are highly sensitive to gravity: in particular, the two Ca I lines become weaker in giants than in MS stars (high-gravity lines), while on the contrary the Ba II and Fe I $\lambda6498.94$ are enhanced in giants (low-gravity lines). The Fe I $\lambda6494.98$ behaves in an intermediate way, as a high-gravity (henceforth high-g) line in G stars (bottom spectrum in Fig. 14) while as a low-gravity (low-g) one in M stars (top two spectra in figure). Since high-g lines in G stars are relatively rare in our wavelength range, we put this line into the high-g line group. Comparing the MS-star spectra (black) with overplotted giant-star spectra (red) shown in the figure (especially the topmost ones), it is evident that in MS stars the quintet is dominated by the outer (Ca I) lines, while in giants it is dominated by the inner, "core" lines. This simple observation permits to use this line group as a quick and easy mean to visually discriminate between dwarfs and giants in the low-mass range. Accordingly, we have defined a new "quintet core" index β_c, this time using only the yellow-colored region in Fig. 14 (see also Table 1). Since the high-g Ca I $\lambda6499.65$ line is very close to the low-g Fe I $\lambda6498.94$ line, the boundaries of the "core" region have been set with great care. To compute the β_c index we have added to low-g lines in the quintet "core" region also the Co I $\lambda6490.34$ and Ti II $\lambda6491.56$ lines falling in the yellow-colored region, blueward of the quintet proper, whose dependence on gravity is also evident from Fig. 14. In order to obtain the best results for the G-star range, a weighted-mean index was found to be most useful, of the form

$$\beta_c = \left(7/8 \times \left\langle f^A \right\rangle + 1/8 \times \left\langle f^{A^1} \right\rangle \right) / \left\langle f^B \right\rangle, \tag{8}$$

where the A and A^1 wavelength ranges refer respectively to the quintet "core" and to the blueward, additional region, respectively. The β_t and β_c values are reported in Table 3. The observed dependence of the β_c index on $V - I_c$ color is shown in Fig. 16. An extremely clear separation can be seen between cluster stars and giants, especially in the M-star range, with the former stars having always $\beta_c > 0.87$, while giants having β_c values lower by 0.05–0.1 or more. But this diagram shows also
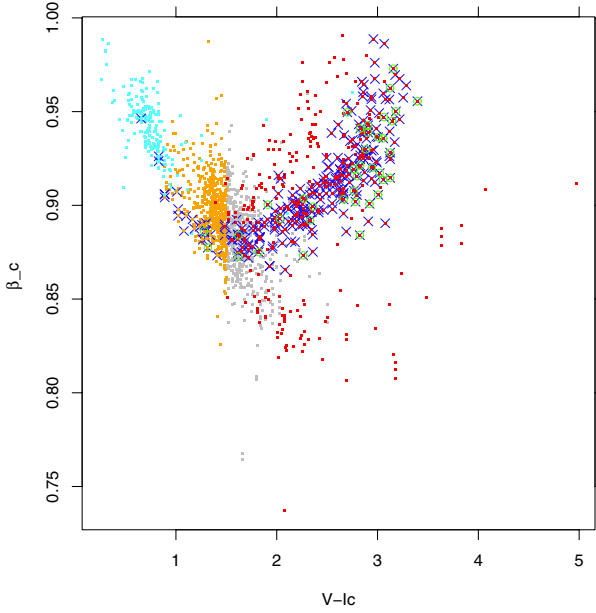
Fig. 16. "Quintet core" index β_c vs. $V - I_c$, showing the strong gravity-related differentiation of late-type stars for $V - I_c > 1.5$.
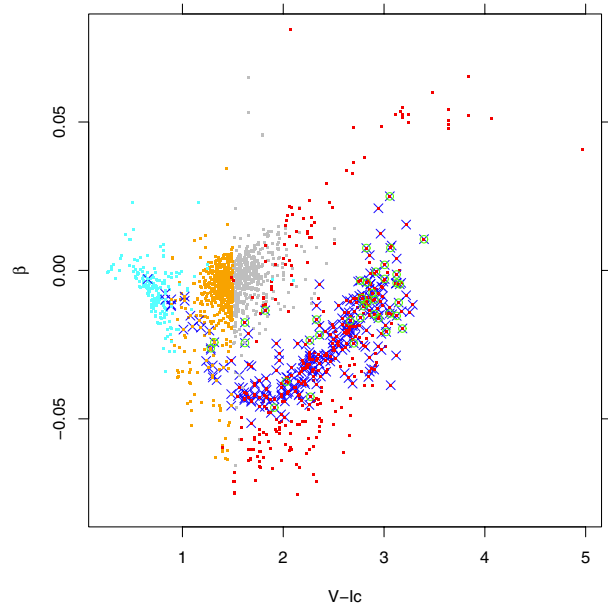
Fig. 17. Quintet "core/edge" ratio index β vs. $V - I_c$, which best defines gravity differentiation at all spectral types.

a most interesting separation between β_c values of cluster members and other M stars on the opposite side with respect to giants: the most plausible interpretation of this separation is that the β_c index is able to tell apart the slight gravity difference between MS and PMS stars, in the M-star range. To our knowledge, gravity differences between MS and PMS late-type stars have never been measured before using this wavelength range. This has been done, instead, using better-known gravity diagnostics such as the Na I lines at 8183–8195 Å (e.g., Mohanty et al. 2004; Lyo et al. 2004, 2008; Riddick et al. 2007; Lawson et al. 2009). A thorough investigation of the diagnostic capabilities which may be offered by the "quintet" lines is therefore most interesting.

The contrasting properties of low- and high-g lines in the quintet are best put into evidence by using a "relative difference" index, which we now define as

$$\beta = (\beta_t - \beta_c)/\beta_t, \qquad (9)$$

and whose dependence on $V - I_c$ is shown in Fig. 17. This figure, where giants are now placed above the MS/PMS stars, shows again clearly the MS/PMS separation for M stars with $V - I_c < 2.6$, but also that the index β is able to discern MS from PMS stars even through the intermediate-type range (orange dots), with higher-gravity MS GKM stars describing a locus in the diagram below that occupied by cluster members of same $V - I_c$ colors. The β values are reported in Table 3. Maximum 1σ errors (at minimum $S/N = 15$) for β_t, β_c, and β are 0.01, 0.013, and 0.012, respectively. It is worth remembering that such relatively large errors are only appropriate for the lowest-mass cluster members with lowest S/N values, while for most other stars in our dataset, especially those of early types, S/N values are much higher than 15, being the median $S/N \sim 65$. Note also that the quintet spectral region may be affected by many telluric lines (Fig. 3), and their subtraction is therefore particularly important to compute β_t and β_c most accurately.
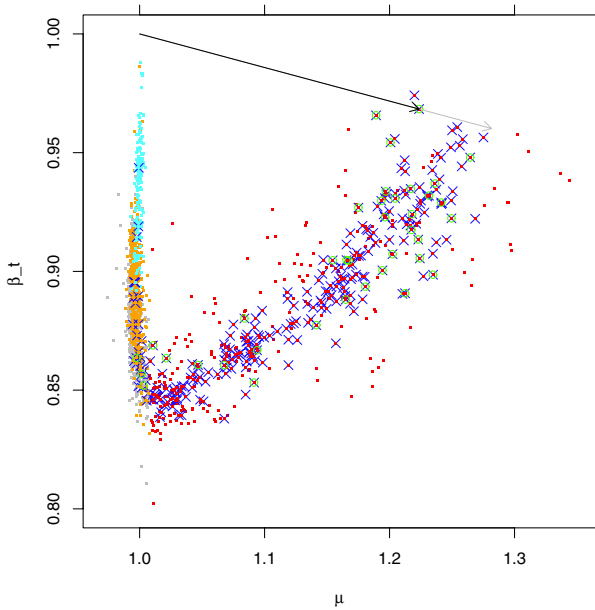
Some warnings about the β_c (and thus β) index are however necessary: first, while the total quintet index β_t is not very sensitive to fast rotation, the closeness in wavelength between high- and low-g lines used to compute β_c makes that index

rather sensitive to fast rotation (above $\sim$30–50 km s^{-1}), since in this case adjacent rotation-broadened lines tend to merge, and cross-contamination between the low-g and high-g bands make the β_c index approach its "neutral" value of unity (the neutral value of β is instead zero). This rotation effect may be partially responsible for the large scatter of β_c near $V - I_c \sim 3$ for cluster members (Fig. 16), since these stars are mostly fast rotators (Fig. 2). Moreover, the Ba II λ6496.897 line was found to be enhanced in young star clusters, and might be affected by NLTE effects, especially in young stars with strong chromospheric activity (D'Orazi et al. 2009b, 2012, and references therein), and this may also contribute to the scatter seen in Figs. 16 and 17. Second, the Ba II λ6496.897 line is one of the most gravity sensitive lines in the quintet "core" region, but it may be strongly enhanced also in the so-called barium stars, leading to completely spurious values for the β_c index. These stars are however rare, and none appears to be present in our dataset. Since they are known to have high abundances not only of barium but also of other s-process elements such as strontium and yttrium, examination of lines of these elements (a few of which are found in the HR15n range) is needed to determine whether a star with a strong Ba II line is a barium star or a low-gravity star. Finally, indices β_t, β_c, and β are expected to be highly sensitive to metallicity, as will be discussed in Sect. 7.2.

Having already defined temperature indicators such as the α_w and μ indices, it is now possible to compare the "quintet" indices with them, in completely reddening-free representations. A (β_t, α_w) diagram is shown in Fig. 18, excluding late-type (M-type) stars for clarity. This figure shows that the decrease in β_t with α_w (thus, with temperature) is not uniform, but shows a sort of plateau, with a non-negligible spread of datapoints; this might be due to metal abundance effects, and/or to gravity. Candidate cluster members fall, with one exception, well within the main band comprising most stars in the sample, and fit comfortably the picture where deviation from this main locus are only due to gravity or metallicity, both of which are expected to be (nearly) constant for cluster stars in this mass range. The locus of orange datapoints (mostly giant stars) above the position of cluster stars might be ascribed to both low-gravity effects,
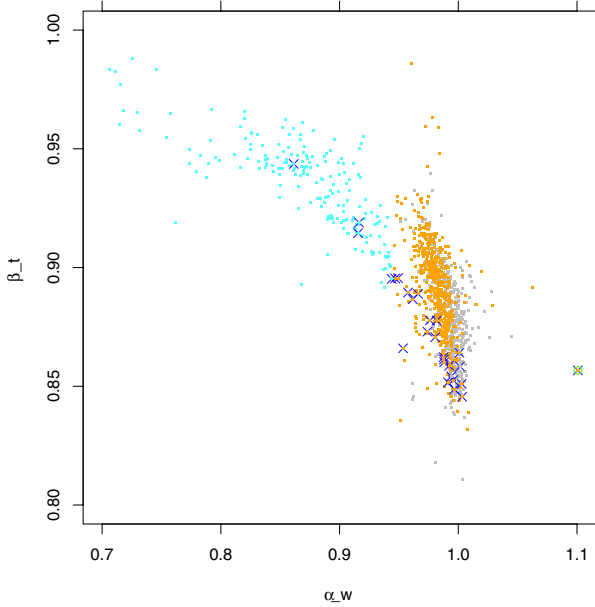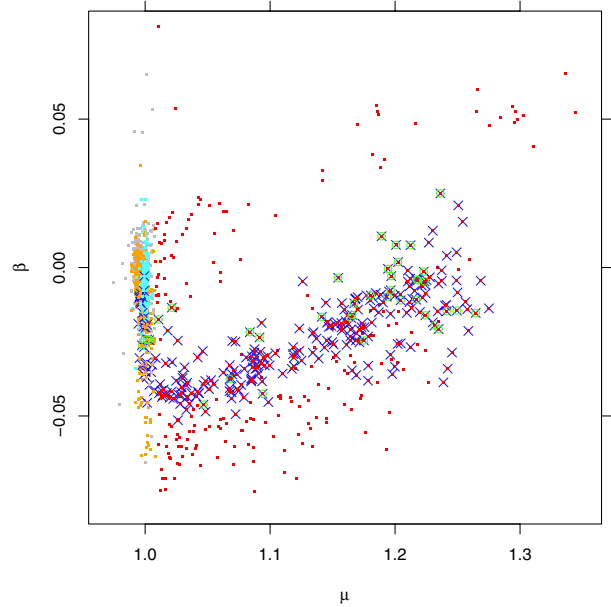
Fig. 18. Index β_t vs. the temperature-sensitive Hα wings index α_w. Late-type stars (comprising most emission-line CTTS) are not plotted.

Fig. 20. Gravity index β vs. μ. This reddening-free diagram shows clearly the difference between gravities of MS and PMS late-type stars, and even more between these and giant stars.

Fig. 19. Index β_t vs. the temperature-sensitive TiO index μ. Heavily veiled CTTS, if present, would fill the empty triangular region, converging toward the point $(1, 1)$. The procedure for determination of veiling r is exemplified by the comparison between the black arrow and its gray prolongement; see text for details. At most two-three moderate-veiling stars may be present in this dataset, near $\mu \sim 1.2$.

or to reduced metallicity. This latter effect is almost surely responsible for the few orange datapoints with $0.95 < \alpha_w < 1$ and $\beta_t > 0.94$. A study of these interesting outliers, and of similar ones below the main band in the figure, is however beyond the scope of this work, and will be made in a future work; some insight on their nature will be nevertheless gained from suitable reference spectra in Sect. 7.1.
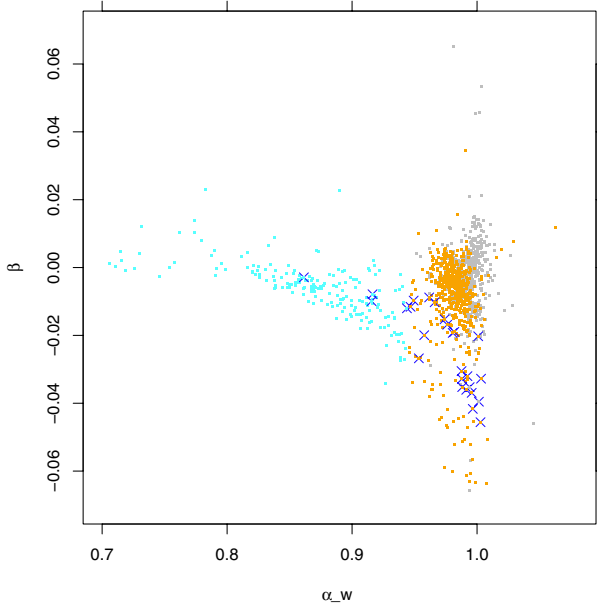
Next, Fig. 19 shows a (β_t, μ) diagram describing the behavior of late-type stars in a reddening-independent way. While low S/N is a limiting factor for the reddest stars, the figure shows nevertheless a practically empty triangular region, with only a
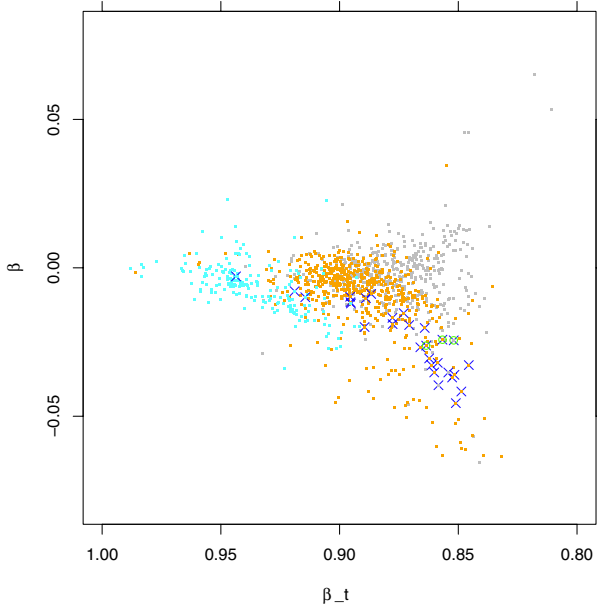
few non-member stars in it. We recall that the neutral value of both β_t and μ is unity, i.e. the value approached only by the most massive stars in the dataset. This value would also be approached by heavily veiled PMS stars, which are to be found (exclusively) among CTTS (green circles): the fact that CTTS datapoints in this cluster stay away from the central part of this diagram, but on the contrary follow the same locus as other, non-CTTS, cluster members, implies that no significant veiling is present in their spectra. The only possible exception are the 2–3 CTTS with $\beta_t > 0.95$, for which at most a small veiling factor $r \sim 0.2$ may be derived. The procedure for quantitative determination of veiling r is exemplified in the figure, by the comparison between the black arrow (joining the neutral point with the measured position in the diagram for a CTTS) and its gray prolongement (extrapolated up to the cluster locus): the length ratio between them is $1{:}r$ (see Eq. (3)). It should be noted that the procedure just outlined becomes unreliable (and overestimates r) for very fast-rotating stars, whose indices are compromised as already explained.

We now turn our attention to the gravity index β, as a function of different temperature indices. First, a (β, μ) diagram is shown in Fig. 20, which again shows the good separation between MS, PMS, and (especially) giant stars already seen in Fig. 17, but here in a reddening-independent way. While reddening is not of great concern for the "clean" case of γ Vel stars, it is of great importance and nuisance for many other (younger) clusters such as Cha I, and therefore we devote some attention to build reddening-independent diagnostics, with a more general purpose in mind than the study of γ Vel alone. That the power of the β index as a gravity diagnostics extends to intermediate-type stars as well as to M stars is demonstrated by the (β, α_w) diagram of Fig. 21 (excluding M stars). The MS locus is clearly seen, starting at $(\beta, \alpha_w) = (0, 0.7)$ and bending downwards (orange datapoints) in a regular way; the bulk of giants (orange/gray) remain instead near $\beta \sim 0$, well above MS stars with the same α_w index. Cluster stars of intermediate type fall in between, where they are expected to lie, just below the envelope of giant stars (i.e., with $\log g$ just above them, see Fig. 4). The few orange
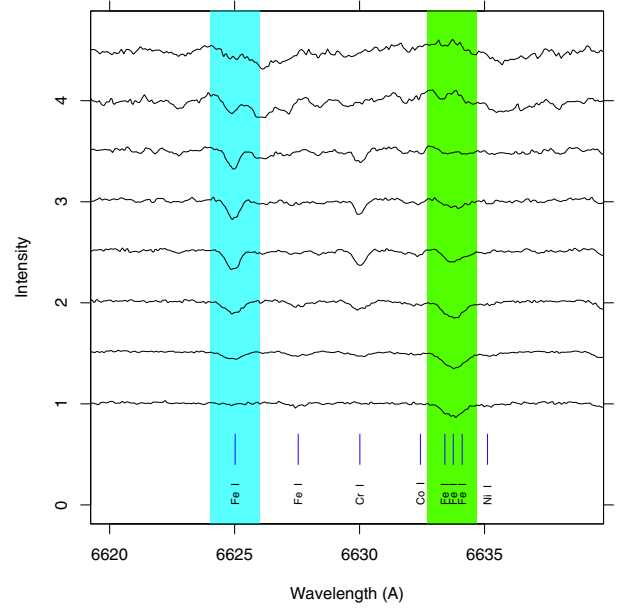
Fig. 21. Gravity index β vs. α_w, not showing late-type stars. Difference in gravities between intermediate-type MS, PMS, and giant stars are also clear from this diagram.

Fig. 22. Index β vs. total quintet index β_t, the latter measuring temperature in intermediate-type stars.
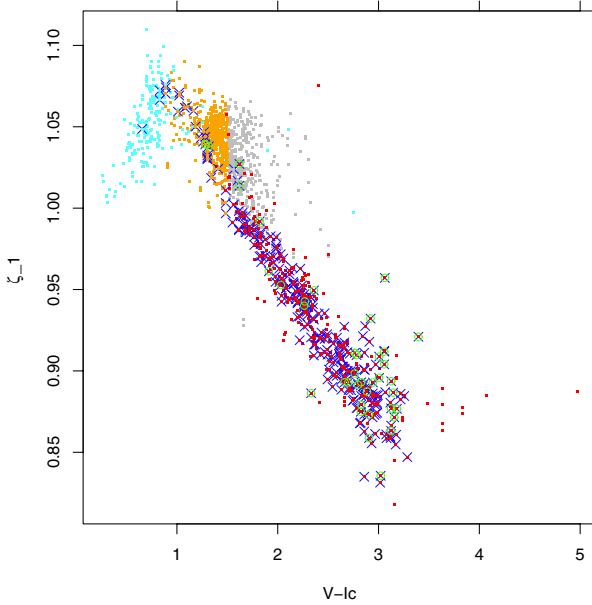

Fig. 23. Atlas of spectra of intermediate-type and late-type cluster members in the range 6620–6638 Å, showing the wavelength ranges used to define our index ζ_1, containing Fe I lines and also sampling a TiO molecular jump, as evident from the two topmost spectra. Spectra form a temperature sequence, hotter to the bottom. The green (cyan) band indicates the range used for high- (low-)temperature lines.

4.4. Temperature-sensitive features near 6630 Å

We have then considered a set of additional lines, useful to compute a further index, sensitive to temperature in intermediate-type stars. Not many lines are found in the HR15n range to this aim, since most lines exhibit an intensity peak in this T_{eff} range and are no good temperature indicators. The lines chosen here are all Fe I lines, $\lambda\lambda 6625.022$, 6633.412, 6633.749, and 6634.106. Figure 23 shows the relevant spectral region for a set of cluster member stars, with temperatures increasing from top to bottom according to $V − I_c$ color (the three lowest spectra are GK stars, the topmost five are M stars). We compute an index ζ_1 as

$$\zeta_1 = \langle f^A \rangle / \langle f^B \rangle, \tag{10}$$

with A and B ranges defined in Table 1. We see that the $\lambda 6625.022$ line has a strongly different temperature sensitivity than the other three (unresolved) Fe I lines near 6634 Å. In the coolest stars (top two spectra in figure) all these lines have largely disappeared, but in their place the two extremes of a molecular TiO band are found: this chance coincidence has the favorable effect that the trend exhibited by the ζ_1 index with $V − I_c$ color continues monotonically beyond the intermediate-type stars, until the latest spectral types considered. This is shown in Fig. 24: after a short rise in the early-type range, this index attains its maximum values for early-G stars (cyan-orange dots transition), to decrease sharply and monotonically throughout all lower-temperature stars. No pronounced gravity effects are apparent: for instance, no separate MS and giant branches are identifiable in the figure. Metallicity effects can be expected, but are not obvious from the figure. The temperature dependence of the ζ_1 index for intermediate-type stars is therefore useful to reinforce temperature indications obtained from the β_t index. It is also worth noting that the TiO band giving the ζ_1 index its extended cool-star temperature sensitivity was not included among
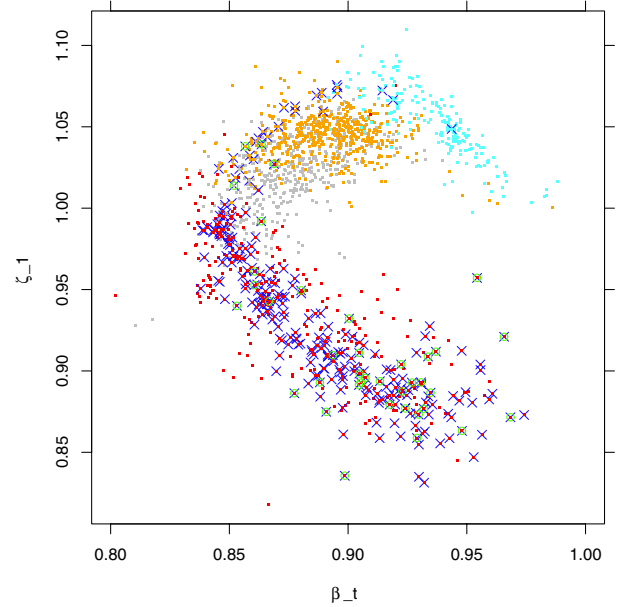
and gray outliers with $\beta > 0.03$ are again interesting peculiar stars, with strongly enhanced low-g lines, which will be studied elsewhere.

Since the α_w index may not be a good T_{eff} indicator for intermediate-type stars, we use instead the β_t index in this mass range. Figure 22 is a (β, β_t) diagram, again excluding M stars. Again a separation between MS, PMS, and giant stars is observed, with PMS cluster stars distinctly above higher-gravity MS stars, which confirms the usefulness of such representation. Some mixing can be seen between giants and earlier-type MS stars (as well as PMS stars) and might be due to a dependence of β_t on metallicity (or $\log g$) as well as on T_{eff}.

Fig. 24. Behavior of the ζ_1 index vs. $V - I_c$. Note the strong, monotonic temperature dependence from early-G types down to the latest-type sample stars.

Fig. 25. A ζ_1 vs. β_t diagram. MS and PMS stars define a characteristics C-shaped pattern. Veiled CTTS can be easily recognized since they would depart from that locus toward point $(1, 1)$, and their veiling r would thus be measured. Again, only two such stars are present in the sample.

those sampled by our μ_n indices, and therefore this new index provides also a new, independent $T_{\rm eff}$ diagnostics for M stars as well. Maximum 1σ errors on ζ_1 are estimated to be 0.018, for the latest-type cluster members. Being defined using narrow wavelength intervals, the ζ_1 index is affected by fast rotation above $v \sin i \sim 50$ km s^{-1}. The ζ_1 values are reported in Table 3.
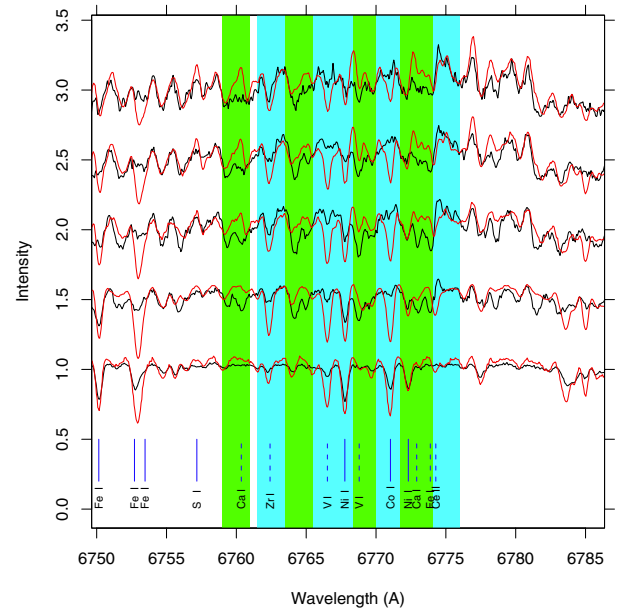
The fact that the β_t index departs increasingly from unity, going from early-G to early-M stars, while ζ_1 approaches unity across the same spectral-type range, has the interesting practical consequence that the comparison between these two indices may be used as an effective veiling diagnostic. This is demostrated in Fig. 25: in this (ζ_1, β_t) diagram, cluster datapoints follow a very characteristic C-shaped pattern, while the locus of giants is slightly offset. Apart from early-type stars (cyan dots), or likely metal-poor giants (orange dots mixed with cyan dots), no other stars fall near the neutral point $(\zeta_1, \beta_t) = (1, 1)$. Veiled stars would depart at almost right-angles from the PMS locus, outlined by non-CTTS cluster stars, toward this neutral point, by an amount proportional to veiling r (see Eq. (3)). The C-shaped pattern means that veiling-related effects are non-degenerate with respect to temperature effects, for intermediate- and late-type stars in a cluster. In γ Vel, this plot shows again that veiling may be present at most in two cluster CTTS, with values between $r \sim 0.2$–0.5. The independent veiling measurements obtainable from the (ζ_1, β_t) and (β_t, μ) diagrams (see Fig. 19) can also be of great help in estimating errors on veiling r.

4.5. Gravity-sensitive features in the 6750–6780 Å region

Now we consider a wavelength region in the reddest part of the HR15n range, where many very interesting gravity-sensitive lines are found. Figure 26 shows a number of spectra for intermediate- and late-type MS stars (black) and giants (red), in a temperature sequence (increasing from top to bottom). We see that there are extreme differences in individual lines between MS stars and giants, despite the same temperatures as measured from the TiO bands (and the μ index). Most striking is the almost complete suppression of the $\lambda\lambda 6766$, 6771 lines in MS stars,


Fig. 26. Atlas of MS (black) and giants (red) spectra in the wavelength range 6750–6785 Å, used to define the γ_1 gravity-sensitive index. Lines with better-known parameters are indicated at the bottom with solid blue segments, while some lines with less certain parameters are indicated with dashed segments. Strongly gravity-dependent (low-g) lines are evident. Cyan- and green-colored wavelength ranges are used to sample respectively low-g and high-g lines in the γ_1 index definition.

while the same lines are quite strong in giants. Low-g lines are also found at $\lambda\lambda 6762$, 6767.5, although not as strongly affected as the former two. The identification of some of these lines is not certain: the Co I $\lambda 6771.033$ and Ni I $\lambda 6767.768$ lines are identified with better confidence, while the identification with Zr I $\lambda 6762.413$ and V I $\lambda 6766.519$ is much less certain (as are
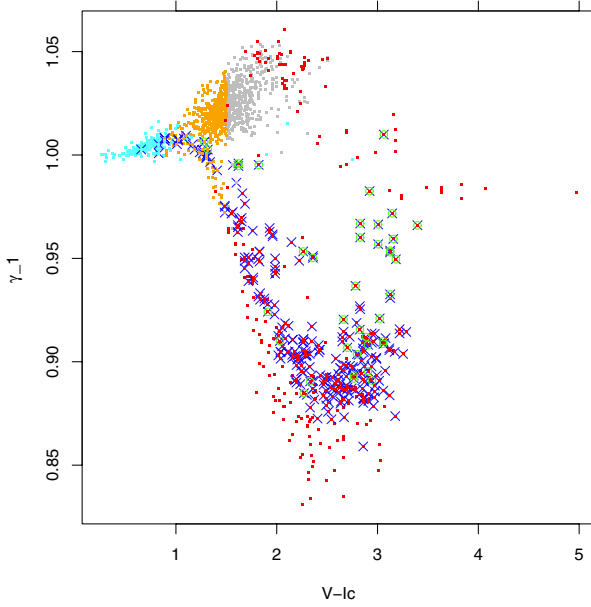
Fig. 27. The γ_1 gravity-sensitive index vs. $V - I_c$ color, showing the extreme difference in γ_1 values between giants and MS stars, and also the MS/PMS separation.
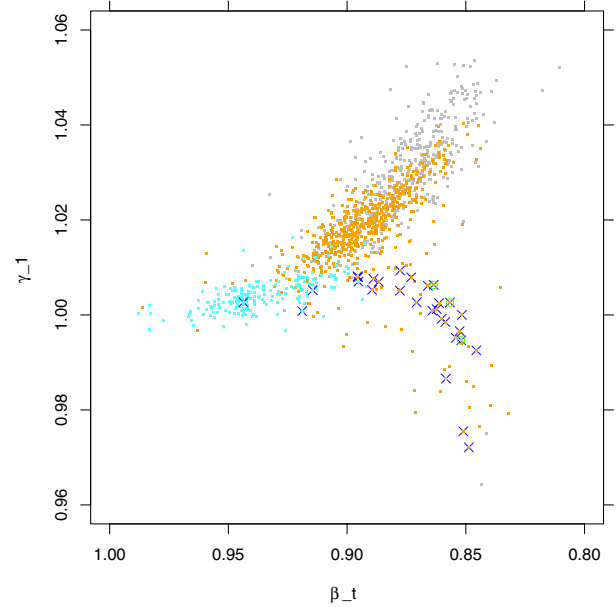
Fig. 28. The γ_1 vs. β_t diagram, showing the effectiveness of γ_1 to discriminate gravities between MS, PMS, and giants also in the case of intermediate-type stars, with β_t acting as a temperature index. Late-type stars are not shown.

the atomic parameters of the two latter lines); other lines may also contribute to the observed absorption features.

We define a new index which takes advantage of these strongly gravity-sensitive lines, from the flux ratio between the low-g line ranges (cyan-colored wavelength ranges in Fig. 26), and contrasting high-g features nearby (green-colored ranges in the figure). The new γ_1 index is then defined as usual

$$\gamma_1 = \langle f^A \rangle / \langle f^B \rangle, \qquad (11)$$

with the A (high-g lines) and B (low-g lines) wavelength regions defined in the figure and in Table 1. Because of the closeness between the high-g and low-g ranges (in fact, they alternate in a comb-like pattern) and their relative narrowness, the γ_1 index becomes sensitive to rotation (like the β index): high-g and low-g contributions tend to mix together, and the index tends toward its neutral unity value for fast rotators. Maximum statistical 1σ errors on γ_1 are on the order of 0.015. The γ_1 values are reported in Table 3.

The behavior of γ_1 vs. $V - I_c$ color is shown in Fig. 27: the extreme MS vs. giants differences visible in Fig. 26 are here mirrored by the huge gap between late-type giants and MS stars. Again, PMS stars form a band above that of MS stars, up to $V - I_c \sim 3$, although the distinction is not as clear as when using β in the late-K range (transition between orange and red dots). The rotation effect on γ_1 may be seen for some fast-rotating CTTS stars near $V - I_c \sim 3$, which tend to mix with giants as their γ_1 index is "diluted" toward the neutral value of unity.

A reddening-free diagram of γ_1 vs. β_t is useful to better inspect the index behavior for intermediate-type stars, and is shown in Fig. 28: the distinction between giants (with γ_1 increasing with lower temperatures), PMS stars (γ_1 first flat, then mildly decreasing), and MS stars (γ_1 decreasing with lower temperatures) is very noticeable, and confirms the usefulness of this index.

4.6. Global temperature and gravity indices

In the previous subsections we have introduced four temperature-sensitive indices: the Hα wings index α_w for early-type stars, the total "quintet" intensity index β_t and the Fe I ratio index ζ_1 for intermediate-type stars, and the TiO band index μ for late-type stars. Moreover, the quintet "core/edge" index β and the γ_1 index have been shown to be very good gravity indicators. Here we attempt to build more global temperature and gravity indices, starting from those already introduced.
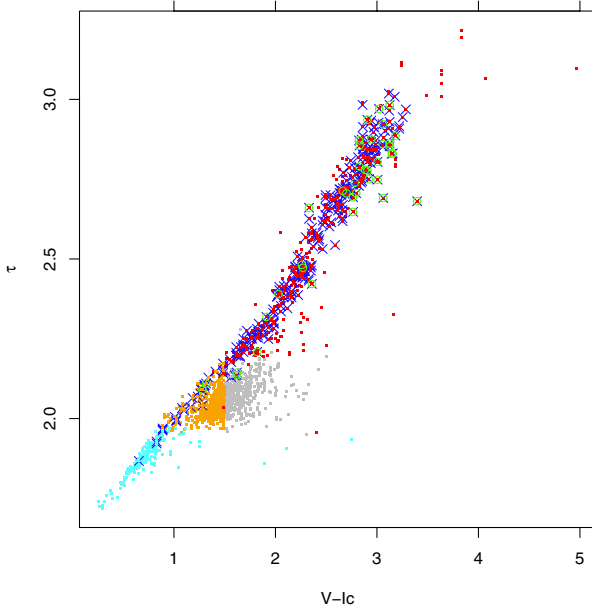
We define a new composite index τ as

$$\tau = \min(\alpha_w, 1) - \beta_t - \zeta_1 + 3 \times \mu. \qquad (12)$$

The α_w index is used here only for its sensitivity to the absorption wings of early-type stars, while in cases where $\alpha_w > 1$ (fast-rotating WTTS and especially CTTS) it is "reset" to unity, since in those cases it is no temperature indicator. In the three broad spectral-type ranges we have studied, individual contributions to index τ behave as follows:

- For early-type stars, α_w is the main contributor to τ; the contrasting contributions of β_t and ζ_1 tend to cancel each other out, and μ is flat and irrelevant.
- For intermediate-type stars, α_w and μ are flat, and contributions from β_t and ζ_1 reinforce each other.
- For late-type stars, α_w is flat, and the strong contributions by (three times) μ and (minus) ζ_1 more than overcompensate the opposite contribution by β_t.

Maximum 1σ errors on τ are on the order of 0.026. The net result is shown in Fig. 29: the strong, direct, almost linear correlation with $V - I_c$ across the whole sampled color range leaves little doubt about the real usefulness of the τ index just defined. It also argues in favor of a nearly uniform reddening for γ Vel cluster stars (except perhaps for the latest-type cluster members, as already noted), without which no such narrow correlation would have been obtained. The two CTTS falling below the main band near $V - I_c \sim 3$ are those stars for which a non-zero veiling

Fig. 29. Composite temperature index τ vs. $V - I_c$, for all sample stars.

Fig. 30. Composite gravity index γ vs. temperature index τ, for all sample stars. The gravity difference between MS and PMS stars is best studied by using this reddening-free diagram encompassing all spectral types.

was suspected from previous diagrams; Fig. 29 helps to confirm this fact once again, although in this latter diagram also a high reddening may have a similar effect.

We have noted in the relevant sections that all indices used in the definition of τ are almost entirely independent of gravity, with some dependence expected only for β_t. They are also relatively unaffected by rotation, at least if it does not exceed ~50–90 km s^{-1}. We expect therefore τ to be a quite robust temperature indicator, across the spectral type range sampled by our dataset (mid-A to mid-M), at least for MS and PMS stars whose gravities are not too dissimilar.

We also define a composite index γ using previous gravity-sensitive indices as

$$\gamma = \beta + \gamma_1,\qquad(13)$$

where the two indices β and γ_1 reinforce each other as gravity indicators. Maximum 1σ errors on γ are on the order of 0.019. The τ and γ values are reported in Table 3. Using now directly τ as a temperature proxy, rather than the $V - I_c$ color, we obtain finally a most interesting (γ, τ) diagram, shown in Fig. 30. We regard this (reddening-free) diagram as one of the most important results of this work. The giants are very well separated from higher-gravity stars, at all temperatures for which a separation was expected, starting at early-G types (cyan-orange transition in the figure) and even more for colder stars. Most importantly, the cluster PMS stars (at 7–10 Myr) are quite clearly separated from higher-gravity (by only 0.5–1.0 dex) main-sequence stars, also starting at early-G types. As expected, very fast-rotating PMS stars (green circles near diagram center) have a γ index slightly compromised, and approaching its neutral value of unity: they appear as lower-gravity than they probably are.

To better appreciate the degree of separation between MS and PMS stars, we plot in Fig. 31 the same diagram, but without cluster members. Moreover, we have added symbols for lithium-rich stars (Li $EW > 150$ mÅ, black plus signs), and for chromospherically-active stars (from the Hα core index α_c, green crosses). Five stars have both lithium and chromospheric emission, and might be additional members missed by our (preliminary) member-selection criteria; for instance, they might be binary members that happen to lie outside the X-ray field of
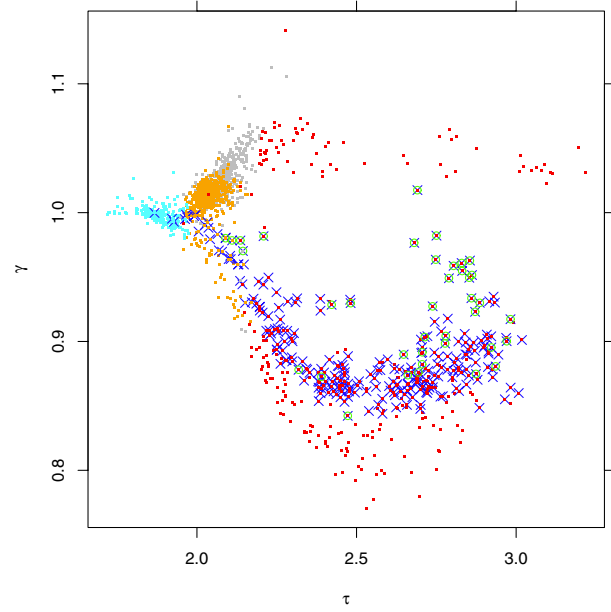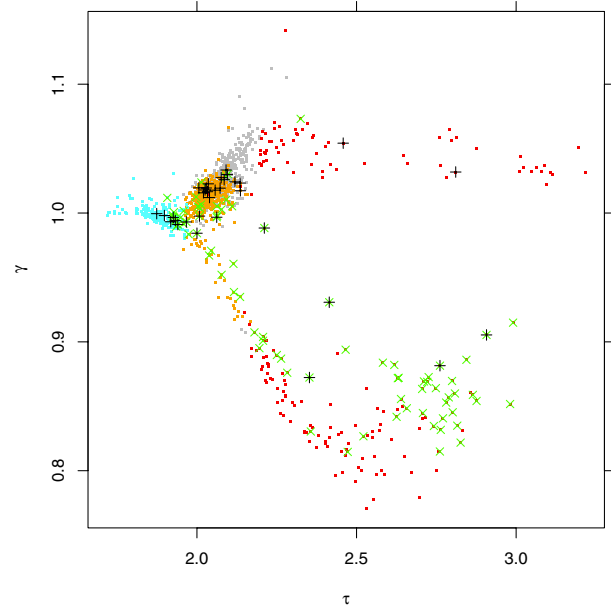
Fig. 31. Same as Fig. 30, but omitting cluster candidate members, to better appreciate the locus of MS stars alone. Stars with lithium $EW > 150$ mÅ are indicated with black plus signs, while those with narrow, chromospheric Hα emission with green crosses.

view. Their position in the (γ, τ) diagram above the MS locus also suggests their being PMS stars. Many giants have also moderately strong lithium lines. Except for the few stars just mentioned, comparison between the diagrams of Figs. 30 and 31 shows that the locus occupied by PMS stars is practically devoid of MS stars up until $\tau \sim 2.6$, and that some overlap between the MS and PMS samples at redder colors (higher τ) is limited to just a few stars, all with strong chromospheric emission. We cannot even rule out that these latter are PMS stars, perhaps older than γ Vel stars and belonging to a dispersed population.

Metal abundance variations among sample stars may be responsible for some scatter of datapoints, in both the MS and giant-stars regions. We also admit that this representation is purposely aimed at characterizing low-mass near-MS stars, and does not do justice to the wide variety of spectral features shown by GK giant stars, which are found in a rather compressed region of the (γ, τ) diagram. Moreover, this latter giant-star region contains the diagram neutral point at $(\gamma, \tau) = (1, 2)$, where extremely metal-poor stars are probably to be found. This emphasizes that this diagram is not suitable to test for chemical abundances (which will be studied in Sect. 7.2). Veiling also would have the effect of making a star converge toward the neutral point: to correct for this, veiling corrections should be made before placing stars in this diagram, with the techniques discussed in the previous sections.

Outliers in the (γ, τ) diagram above the giant-star locus, or above the early-type star locus are the same stars which were outliers in, e.g., the (β, β_t) diagram of Fig. 22. Due to their lack in the studied sample, we could not test the performance of our indices in the case of early-type PMS stars, such as the Herbig Ae/Be stars: in these cases, Hα is mostly in emission, in which case it cannot be used as a T_{eff} indicator via the α_w index. This latter would be probably high enough to signal the star as an accreting star as for CTTS. Assuming that all other indices are unaffected with respect to, e.g., normal A stars, we would find such a star as a (green) datapoint near $(\gamma, \tau) = (1, 2)$, and confirmation of these stars nature will require a careful individual analysis of their spectrum. Again, no such case is found in the γ Vel sample in Fig. 30. Testing these expectations can only be done by using actual spectra of Herbig stars, however.

The usefulness of the (γ, τ) diagram is emphasized when we consider only slowly-rotating stars ($v \sin i < 30$ km s^{-1}), as we do in Fig. 32: here the PMS band becomes significantly narrower than in the complete diagram; the average trend of γ vs. τ is very well defined, distinctly for MS and γ Vel cluster stars, so that a mapping between this plot and the $(T_{eff}, \log g)$ plane becomes a realistic possibility. In order to quantitatively do that, we need to calibrate our γ and τ indices, a problem which will be examined in the next sections. From an empirical point of view, however, the (γ, τ) diagram may retain its usefulness: given the regular progression, at a given temperature (or τ), between the gravities of MS, PMS, and giant stars, we may reasonably expect that the sensitivity of γ to gravity extends to lower-gravity stars than the γ Vel PMS stars. Therefore, we expect that stars in younger clusters than γ Vel, characterized by lower gravities, will form a band at higher γ values: in this way, the (γ, τ) diagram may become an empirical age indicator for PMS stars. It is worth remarking that such a (relative) age estimate would be unaffected by highly nonuniform reddening, as typical of very young clusters, or distance uncertainties, being determined using purely spectroscopic indicators. It may also be helpful as an additional membership criterion, where other membership criteria may fail (e.g., absent lithium for stars in the so-called lithium chasm; inconsistent RVs for individual SB1 binaries; missing X-ray data, etc.).

As a first, tentative test of the (γ, τ) diagram usefulness in this latter respect, we remark that in Fig. 1 six stars, flagged as members, can be seen to lie below the main cluster locus, which means nearer to the ZAMS if they lie at about the same distance as γ Vel. Their placement in the (γ, τ) diagram is shown in Fig. 32 (bold black circles): they all lie at the interface between the MS and the PMS bands, suggesting that their gravities (and ages) are consistently intermediate between γ Vel members and MS stars. This is well consistent with these stars having a young age, but nevertheless older than γ Vel members, and with
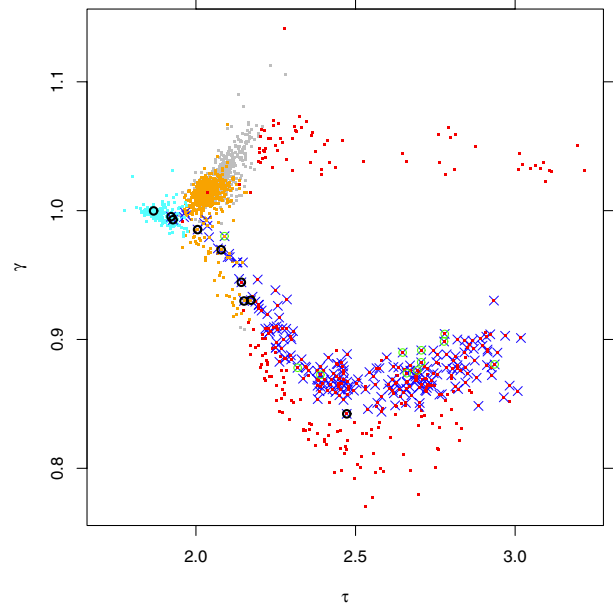
Fig. 32. Same as Fig. 30, but omitting all stars with $v \sin i > 30$ km s^{-1}. The spread of datapoints is significantly reduced with respect to Fig. 30, and the MS and PMS loci better defined. Thick black circles indicate the position of six stars (nine individual spectra), all candidate members, falling near the ZAMS in the CMD of Fig. 1. They here appear to have intermediate gravities between the MS and other cluster members.
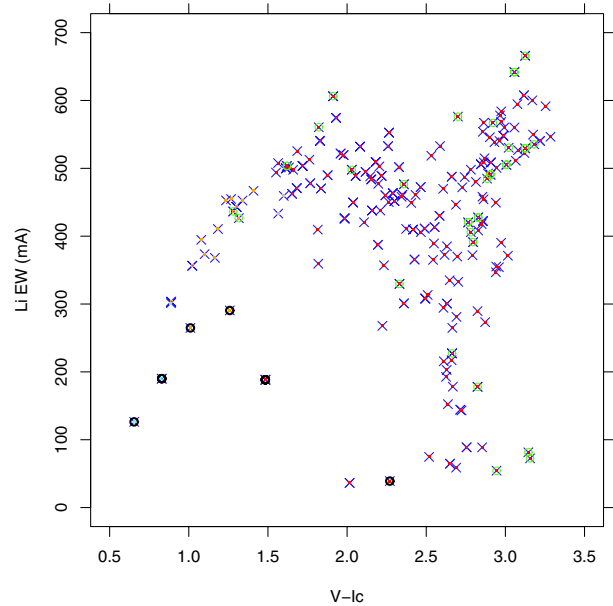
Fig. 33. A lithium EW vs. $V - I_c$ diagram, for members only. Thick black circles indicate the same spectra as in Fig 32.

their belonging to a more dispersed population of PMS stars. To test this further, we show in Fig. 33 a diagram of lithium EW[7] vs. $V - I_c$ color, for PMS stars only (Li-rich giants are therefore not included): while a clear Li-depletion pattern can be seen (to be studied in detail by Franciosini et al., in prep.), the six "older" stars (bold circles) again appear to follow very consistently a different pattern, which according to models is typical of significantly older stars, of about 30–50 Myr (see, e.g., Jeffries et al. 2003). The information which can be obtained from

---

[7] Lithium EWs from release GESiDR1Final, uncorrected for blends.

our (γ, τ) diagram on gravity and age of PMS stars is therefore highly coherent with other evidence, of completely independent origin.

5. Photometric calibration of index τ

While we devote Sect. 7 to calibration of our indices based among others on the *Gaia* benchmark stars, a set of bright stars included in the *Gaia*-ESO Survey whose stellar parameters are accurately known (Jofré et al. 2013, 2014; Heiter et al.; Pancino et al., both in prep.), we have first attempted a calibration of our temperature index τ on the basis of the widely used Kenyon & Hartmann (1995, KH95) color-$T_{\rm eff}$ calibrations. This approach relies on the fact that for γ Vel cluster stars reddening is low and uniform, a fact supported by our data, and on its value as measured by Jeffries et al. (2009). We consider together MS and PMS stars (which have similar reddenings), while we do not use in the calibration giant stars, which may have much higher reddening, and which are easily selected from the (γ, τ) diagram. A few early-type stars may also have large distance and high reddening, but these latter are easily found as outliers in the fit, and discarded. We use de-reddened $V - I_{\rm c}$ colors[8], and the $V - I_{\rm c}$–$T_{\rm eff}$ calibration of KH95 for $V - I_{\rm c} < 1.8$, and that of Stauffer et al. (1998) for $V - I_{\rm c} > 1.8$, which better matches the Pleiades data, to assign a $T_{\rm eff}$ value to MS/PMS stars. The resulting diagram of $T_{\rm eff}$ vs. τ is shown in Fig. 34 (left), together with a seventh-degree polynomial fit. The fact that no separation is seen in this figure between cluster members and MS foreground stars reassures us about the applicability of this calibration to both subsamples. After a first best-fit, datapoints deviant from the fitted values by more than $|\Delta T_{\rm eff}| = 0.04\, T_{\rm eff}$ were discarded, and the fit repeated, with the result being shown in the figure. The final best-fit formula is:

$$T_{\rm eff} = 5\,606\,071.88 - 17\,422\,058.54\,\tau + 2\,320\,6500.2\,\tau^2$$
$$-17\,090\,080.44\,\tau^3 + 7\,496\,636.79\,\tau^4 - 1\,956\,240.22\,\tau^5$$
$$+281\,022.26\,\tau^6 - 17\,141.93\,\tau^7.$$

High-reddening early-type stars are easily seen, as well as two likely veiled cluster stars near $\tau \sim 2.7$. Best-fit residuals are shown in the same figure (right panel); the $|\Delta T_{\rm eff}| = 0.04\, T_{\rm eff}$ limits are shown by the two dashed curves (points outside of the region enclosed by these curves were not included in the fit). For stars inside these limits, the residual standard deviations are 109 K for early-type stars, 73 K for intermediate-type stars, and 50 K for late-type stars. For intermediate- and late-type stars, standard deviations are essentially unchanged when considering only cluster members, while too few early-type members are present to draw solid conclusions about them.

Eventually, we have tested our ability to recover a HR diagram for γ Vel members, correcting the photometric data using $T_{\rm eff}$ as derived from the τ index. Because of the spread of datapoints in the fit above, and the already narrow locus occupied by members in the CMD of Fig. 1, we do not expect this to yield a big improvement in a region with low and uniform reddening like the γ Vel cluster, but there are large potential gains in younger or more distant regions with patchy or higher reddening. We use the best-fit calibration for τ to re-assign a $T_{\rm eff}$ value to each cluster star. Then, using again the KH95 (plus Stauffer et al. corrections) calibration, we compute the expected intrinsic colors $(V - I_{\rm c})_0$; these, together with the observed $V - I_{\rm c}$,
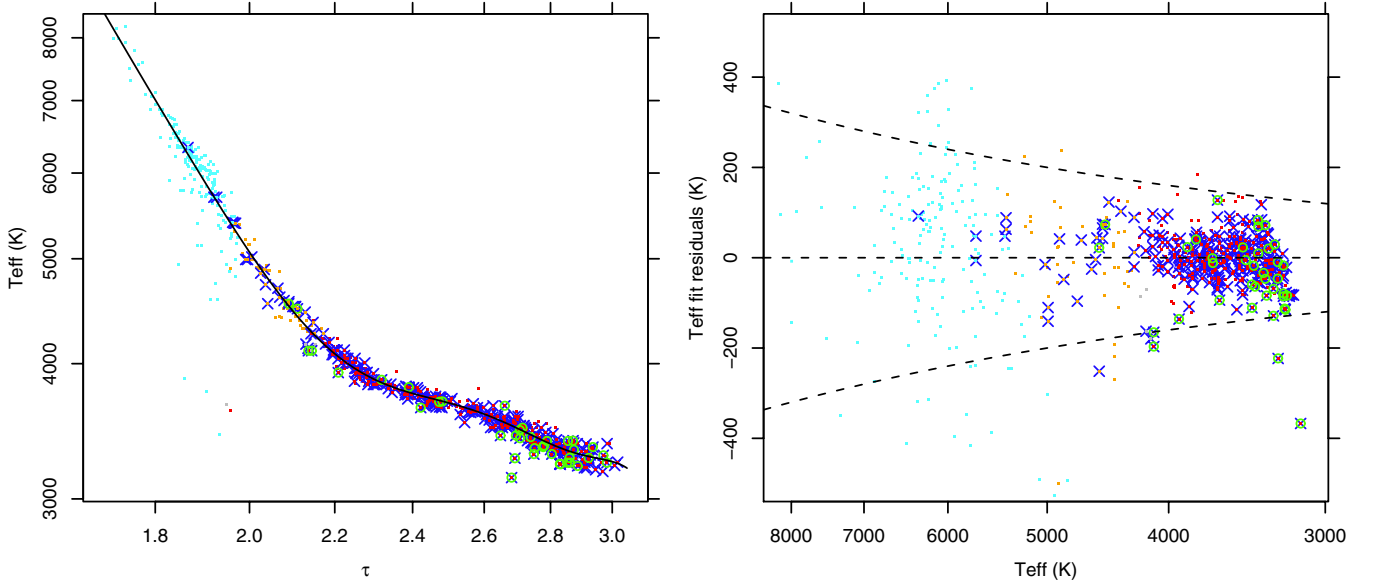
permit to compute individual extinction values A_V for all cluster stars. Using these A_V values, the observed V magnitudes, and bolometric corrections from KH95, we compute bolometric luminosities $L_{\rm bol}$, and are able to construct the HR diagram shown in Fig. 35. Adopting as typical $T_{\rm eff}$ error for the bulk of late-type cluster stars the standard deviation computed above (not the much smaller statistical errors on computed $T_{\rm eff}$), this propagates into median errors of 0.084 mag on $E(V - I)$, and of 0.09 dex on $\log L_{\rm bol}$, comparable to the symbols size in the figure. In the figure we also show the Siess et al. (2000) ZAMS (blue dashed line) and isochrones for ages 5, 10, and 20 Myrs (orange dashed lines). A hint of a binary sequence (or perhaps of an age range) is seen at $T_{\rm eff}$ below 4000 K (despite we left out of our study recognized SB2 stars), where also a narrow cluster sequence is found, well described by the 10 Myr isochrone. Datapoints near the ZAMS (9 individual spectra for 6 stars) are again found, for those stars discussed in Sect. 4.6 to be older PMS stars. Overall, the result is good, and gives us confidence on the reliability of the procedure followed to calibrate $T_{\rm eff}$ in the γ Vel cluster.

## 6. Reference data sets for general calibration

Next, we address the problem of calibrating our temperature and gravity indices in the general case, and also of studying the effect of non-solar metallicities on our indices. Most publically available sets of spectra are of much lower spectral resolution than that of HR15n spectra; this fact renders the use of our indices impossible, since some of them are defined over narrow wavelength intervals, or even adjacent intervals containing lines with strongly contrasting sensitivity to, e.g., gravity. We therefore must consider exclusively intermediate- to high-resolution spectra, of a large number of stars covering a region of the parameter space ($T_{\rm eff}$, $\log g$, [Fe/H]) as large as possible. First, we use the spectra from the UVES Paranal Observatory Project[9] (UVES-POP, see Bagnulo et al. 2003). This set of spectra comprises relatively bright stars (both field and cluster stars), observed with the UVES spectrograph at very high S/N. Only the field stars are considered here, as they cover a wider parameter range (O-M, plus some peculiar stars, Wolf-Rayet, and carbon stars). The spectral resolution of UVES being much higher that that of Giraffe/HR15n spectra, spectral degradation is needed by convolution with a suitable line-spread function (assumed Gaussian). One big shortcoming of the composition of the UVES-POP sample is the lack of main-sequence stars later than about K5. Another issue is the non-homogeneous nature of the stellar parameters, collected from literature without a detailed check, as explained in Bagnulo et al. (2003): a visual inspection of spectra shows indeed that in a few cases the spectral types appear rather inaccurate. Nevertheless, the wide coverage of the ($T_{\rm eff}$, $\log g$) plane makes this set an interesting one for a study of the properties of our indices. Overall, the number of UVES-POP stars with valid data in the HR15n wavelength range is about 300. It is important to realize that the composition of the UVES-POP sample is not representative of the average spatial density of the different spectral types, but instead contains an exceedingly large proportion of peculiar stars, rare Wolf-Rayet (WR) stars, and supergiants; this offers us the opportunity to test the performances of our indices for these rare stellar types.

A much larger set of spectra is available from the ELODIE 3.1 stellar library (Prugniel and Soubiran 2001), containing 1962 spectra of 1388 stars, with a wide coverage in $T_{\rm eff}$, $\log g$, and [Fe/H], spectral resolution $R \sim 42\,000$ and high S/N,

---

[8] We adopt for foreground MS stars the same reddening as for cluster members, since as discussed in Sect. 2 the bulk of the former stars lie at distances close to the cluster itself.

[9] ESO DDT Program ID 266.D-5655.

Fig. 34. Calibration between τ and $T_{\rm eff}$, as derived from observed $V - I_{\rm c}$ colors, average cluster reddening, and KH95 calibrations. *Left*: $T_{\rm eff}$ vs. τ; the polynomial best-fit calibration is shown as a solid line. *Right*: fitting residuals; datapoints outside the dashed curves were not used in the fit.
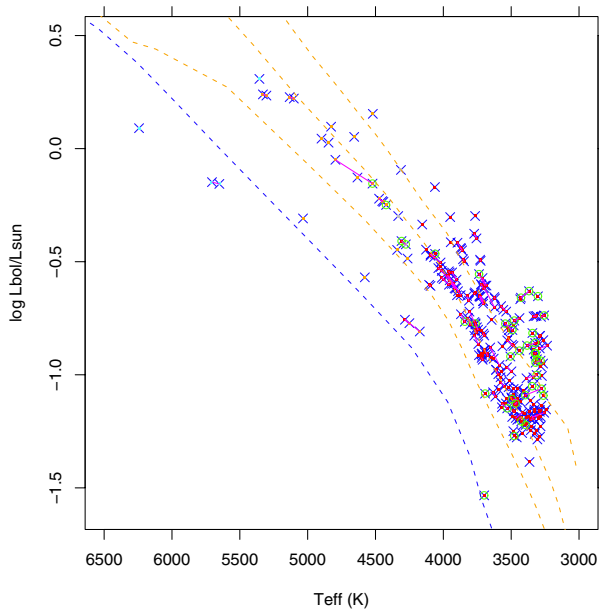
Fig. 35. HR diagram for γ Vel members. The ZAMS is indicated with a blue dashed line. Orange dashed lines are Siess isochrones for ages 5, 10, and 20 Myr. Magenta segments connect different observations of the same stars.

and covering the wavelength range 3850–6800 Å. These spectra are a subset of the complete ELODIE archive, corresponding to stars with best-studied fundamental parameters. Accompanying the library, a table of literature parameters including quality flags helps to select the most reliable measurements, unlike stars in the UVES-POP sample. One shortcoming of the ELODIE spectra, instead, is the way in which telluric-line contamination was treated, namely blanking completely the spectrum in correspondence to known telluric lines: these latter are especially dense in the wavelength region 6490–6500 Å, where the line "quintet" is found (Sect. 4.3), from which the temperature- and gravity-sensitive indices $\beta_{\rm t}$ and β are computed. These indices, computed

from the ELODIE spectra, are therefore slightly altered by such "holes" in their extraction regions, in a non-systematic way because of the lack of correlation between the star radial velocity (RV) and its $T_{\rm eff}$ and $\log g$. In practice, this has a similar effect as a reduced S/N in these particular indices, increasing the scatter of datapoints in the relevant diagrams. We find, nevertheless, that this is not too critical in practice, and we will be able to derive useful calibration information from the ELODIE spectra despite this feature. The ELODIE set of spectra is slightly richer in cold stars than the UVES-POP set, although the number of MS stars cooler than mid-K remains only a handful; moreover, the fraction of peculiar stars appears to be negligible, unlike the UVES-POP set. Overall, the two sets are complementary in several aspects, each one providing useful information on our indices.

To them, we have added about two dozen *Gaia*-ESO Survey benchmark stars (Jofré et al. 2013, 2014; Heiter et al., in prep., Pancino et al., in prep.), which for the time being provide only a limited coverage of parameter space, and are therefore used only as a final check of results obtained using the two larger reference datasets from UVES-POP and ELODIE. Furthermore, recent results from *Gaia*-ESO Survey UVES observations of hundreds stars are used as a check, including a comparison between common UVES-Giraffe targets from the Survey γ Vel dataset. Finally, results from *Gaia*-ESO Survey HR15n observations of young clusters are also examined, since the member population of each cluster constitutes an age- and metallicity-homogeneous sample, and is predicted to lie along definite sequences in the stellar parameter space.

7. Calibration results

7.1. UVES-POP dataset

We present here the analysis of the UVES-POP spectra. For each of them, all spectral indices were computed, following exactly the same procedure (including normalization in exactly the same HR15n wavelength range). RVs needed to place spectra in the stellar rest frames were taken from SIMBAD database, where they are found for only 264 UVES-POP stars. Since the
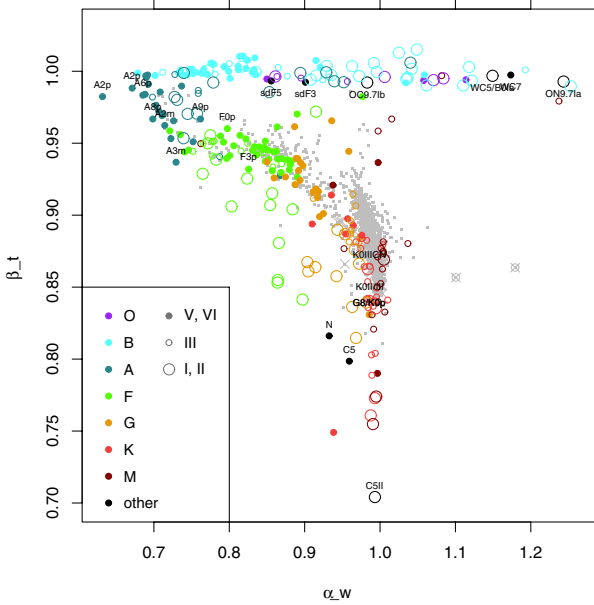
Fig. 36. Index β_t vs. Hα wings index α_w, for UVES-POP stars (colored symbols). Datapoints from the γ Vel dataset are shown in gray (excluding stars of types later than about K7). γ Vel cluster members are indicated by gray crosses, and cluster CTTS in particular by empty gray circles. As explained in the legend, filled colored dots are UVES-POP stars of luminosity classes IV-V (or undefined), smaller empty circles are of class III (including intermediate classes such as II/III, or III/IV), and bigger empty circles are of luminosity classes I-II. Spectral classes are color-coded, as in the legend. Wolf-Rayet stars, OC/ON stars, subdwarfs, and carbon stars are plotted with black symbols. These and stars with peculiar spectra are labeled.

UVES-POP sample lacks entirely MS stars later than mid-K, this dataset is not useful to calibrate indices for γ Vel cluster stars, most of which are in fact later than mid-K; however, we find it useful to understand some other interesting properties of our indices. We start from a diagram of indices β_t vs. α_w, as shown in Fig. 36. This "reversed question mark" diagram is a very important starting point in our analysis. We mentioned in Sect. 4.2 that the system of indices we developed is suitable for stars with $T_{\rm eff} \leq 8000$ K, and this diagram makes it clear why: stars hotter than 8000–10000 K (i.e., OB and WR stars) all belong to the upper strip in the diagram, while cooler stars (such as those in the γ Vel dataset) populate the lower, S-shaped part of the diagram. This pattern is easily understood, by recalling that $\alpha_w = 1$ means a Hα line without broad wings, such as that in K-M stars, while $\beta_t = 1$ means essentially a lack of metallic lines (Ca I, Fe I, Ti I, and Ba II all contribute to β_t), which is found in OB-WR stars, where these elements are found in higher ionization stages, or in very metal-poor subdwarfs, two of which shown in the figure. As temperature decreases from the very highest values found in O-WR stars (which often also have Hα emission, and thus $\alpha_w > 1$), the position of stars in the diagram moves along the $\beta_t = 1$ strip from right to left, until class A0-A2 is reached, where the Hα line attains its maximum width, and the index α_w its minimum value. At the same spectral type, metallic lines start to be relevant in the spectrum, and β_t starts to depart from its neutral value of unity, toward lower values, decreasing monotonically until mid-K types, as explained in Sect. 4.3. With the (β_t, α_w) diagram, we are therefore able to discriminate between stars respectively hotter and colder than type early-A, selecting only the latter ones for analysis using our indices. The diagram should instead not be used to infer a temperature for

OB stars, since for these stars the width of the Hα wings, as measured by the α_w index, is affected by gravity as well as by temperature (e.g., Böhm-Vitense 1989; Gray & Corbally 2009), and also because of the additional complication of Hα going into emission in many OB-WR stars.

There are other interesting lessons to be learned from the (β_t, α_w) diagram of Fig. 36. The S-shaped strip going from early-A to late-G stars is populated (in the UVES-POP sample) by stars belonging to all luminosity classes, from V (filled dots), through III (small empty dots) to I (bigger empty circles); yet, only these latter supergiant stars segregate from class III-V stars, lying lower than the main strip in the diagram. Therefore, the position of stars in this part of the diagram is insensitive to gravity except for supergiant stars; since, as mentioned in Sect. 4.2 and further discussed below, the α_w index is independent of gravity in this spectral-type range, this implies that also β_t is independent of gravity for early-A to (at least) late-K, and luminosity classes V to III. Besides FG supergiants, also KM supergiants are found at lower β_t values than KM dwarfs/giants: β_t values for these latter are usually above 0.83 (Sect. 4.3), while in Fig. 36 a number of supergiant stars are found below that value. The diagram is also useful to select metallic-line Am stars, since they have stronger metal lines (i.e., lower β_t) than expected on the basis of their Balmer lines (i.e., the α_w index). One such example can be seen in the figure. One peculiar A star (type A2p) is also found to deviate from the main strip in the diagram. Carbon stars are also found in a peculiar position in this diagram ($\beta_t < 0.85$ and $0.9 < \alpha_w < 1.0$), near the KM-supergiant locus. Three such stars are labeled "N", "C5", and "C5II" in the figure; one more star in the same part of the diagram (HD 115236), for which a K5 spectral type is listed in the UVES-POP page[10], is instead reported in SIMBAD to have a type of S6/8 B. This latter type explains why the position of this star in the diagram is so different from other K-type stars in the sample, and strengthens our argument about this location in the diagram being typical of carbon stars and similar objects. Because a very large number of absorption lines is present in the HR15n spectra of carbon stars, in excess of those found in "normal" stars, we are unable to state with certainty whether their β_t enhancement is caused by stronger absorption from the same lines as in "normal" stars or by other lines.

Finally, there are a few stars in the gap between the OB-star strip and the solar-star strip: while this is the expected position of mid-late M stars (for which both β_t and α_w tend to unity), for FGK stars this is indicative of low metallicity, as we discuss in more detail below. At very low metallicities, FGK stars may even mix with OB stars in this diagram (as is the case for the two sdF stars labeled in the figure, namely HD 140283 and HD 84937): should this happen, a visual inspection of the spectra themselves would solve the ambiguity, since metal-poor stars will have only very weak lines, while OB stars in the same region of the (β_t, α_w) diagram will show strong lines of He I and ionized metals at the very least near 6678 Å. The ambiguity between late-M and OB stars is instead solved by looking at molecular index μ, which has a value of unity for OB stars, but is much higher for M stars (Sect. 4.1).

Next, we examine the diagram (μ_7, μ_6) of Fig. 37, which describes the behavior of two distinct molecular bands in the HR15n spectral range. In Sect. 4.1, this diagram was the first instance of a gravity segregation between M giants and dwarfs. The UVES-POP sample does not contain any M dwarf, and

---

[10] http://www.eso.org/sci/observing/tools/uvespop/field_stars_uptonow.html
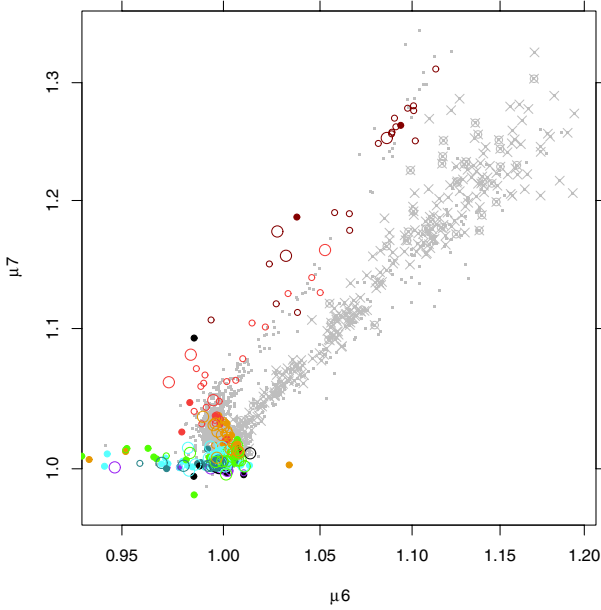
Fig. 37. Plot of μ_7 vs. μ_6 for UVES-POP stars. Note the lack of stars in the region occupied by MS/PMS M stars. Symbols as in Fig. 36, with the addition of stars later than K7 from the γ Vel dataset.
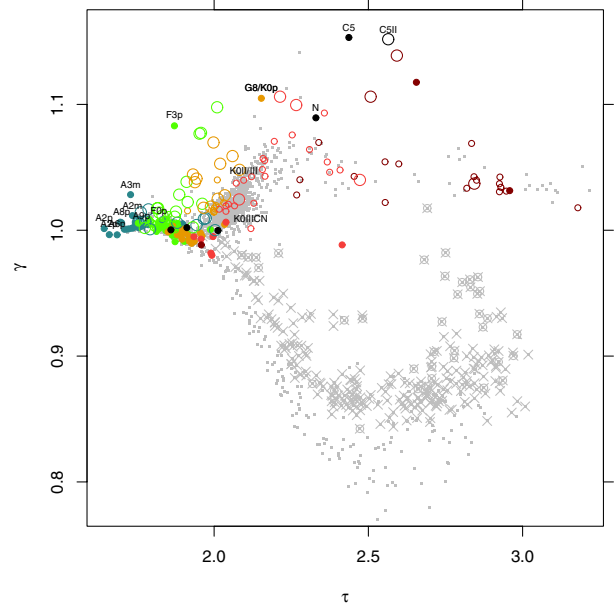
Fig. 38. (γ, τ) diagram for UVES-POP stars, excluding stars earlier than A2. Carbon stars and stars with peculiar spectra are labeled. Symbols as in Fig. 37.

accordingly no datapoint is found in the figure along the M-dwarf strip (gray dots are γ Vel datapoints; gray crosses are γ Vel cluster members), confirming our findings from Sect. 4.1. Interesting in this diagram is also the location of the few KM supergiant stars, along a strip placed still above that occupied by KM giants (which in turn was above the dwarf strip): this shows that the gravity dependence of the combination of (μ_7, μ_6) indices continues monotonically across the whole range of M-star gravities, from dwarfs through giants up to supergiants. The extension to supergiant stars is a new result, which could not have been obtained in Sect. 4.1 because of the lack of M supergiants in the γ Vel dataset. This lack is also suggested by comparing the ranges of β_t values found respectively in the γ Vel and UVES-POP datasets, as discussed above.

We eventually show in Fig. 38 the (γ, τ) diagram for UVES-POP stars, with spectral types later than A2 (gray symbols refer to the γ Vel dataset as above). The lack of UVES-POP dwarf stars later than mid-K is evidently confirmed by the lack of non-gray datapoints in the lower part of the diagram. Noteworthy is the position occupied by some stars with peculiar spectra, with values for γ index mimicking low-gravity stars. FGKM supergiants are found above the locus of dwarfs and giants of the same spectral types, confirming the effectiveness of γ as a gravity index for these stars as well. We note that this does not happen for A-type supergiants (blue circles, near $(\gamma, \tau) = (1, 2)$): the reason for this may be twofold: at these temperatures, the α_w index which is an essential ingredient of temperature index τ starts to depend to gravity, and the metallic lines which contribute to γ become too weak to be an useful gravity indicator. The position of carbon stars (labeled in the figure), near that of KM supergiants is also remarkable, and both these types of stars may account for many of the "outlier" stars mentioned in Sect. 4. The star found in isolation near the center of the diagram (red filled dot in the figure) is the already mentioned S6/8 star HD 115236, in a location not populated by normal dwarfs or giants. In such "suspicious" cases, an accurate examination of the spectrum is
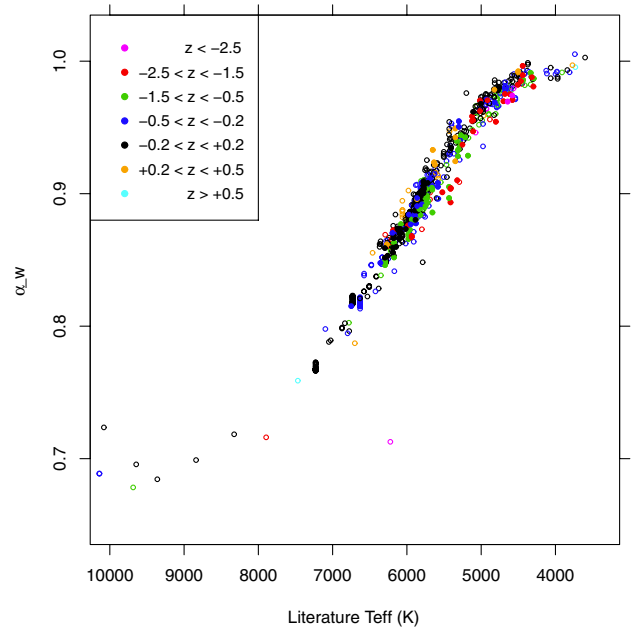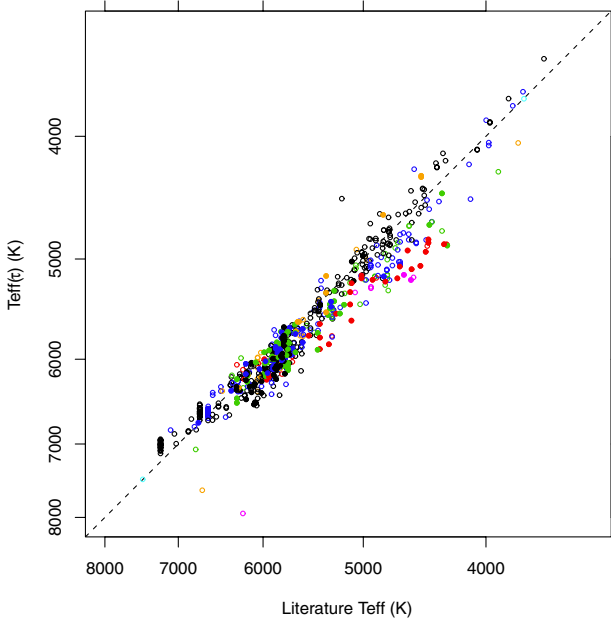

Fig. 39. Index α_w vs. literature $T_{\rm eff}$, for the ELODIE spectra. Datapoints are color-coded according to their metallicity (from literature), as in the legend. Filled dots indicate stars with most reliable determinations of $T_{\rm eff}$ and [Fe/H], while empty dots are stars with less reliable parameters.

needed to ascertain the peculiar nature of the star, while our indices may only provide an initial hint in this direction.

7.2. ELODIE dataset

We examine now results from the ELODIE dataset. We start from a diagram of our index α_w vs. the literature $T_{\rm eff}$ values for ELODIE sample stars (Fig. 39). Here and in the following, we have considered only ELODIE stars with no indication of SB2 status, no "uncertain RV" flag, and without close visual companions possibly contaminating the stellar spectrum. We have

Fig. 40. Effective temperature as derived from index τ (in Sect. 5), vs. literature $T_{\rm eff}$, for the ELODIE spectra. The dashed line represents identity. Symbols as in Fig. 39.

Fig. 41. A $\beta_{\rm t}$ vs. $\alpha_{\rm w}$ diagram, analogous to Fig. 36, for ELODIE spectra. Colored symbols are as in Fig. 39, while gray symbols indicate stars from the γ Vel dataset, as in Fig. 36.

plotted color-coded symbols according to (literature) metallicity $z = $ [Fe/H], choosing seven z ranges (with finer spacing near $z = 0$), as explained in the figure legend; moreover, we use filled dots only for stars having the best-quality flag ($q = 4$) set for both $T_{\rm eff}$ and [Fe/H] in the stellar parameter table accompanying the ELODIE spectra themselves[11]. Empty dots are instead used for all remaining stars, with lower-quality parameter determinations. The ($\alpha_{\rm w}$, $T_{\rm eff}$) diagram of Fig. 39 shows a very good correlation between our $\alpha_{\rm w}$ index and $T_{\rm eff}$, at least on the $T_{\rm eff}$ range 4500–7500 K. This is a confirmation, if ever needed, that the width of Hα line wings is a very good measure of $T_{\rm eff}$ in this range, for all gravities and metallicities. This gives further support to our use of the $\alpha_{\rm w}$ index as a primary temperature indicator, in the above $T_{\rm eff}$ range. $T_{\rm eff}$ standard deviations around a quadratic best-fit line are 105 K for 6000 K $< T_{\rm eff} <$ 7000 K and 116 K for 5000 K $< T_{\rm eff} <$ 6000 K.

Next, in Fig. 40 we plot the effective temperature $T_{\rm eff}(\tau)$ we have derived from the measured values of the τ index on ELODIE spectra and its calibration following KH95 (Sect. 5), vs. literature $T_{\rm eff}$. The agreement is not bad, but inferior with respect to that shown using the $\alpha_{\rm w}$ alone: in this case, standard deviations of the differences between $T_{\rm eff}(\tau)$ and literature $T_{\rm eff}$ are 203 K for 6000 K $< T_{\rm eff} <$ 7000 K, 165 K for 5000 K $< T_{\rm eff} <$ 6000 K, and 213 K for 4000 K $< T_{\rm eff} <$ 5000 K. We recall however, that τ is useful as a $T_{\rm eff}$ indicator over a much wider $T_{\rm eff}$ range than $\alpha_{\rm w}$, so the question whether or not the spread of datapoints in Fig. 40 can be minimized is an important one. We note that the spread around the identity relation (dashed line) seems to be mostly related to differences in metallicity z: the lowest-z stars (red and magenta datapoints) fall mostly below the dashed line, while high-z stars (orange) fall above it. In order to minimize the spread in the diagram, and obtain a more accurate $T_{\rm eff}$ indicator, it is therefore important to be able to estimate z from our HR15n spectra themselves. We
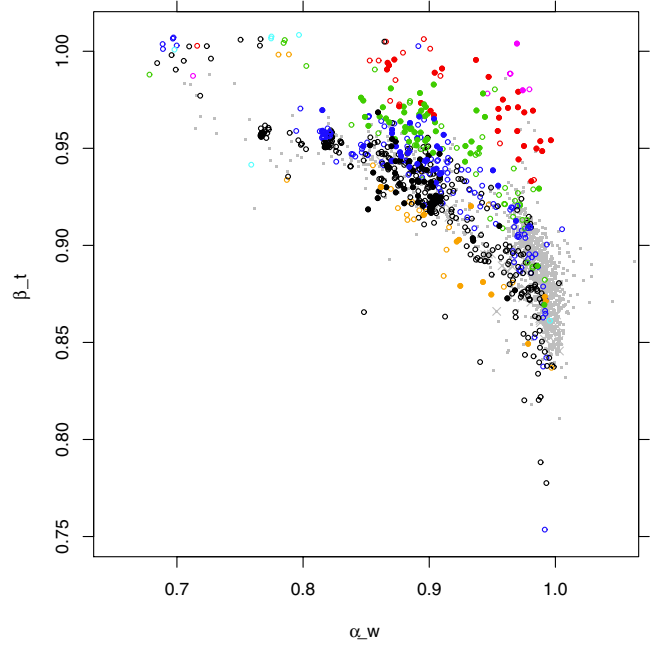
remark that the weak z dependence of $T_{\rm eff}(\tau)$ implies that also index τ (of which $T_{\rm eff}(\tau)$ is a monotonic function) is only slightly depending on z.

We have already assessed that $\alpha_{\rm w}$ is a metallicity-independent index, while it is likely that $\beta_{\rm t}$ is highly z-dependent. The ($\beta_{\rm t}$, $\alpha_{\rm w}$) diagram of Fig. 41 for ELODIE spectra shows this latter fact rather clearly: datapoints of different colors (i.e., z) are distributed in layers, with lower-z stars found at gradually higher values of $\beta_{\rm t}$ than solar-metallicity stars. We discussed above that, at least for luminosity classes V to III, $\beta_{\rm t}$ is practically independent of gravity, so that only the z dependence shifts a star position up- or downwards, for a fixed $T_{\rm eff}$ (and $\alpha_{\rm w}$), except for supergiants. In the specific case of the ELODIE spectra, however, we remarked about the masking of telluric lines, adopted by the authors of the spectral library, having the effect of increasing scatter in the computed values of $\beta_{\rm t}$ (and β) index, which accounts at least partially for the scatter found in Fig. 41. The question is therefore whether another indicator of z can be obtained in the HR15n wavelength range, from a less telluric-contaminated spectrum region.

We therefore consider a new combination of indices, which we define as

$$\zeta = \zeta_1 - \beta_{\rm t}. \tag{14}$$

In this index, the telluric-line effect on $\beta_{\rm t}$ is mitigated by the addition of the telluric-free ζ_1 index. To understand its usefulness as a metallicity indicator, we plot ζ vs. τ in Fig. 42. Index τ was shown above to be only little affected by metallicity; on the contrary, ζ is strongly dependent on z (hence the choice of its name). This statement is of course valid only within the limitations of the ELODIE dataset, since for $\tau \geq 2.1$ ($T_{\rm eff} \leq 4500$ K) very few datapoints are available with known stellar parameter (even less with most reliable parameter determinations - filled dots). In the figure we show also datapoints from the γ Vel dataset (gray) and an analytical approximation $Z(\tau)$ to the locus of solar-metallicity stars (black dots), continued by γ Vel cluster members (gray
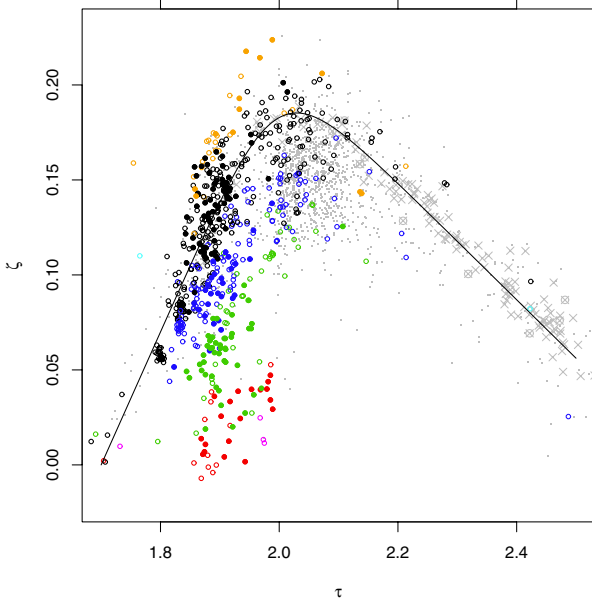
Fig. 42. Index ζ vs. τ for ELODIE spectra with $T_{\rm eff} < 10\,000$ K, and for γ Vel dataset stars. The solid line is an approximate analytic description of the behavior of solar-metallicity ELODIE stars (mostly for $\tau < 2.1$) and of γ Vel cluster members (for $\tau > 2.1$). Symbols as in Fig. 41.
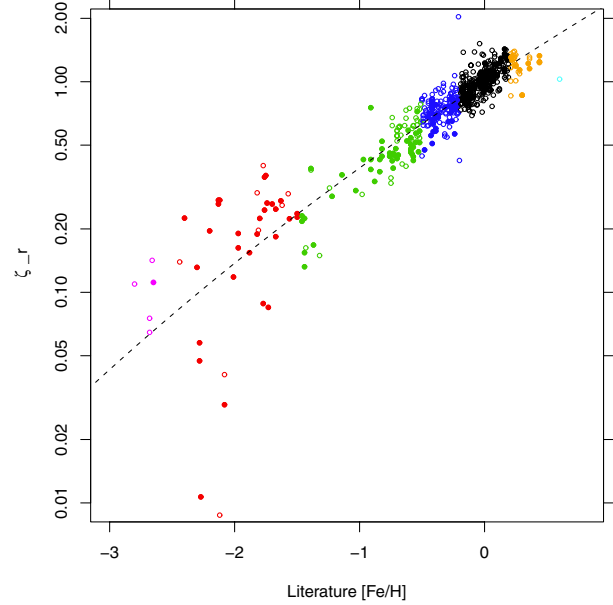
Fig. 43. Ratio ζ_r between measured ζ and the function $Z(\tau)$, vs. literature metallicity $z = $ [Fe/H], for ELODIE spectra with $\tau > 1.8$ ($T_{\rm eff} < 7000$ K). The dashed line is an analytical description of the relation found (see text). Symbols as in Fig. 39.

crosses) at lower temperatures (higher τ). The analytical form of this function is

$$Z(\tau) = \frac{1}{(1/(0.7\tau - 1.19)^5 + 1/(0.825 - 0.308\tau)^5)^{1/5}} \qquad (15)$$

and we define a "ζ ratio" index ζ_r as

$$\zeta_r = \zeta/Z(\tau), \qquad (16)$$

which describes well the weakening of metal lines at lower z values, at least for stars in the $T_{\rm eff}$ range 4500−7500 K, and irrespective of gravity. We explicitly remark that our formulation of function $Z(\tau)$ is a zero-order approximation to the true dependence of ζ on τ for solar-metallicity stars, mostly because of the heterogeneous nature of the ELODIE literature parameters: a much better knowledge of this function (and in turn of the derived index ζ_r) would be obtained from a study of a single-metallicity stellar sample, such as that of a cluster with a richer population of solar-type stars than γ Vel.

The relation between the newly defined index ζ_r and literature metallicity z is shown in Fig. 43, for $\tau > 1.8$ ($T_{\rm eff} < 7000$ K). The dashed line is an analytical approximation of the correlation found, of the form

$$Z_r = (1 + 0.09\,z)^{10}. \qquad (17)$$

At the lowest metallicity values ($z < -2$), Fig. 43 shows a considerable scatter with respect to our analytical approximation, which should be therefore regarded as tentative; however, the still limited tests provided by both the Survey UVES results and the benchmark stars in Sect. 7.4 below show a smaller scatter, and reassure us about the validity of our approximation. Inverting Eq. (17) we have computed new metallicity values $z(\zeta, \tau)$ from ζ and τ, for ELODIE stars with $\tau > 1.8$; standard deviations for the differences $z(\zeta, \tau) - z$ (where z is the literature metallicity) are then found to be 0.68 for $z < -1.5$, 0.22 for $-1.5 < z < -0.5$, and 0.15 for $z > -0.5$. We conclude that our new index ζ_r does indeed provide a good metallicity diagnostics,

at least for stars with $T_{\rm eff} < 7000$ K, and all gravities. We basically lack a suitable reference sample of lower-temperature stars with measured metallicities to properly assess the effectiveness of this index for M stars.

Having established a valid metallicity index, we take advantage of it to attempt a metallicity correction to the $T_{\rm eff}(\tau)$ function obtained in Sect. 5. The needed correction term must be such as to lower the estimated temperature for low-metallicity stars between 4000–5000 K, while leaving unaltered temperatures near 6000 K, for any metallicity (see Fig. 40). An useful empirical expression for the metallicity-corrected temperature $T_{\rm eff}^z(\tau)$ (again, not from a best fit) is found to be

$$T_{\rm eff}^z(\tau) = T_{\rm eff}(\tau) \times 10^{0.00003(1-\zeta_r)(T_{\rm eff}(\tau)-6300)} \qquad (18)$$

with $T_{\rm eff}(\tau)$ and $T_{\rm eff}^z(\tau)$ in units of K. This newly determined temperature is compared in Fig. 44 with literature $T_{\rm eff}$ values: apart from very few outliers (most of which stars without best-quality literature parameters) a good correlation is obtained, with no appreciable systematics related to metallicity. Standard deviations of the differences between $T_{\rm eff}^z(\tau)$ and literature $T_{\rm eff}$ are 230 K for 6000 K $< T_{\rm eff} <$ 7000 K, 175 K for 5000 K $< T_{\rm eff} <$ 6000 K, and 135 K for 4000 K $< T_{\rm eff} <$ 5000 K.

We note that these standard deviations are almost a factor of 2 larger than those found using photometry in Sect. 5. This is surprising, since aside from systematic errors possibly introduced by the adopted KH95 calibration, photometric colors may be affected by reddening (anyway by a small amount, as discussed in Sect. 5). Doubtlessly, the telluric contamination to β_t (and thus to τ and $T_{\rm eff}(\tau)$) increases the spread in our derived $T_{\rm eff}$ for ELODIE stars. Moreover, the heterogeneous assembly of literature data on stellar $T_{\rm eff}$, $\log g$, and z also contribute to the spread in (the abscissa of) Fig. 44, while the photometric $V - I$ colors used in Sect. 5 were all taken from the same source (Jeffries et al. 2009). For all these reasons, it is probably safe to consider, for solar-metallicity stars, the calibration found in Sect. 5 as the most reliable one; for metal-poor (or metal-rich) stars, the metallicity correction introduced above becomes
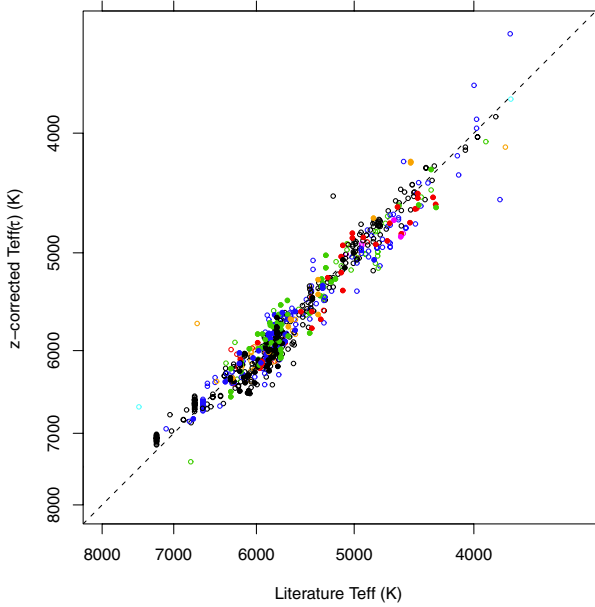
Fig. 44. A diagram analogous to Fig. 40, but showing the metallicity-corrected temperature $T_{\rm eff}^z(\tau)$. Symbols as in Fig. 39.
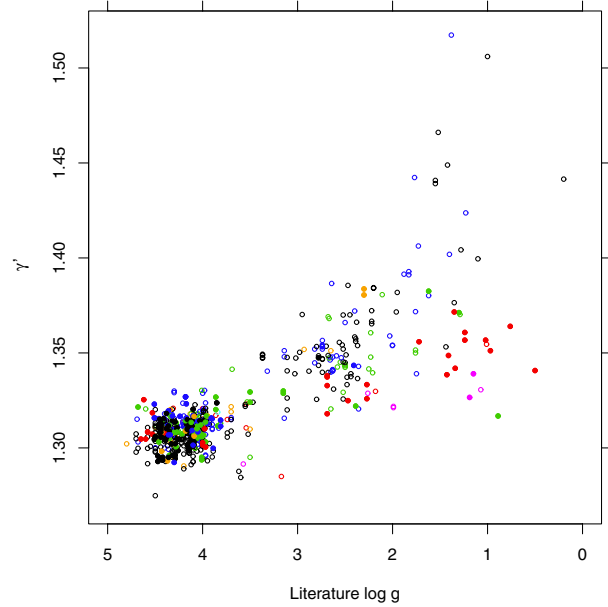
Fig. 46. Composite index γ' vs. literature $\log g$ for ELODIE spectra with $T_{\rm eff} < 10\,000$ K. Symbols as in Fig. 39.
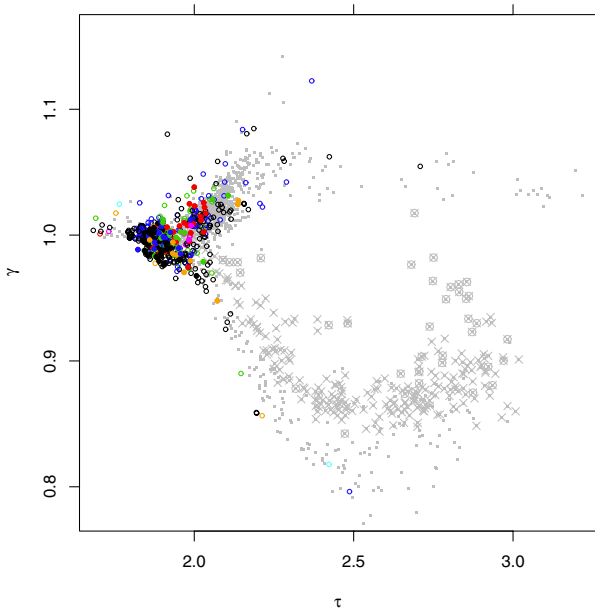
Fig. 45. (γ, τ) diagram for ELODIE stars, excluding stars with literature $T_{\rm eff} > 10\,000$ K, and for γ Vel dataset stars. Symbols as in Fig. 41.

necessary, although it probably results in a less reliable $T_{\rm eff}$ determination compared to solar-metallicity stars.

We now try to calibrate the gravity-sensitive index γ. We remind that $\gamma = \gamma_1 + \beta$, and $\beta = 1 - \beta_{\rm c}/\beta_{\rm t}$. Since both $\beta_{\rm c}$ and $\beta_{\rm t}$ are affected by the telluric-line masking present in ELODIE data, index γ is expected to be affected by more significant scatter with respect to other indices discussed above. Nevertheless, useful information can still be gained from this index for ELODIE spectra. First, in Fig. 45 we show a (γ, τ) diagram for ELODIE stars (with gray symbols referring to the γ Vel dataset). As expected, MS stars later than mid-K ($\tau > 2$ and $\gamma < 0.95$) are only a handful; they fall all near the lower envelope of γ Vel MS stars, i.e. well below the locus populated by cluster PMS stars, in perfect agreement with our results in Sect. 4.6. The number of M giants

is not large either: in fact, it is less than the UVES-POP giants, so that again the two datasets are complementary. The diagram is in agreement with the bulk of ELODIE stars being FGK stars of classes V to III.

To calibrate the dependence of γ on $\log g$, we first observe that MS stars with $1.8 < \tau < 2.0$, with nearly constant $\log g$, do not fall on a line at constant γ, but show a slope in their γ vs. τ locus, indicating that γ depends slightly on temperature, in addition to gravity. Limiting ourselves to F,G, and early-K stars (because of the ELODIE sample composition), we find that a better $T_{\rm eff}$-independent gravity index may be taken as

$$\gamma' = \gamma + \tau/6 \qquad (19)$$

whose dependence on (literature) $\log g$ is shown in Fig. 46. From this latter figure we observe that the scatter of datapoints is fairly large, compared to analogous diagram involving $T_{\rm eff}$ or z, considered above; this was in part expected, as discussed above, because of telluric contamination. But there is also an evident systematic trend with stellar metallicity, as seen from some layering of datapoints with different colors. We therefore attempt again to apply a metallicity correction to γ', based on the metallicity index ζ_r derived above.

We found useful this empirical correction to obtain a metallicity-corrected γ'^z index:

$$\gamma'^z = 1.305 + (\gamma' - 1.305)/\sqrt{\zeta_r}. \qquad (20)$$

The γ'^z index is shown in Fig. 47 vs. literature $\log g$. The main properties of all indices are summarized in Table 2. In the figure, the significant metallicity-related segregation seen in Fig. 46 is no longer visible. Despite the scatter still present, using this diagram it is possible to discriminate effectively between gravities of MS stars, giants, and supergiants, with very few outlier datapoints, irrespective of metallicity. In the figure, a quadratic best fit[12] to the data is also shown. Residuals in $\log g$ around the best-fit curve have standard deviations of 0.437 dex for dwarfs ($\gamma'^z < 1.33$) and 0.88 dex for giants/supergiants ($\gamma'^z > 1.33$).

---

[12] The best-fit formula is $\gamma'^z = 1.4516 - 0.0405 \log g + 0.00153(\log g)^2$.

Table 2. Properties of spectral indices.

Index	Description	Indicator type
$\mu_1 - \mu_7$	TiO and CaH bands	T_{eff} late-type ($\mu7$ also $\log g$)
α_w	Hα wings	T_{eff} early-type, CTTS if $\alpha_w > 1.1$
α_c	Hα core	chromospheres
β_t	metal line "quintet" $\lambda\lambda$ 6493−6500	T_{eff} intermediate type
β_c	low-gravity "quintet" lines	$\log g$
ζ_1	Fe I lines $\lambda\lambda$ 6625–6635	T_{eff} intermediate type
γ_1	low-gravity lines $\lambda\lambda$ 6758–6776	$\log g$
μ	$0.25\,(\mu_1 + \mu_3 + \mu_5 + \mu_7)$	T_{eff} late-type
β	$1 - \beta_c/\beta_t$	$\log g$
τ	$\min(\alpha_w, 1) - \beta_t - \zeta_1 + 3 \times \mu$	T_{eff} all types
γ	$\beta + \gamma_1$	$\log g$ all types
ζ	$\zeta_1 - \beta_t$	metallicity
ζ_r	$\zeta/Z(\tau)$	T_{eff}-corrected metallicity
γ'^z	$1.305 + (\gamma + \tau/6 - 1.305)/\sqrt{\zeta_r}$	T_{eff}- and z-corrected gravity
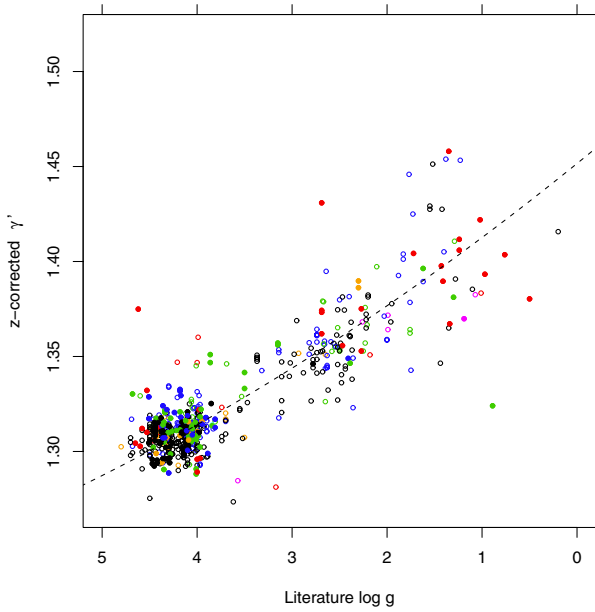
Fig. 47. Diagram analogous to Fig. 46, but using the metallicity-corrected index γ'^z. Symbols as in Fig. 39. The dashed line is a quadratic best fit to the data.
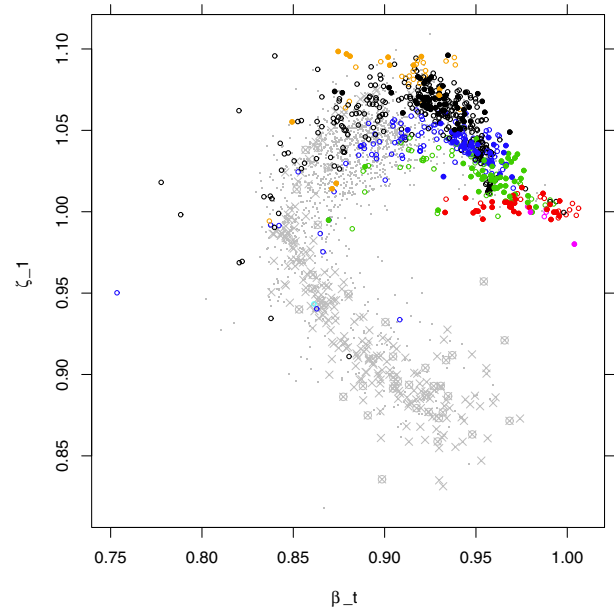
Fig. 48. Diagram of ζ_1 vs. β_t, for ELODIE and γ Vel spectra with $T_{eff} < 10\,000$ K. Symbols as in Fig. 41.

We remark again that these results do not apply to dwarfs later than mid-K, and that some of the spread seen is attributable to telluric-line masking in ELODIE data.

We conclude this section by examining the (ζ_1, β_t) diagram introduced in Sect. 4.4, where its usefulness as a PMS veiling diagnostics was discussed. Such a diagram for ELODIE stars is shown in Fig. 48. From the UVES-POP dataset analysis discussed above, we already know that the few stars to the left of the main locus (especially those with $\beta_t < 0.83$) are probably super-giants, a few of which are also found among ELODIE stars. The layering of stars with different metallicities in the upper part of the diagram is also not a surprise, given the discussion on index ζ above. What is more interesting is that metallicity appears to be the dominant cause for vertical spread of G-K star datapoints near $\beta_t \sim 0.9$, with gravity being only a secondary factor. This same region in the diagram was found in Sect. 4.4 to be populated by giants, with no MS/PMS stars, but there was ambiguity as to whether such a displacement with respect to the MS star locus was a gravity or metallicity effect; from Fig. 48 the dominant role of metallicity is instead evident. Interestingly, when applied

to a constant-metallicity population such as a star cluster, this finding implies that G-K cluster stars are expected to be found only in a narrow strip in this diagram (again, this could not be well tested with γ Vel because of its little population of G-type stars). In a very young cluster, G-K stars are still in their PMS stage, with gravities below those of MS G-K stars, but this will not change their position in this diagram. At the same time, PMS veiling might be present, and it certainly changes the star position in the same diagram. Therefore, the above results strengthen our arguments from Sect. 4.4 that this diagram provides a very useful veiling diagnostics for PMS stars, from G-type to M-type stars.

7.3. Gravity calibration for PMS stars

We mentioned in Sect. 4.6 that late-type PMS stars occupy a region of the $(\log g, T_{eff})$ plane not populated by other classes of normal stars. Therefore, our gravity index could not be calibrated in the range relevant to PMS stars using either ELODIE or UVES-POP stars. We devise here an alternative method to obtain $\log g$ values for the PMS stars, as well as for lower-MS stars.
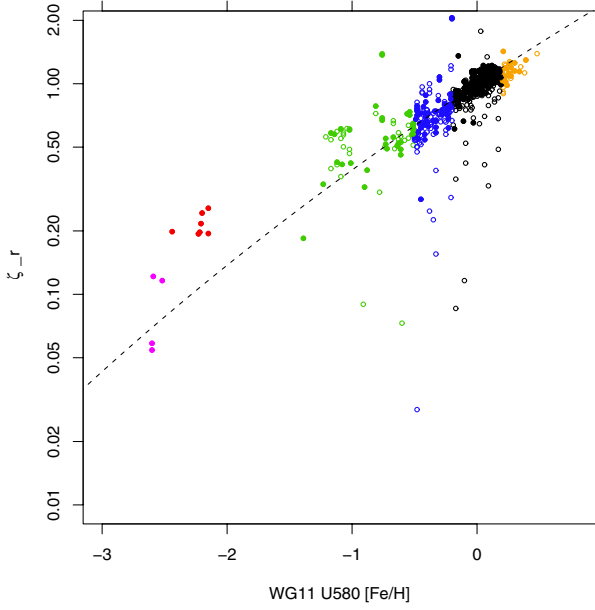
Fig. 49. Index ζ_r for *Gaia*-ESO Survey UVES spectra in the HR15n range, vs. metallicity z = [Fe/H] as derived by WG11 from the complete UVES spectra. Only stars with $\tau > 1.8$ are shown. Dot colors indicate different metallicity ranges, as in Fig. 43. Filled dots correspond to UVES spectra with $S/N > 70$, while empty dots are spectra with $20 < S/N < 70$. The dashed line shows the same relation as in Fig. 43, and is not a best-fit to the UVES data.

The PMS temperature calibration is assumed not to differ from that valid for MS or giant stars, since the τ index was shown above not to depend on gravity.

First, an empirical polynomial fit to the lower MS was derived, for all non-member stars in the γ Vel dataset. The best-fit formula, for all stars with $\gamma < \min(1, 0.565 + 0.2 \times \tau)$, is

$$\gamma_{MS}(\tau) = -116.2025396 + 229.7914669\,\tau - 176.8744508\,\tau^2$$
$$+ 66.8400769\,\tau^3 - 12.4184477\,\tau^4 + 0.9085821\,\tau^5.$$

Then, the following formula gives a good approximation to the expected $\log g$ of members stars in the γ Vel cluster, based on its age and Siess et al. (2000) isochrones (see Fig. 4)

$$\log g_{PMS} = 2.31066 + 2\,(\gamma - 1.03)/(\gamma_{MS}(\tau) - 1.03) \qquad (21)$$

and also its extrapolation to younger PMS stages appears satisfactory. There is however an "interface" region, between these lower-MS and PMS stars, and more massive MS and giant stars, where the two formulations for $\log g$, i.e. that from Eq. (21) and that from the γ'^z best fit, must agree seamlessly. This is achieved by a further correction to the above formula for $\log g_{PMS}$, needed only for stars with $\tau < 2.07$, such that the final expression for $\log g_{PMS}$ for these latter stars becomes

$$\log g_{PMS} = 2\,(\gamma - 1.03)/(\gamma_{MS}(\tau) - 1.03) - 361.637$$
$$+ 350.02806\,\tau - 84.15922\,\tau^2 \qquad (\tau < 2.07).$$

This completes the quantitative calibration of our indices in terms of physical quantities, at least for the range of properties typical of low-mass clusters.

7.4. Other Gaia-ESO Survey data: UVES results, and benchmark stars

In order to test how consistent are the calibrations made with other results being obtained within the Survey, more
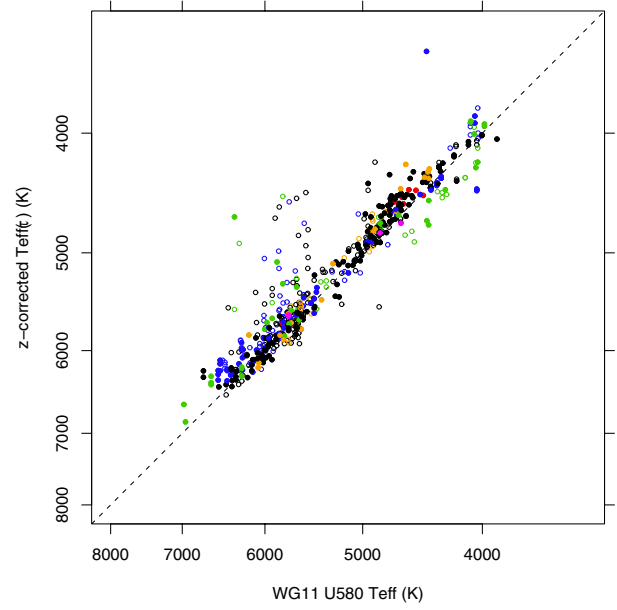
Fig. 50. Metallicity-corrected temperature $T_{\mathrm{eff}}^z(\tau)$ derived by us for *Gaia*-ESO Survey UVES spectra in the HR15n range, vs. T_{eff} as derived by Survey WG11. Symbols as in Fig. 49. The dashed line shows the same relation as in Fig. 44.
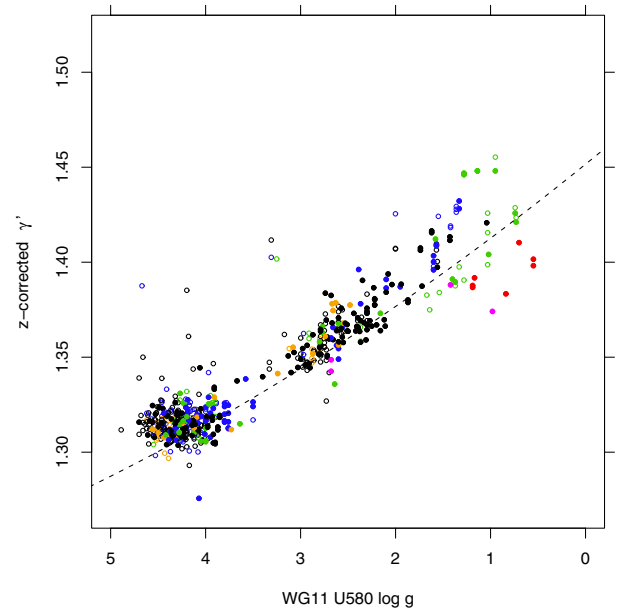

Fig. 51. Metallicity-corrected index γ'^z derived by us for *Gaia*-ESO Survey UVES spectra in the HR15n range, vs. $\log g$ as derived by WG11. Symbols as in Fig. 49. The dashed line shows the same relation as in Fig. 47.

homogeneously than the literature data used thus far, we consider now the sample of all UVES observations (with the 580 nm grating) of *Gaia*-ESO Survey stars, with stellar parameters from internal data release GESiDR1Final, derived from contributions by a large number of consortium members (Working Group WG11, Smiljanic et al., in prep.). As for ELODIE spectra, we have degraded the UVES spectra to the HR15n resolution and wavelength range. Results are shown in Figs. 49–51. Dashed lines in these figures are not best fits to the data, but are the same analytical curves shown in Figs. 43, 44, and 47. The agreement between the calibration based on ELODIE data and the
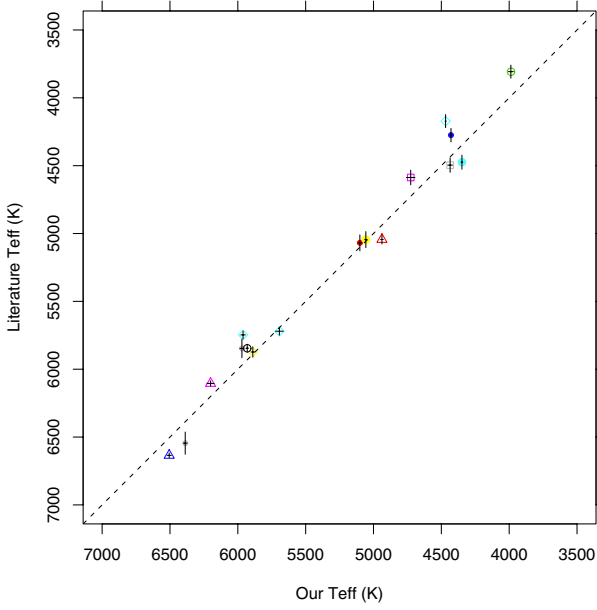
Fig. 52. Comparison of $T_{\rm eff}$ as derived by our method, and literature $T_{\rm eff}$ for *Gaia*-ESO Survey benchmark stars. Dotted line represents identity.
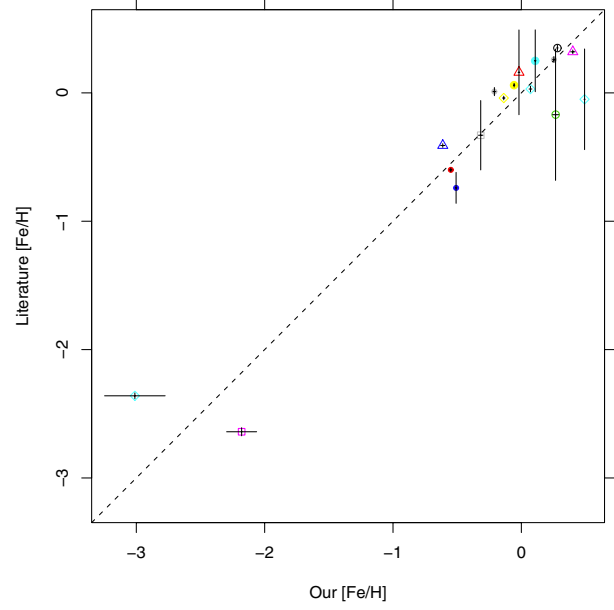
Fig. 54. Comparison of [Fe/H] as derived by our method, and literature [Fe/H] for benchmark stars. Dotted line represents identity.
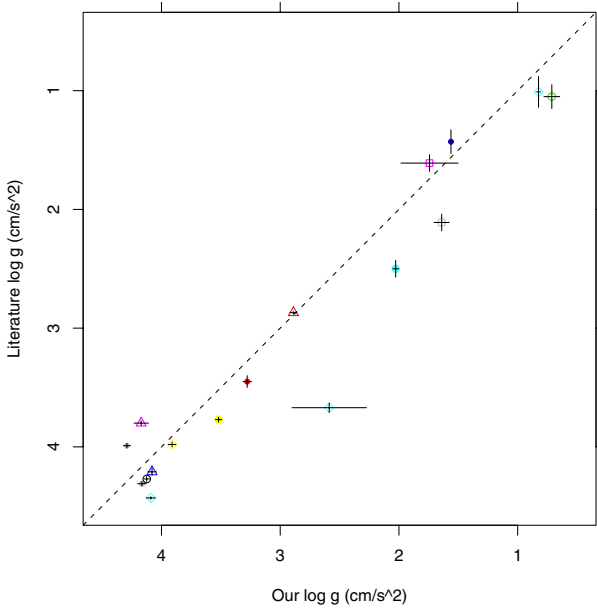
Fig. 53. Comparison of $\log g$ as derived by our method, and literature $\log g$ for benchmark stars. Dotted line represents identity.
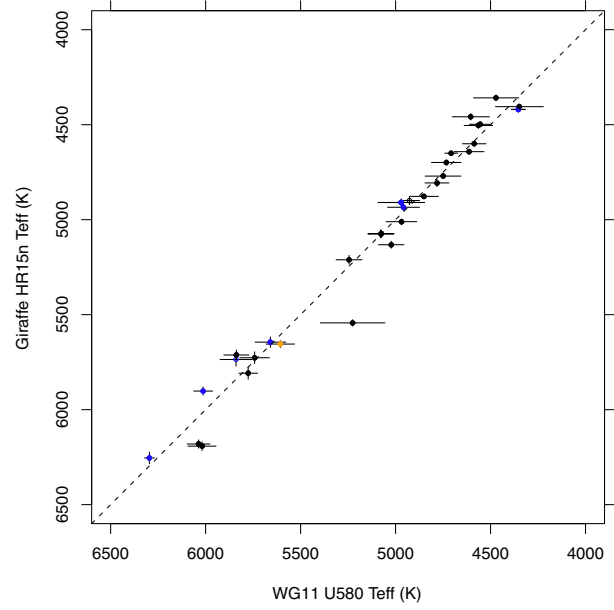
Fig. 55. Comparison between $T_{\rm eff}$ values derived for common UVES and Giraffe targets, respectively by WG11 from UVES data and by our method from Giraffe data. Symbols as in Fig. 49. The dashed line represents identity.

results from UVES is good, especially considering the spectra with highest S/N (>70, filled dots in the figures), and reassures us on the validity of our results.

Eventually, we made a comparison between our derived parameters for *Gaia*-ESO Survey benchmark stars, and their accurate literature values (Heiter et al., in prep.; Jofré et al. 2013, 2014). In the Survey, each benchmark star was observed with all instrument configurations used in the Survey, including HR15n. For each star, we have selected the HR15n spectrum with the highest S/N. Figures 52–54 show the results obtained. The standard deviations of the residuals are 133 K for $T_{\rm eff}$, 0.34 dex for $\log g$ (0.24 dex considering only stars with $z > -1$), and 0.29 dex for [Fe/H] (0.22 dex considering only stars with $z > -1$). We note that some scatter in these values comes from uncertainties

in the parameters of the benchmark stars themselves (e.g., Jofré et al. 2013, 2014), and that the benchmark sample lacks for the moment M dwarfs (Pancino et al., in prep.), for which a smaller $T_{\rm eff}$ uncertainty was estimated in Sect. 5.

7.5. Comparison between UVES and Giraffe results for γ Vel stars

More than 40 stars in the γ Vel dataset were targeted by *Gaia*-ESO Survey observations with both UVES and Giraffe. Such common targets (not necessarily cluster members) are very useful for testing the consistency of results of independent
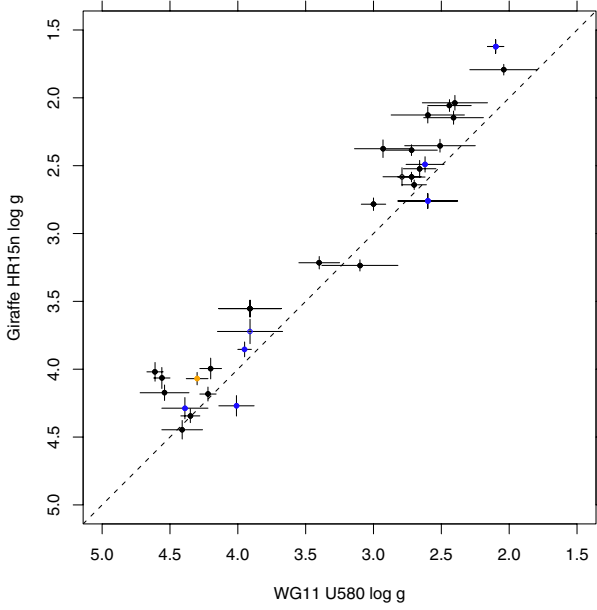
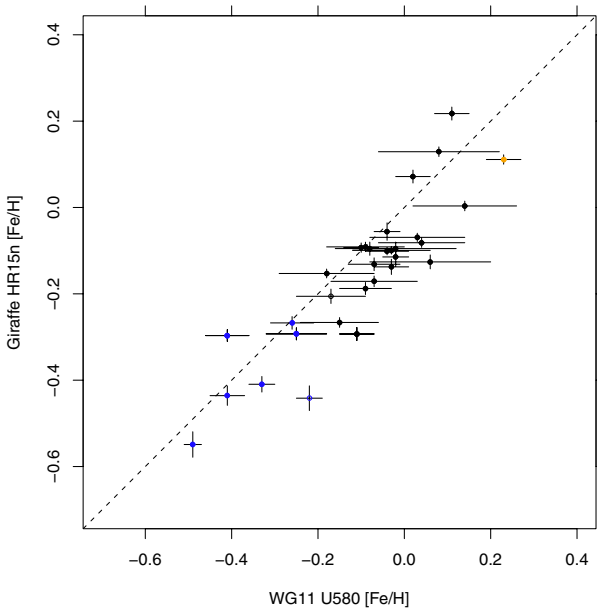**Fig. 56.** Same comparison as in Fig. 55, for log g.

Fig. 57. Same comparison as in Fig. 55, for metallicity z.

analysis of UVES and Giraffe data, as explicitly indicated in the Survey Management Plan. We therefore compare here the results from the UVES data analysis made by WG11 with our results for Giraffe HR15n spectra of the same stars (not of their downgraded-resolution UVES spectra as in Sect. 7.4). Since our method was natively developed for Giraffe HR15n spectra, this test is perhaps more significant than tests made in Sect. 7.4 above. For instance, residual instrumental signatures in the (degraded) UVES data (e.g., imperfect order merging) might have slightly affected results from those tests. The number of common Giraffe-UVES target stars, on the other hand, is significantly smaller than the total number of UVES spectra used in the tests of Sect. 7.4.

We show in Fig. 55 a comparison between the T_{eff} values derived from UVES data by WG11 (34 stars in GESiDR1Final data release) with those derived by our method from HR15n data.

Color coding indicates metallicity according to the UVES results. Figures 56 and 57 show analogous comparisons for log g and metallicity. We find a mean T_{eff} offset (UVES minus Giraffe) of –2 K, and a std.dev. of differences of 92 K. This latter number is slightly smaller than that obtained from benchmark stars (which however span a wider range in all parameters), and well comparable to the std.dev. of fitting residuals obtained in our T_{eff} calibration in Sect. 5 in the same T_{eff} range (110 K for F to mid-G stars, 70 K for mid-G to late-K stars). These uncertainties, consistent across a varied range of T_{eff} calibrations methods (direct measurements for benchmarks, photometry for γ Vel MS/PMS stars, high-resolution UVES data) are therefore robust estimates of the total (statistical plus systematic) errors on T_{eff} delivered by our method.

For log g, the UVES-Giraffe comparison yields a mean offset of 0.21 dex and a std.dev. of differences of 0.21 dex. This latter is again slightly lower than that obtained from metal-rich benchmark stars. Finally, the [Fe/H] mean offset and std.dev. of UVES-Giraffe differences are respectively 0.056 and 0.084: this latter is significantly lower than the corresponding std.dev. using benchmark stars (note however that some of the latter have large errors in their literature metallicity, see Fig. 54).

Despite that the log g and [Fe/H] mean offsets resulting from this comparison are slightly different from zero, we choose not to revise for the moment our calibrations for these quantities, both because of the much smaller number of stars contributing to this test, compared to the ELODIE spectra we used above as calibrators, and also since the *Gaia*-ESO Survey analysis procedures are still evolving and consolidating.

7.6. Tests on clusters as calibrators

Last, we show how the stellar parameters derived from our spectral indices perform for *Gaia*-ESO Survey young clusters. Classically, clusters have been used as calibrators for stellar evolutionary models since they are composed of stars having all (nearly) the same age and metallicity. Analogously, we need here to ensure that the putative members of a given cluster define loci in both the (T_{eff}, log g) and the (T_{eff}, [Fe/H]) diagrams, in reasonable agreement with a single metallicity value, and also with information available from photometry and model isochrones. We therefore show these diagrams, derived using our method on *Gaia*-ESO Survey data from release GESiDR1Final for clusters Chamaeleon I and γ Vel (1–3 Myr and 5–10 Myr, respectively), in Figs. 58 and 59. Blue crosses represent members (from Sect. 2 for γ Vel, from Luhman 2007 for Cha I), and green circles CTTS; only stars with $v \sin i < 50$ km s^{-1} are plotted.

We observe from these figures (left panels) that the median log g of M-type Cha I members is ~3.7, while that of M-type γ Vel members is distinctly higher, being ~4.0. Therefore, our gravity determination does indeed describe the gradual contraction of PMS stars toward the MS, confirming our findings in Sect. 4.6. Moreover, the derived metallicities (right panels) of putative cluster stars (apart from very few outliers of questionable membership) have a sharply peaked distribution, with no (spurious) dependence on T_{eff}. Only a few CTTS members of Cha I deviate from a flat dependence of metallicity on T_{eff}, but this is likely due to the strong veiling affecting these stars' spectra, and weakening their absorption lines. The 1σ width of the derived metallicity distributions for these clusters (robustly determined as the difference between the 84% and 50% quantiles, to minimize the effect of non-member outliers and of veiled spectra) are 0.053 dex for Cha I, and 0.042 dex for γ Vel. These ranges are sensibly smaller than the 1σ scatter found above

(0.22 dex) for metal-rich benchmark stars, leading to at least a legitimate suspicion that the benchmark metallicity scatter is dominated by errors in their literature values rather than by uncertainties in our derivation. Again, this is one more confirmation of the validity of our procedure. The clusters' measured 1σ metallicity scatter is also nearly one-half that found in the UVES-Giraffe common-target comparison of Sect. 7.5, presumably because of the wider range of parameter values covered by these latter stars.

8. Discussion and future prospects

In the previous sections we have defined a set of spectral indices, which enabled us ultimately to place stars in an empirical (γ, τ) diagram, representing a fairly regular mapping of the $(T_{\text{eff}}, \log g)$ plane for intermediate- and late-type stars, for all gravities from the MS up to giants. For this approach to be successful, the indices were carefully selected, on the basis of suitable template spectra from the *Gaia*-ESO γ Vel dataset. This approach is fundamentally different from usual curve-of-growth studies of Fe I/Fe II lines, for which insufficient spectral lines are available in the wavelength range studied here. It is instead more similar to spectral-typing methods, but made quantitative thanks to the use of spectral indices. These were accurately defined to take also advantage of the higher resolution of our spectra, compared to usual low-resolution classification spectra. This compensates the lower number of available diagnostics in the relatively limited wavelength range covered by the HR15n setup. In general, our results falsify the often-made statement that this observational setup is not adequate for spectral classification.

The results presented in this work were made possible in a fundamental way by the extensive parameter-space coverage of the studied stellar sample. Without a combined study of both MS/PMS and giant stars it would have been probably impossible to select, e.g., line ratios most sensitive to gravity.

Since γ Vel contains mostly low-mass, late-type stars, we have devoted particular attention to devise a set of indices which are especially suited to measure temperature and gravity in that mass range. Whether the same indices are equally suited to discriminate satisfactorily, e.g., gravity (age) of more massive stars in a younger cluster, or to discriminate between MS stars, and evolved subgiants and giants in a much older cluster, remains to be studied on the basis of suitable datasets, such as more massive cluster of different ages, some of which are part of the Survey program.

Another little-explored problem is that of heavily-veiled CTTS, which are basically absent in γ Vel. For these stars, we have discussed ways of determining veiling and correct for its effect, but the effectiveness of the procedure still needs to be tested on real veiled spectra, many of which are found among, e.g., Chamaeleon I member stars in the *Gaia*-ESO GESiDR1Final data release. We should also note that in clusters immersed in an H$_{\text{II}}$ region, the nebular (narrow) Hα emission often masks completely any narrow (chromospheric) emission from the cluster stars. This probably prevents the use of the α_c index as a tool for selection of chromospherically active stars. Actual tests on such type of clusters are needed to effectively understand the useability of α_c under these circumstances.

One extremely interesting application of the present work is the study of non-accreting stars in PMS clusters, since the locus occupied by the PMS band in the (γ, τ) diagram is expected to change as a function of age, especially at the youngest ages. The (γ, τ) diagram might therefore become a very useful, distance-independent age indicator, complementing those already existing such as the Li abundance. The comparison

between the γ Vel and Cha I (γ, τ) diagrams, shown in Sect. 7.6, agrees with their expected age dependence.

Observations of older clusters, instead, are important to define as accurately as possible the MS locus in the (γ, τ) diagram, without any possible contribution from PMS stars. This would greatly help to define the region in the diagram where MS stars are not to be found, and only very young/PMS stars may be found.

We have repeatedly noted the presence of outliers in several of our index-index diagrams for the γ Vel dataset. Their positions in the respective diagrams are not due to statistical errors in the indices used (maximum errors are carefully reported for each index), but are instead directly related to some spectral peculiarities with respect to the bulk of other stars (either cluster or field stars). By comparison with index values for stars in the UVES-POP dataset, it is likely that they are chemically peculiar stars, supergiants, and carbon (or carbon-enhanced) stars. In this respect, spectral peculiarities involving an excess abundance of barium (barium stars, but also several types of carbon-enhanced stars) are easily spotted by our index β, sampling the Ba II $\lambda6496.897$ line. A study of the performances of our indices based on a much more varied sample of peculiar stars from, e.g., the Tomasella et al. (2010) spectral atlas is being made, and will be presented in a future work.

9. Summary

We have studied a large set of stellar spectra in the γ Vel cluster region, all taken within the *Gaia*-ESO Survey with VLT/Giraffe setup HR15n. Our immediate aim was to derive basic parameters (T_{eff}, $\log g$, veiling, CTTS indicators) for low-mass cluster stars; at the same time, we tried to address the more general issue of finding useful spectroscopic indicators of fundamental parameters for stars observed with the same resolution and wavelength range.

To this aim, we have defined a number of spectral indices, with the following characteristics:

1. Molecular indices: seven indices $\mu_1 - \mu_7$, sampling the most important TiO molecular-band jumps in HR15n, plus an average TiO index μ derived from them, which is a good T_{eff} indicator for late-type stars.
2. Hα indices: two indices, α_w and α_c, sampling respectively the Hα wings and core, either in absorption (for early-type T_{eff} determination) or in emission as CTTS/accretion indicator (α_w), or chromospheric indicator (α_c).
3. 6490–6500 Å "quintet" indices: two indices, β_t and β_c, sampling respectively the entire group ("quintet") of strong lines near 6495 Å, and its "core"; a difference index β is then derived, highly sensitive to gravity over a wide spectral-type range, while β_t is a good T_{eff} indicator for intermediate-type stars.
4. 6625–6635 Å temperature index: an index ζ_1 from the ratio of suitable Fe I lines, useful as additional T_{eff} measure for intermediate-type stars.
5. 6760–6775 Å gravity index: an index γ_1, sampling a set of lines strongly sensitive to gravity for intermediate-type and late-type stars.

Most notably, two global indices were computed from the above indices: index τ, sensitive to temperature across the whole spectral-type range spanned by our stars, and a gravity-sensitive index γ. Using these indices we are able to place stars in a (γ, τ) diagram, which enables us to discriminate rather clearly
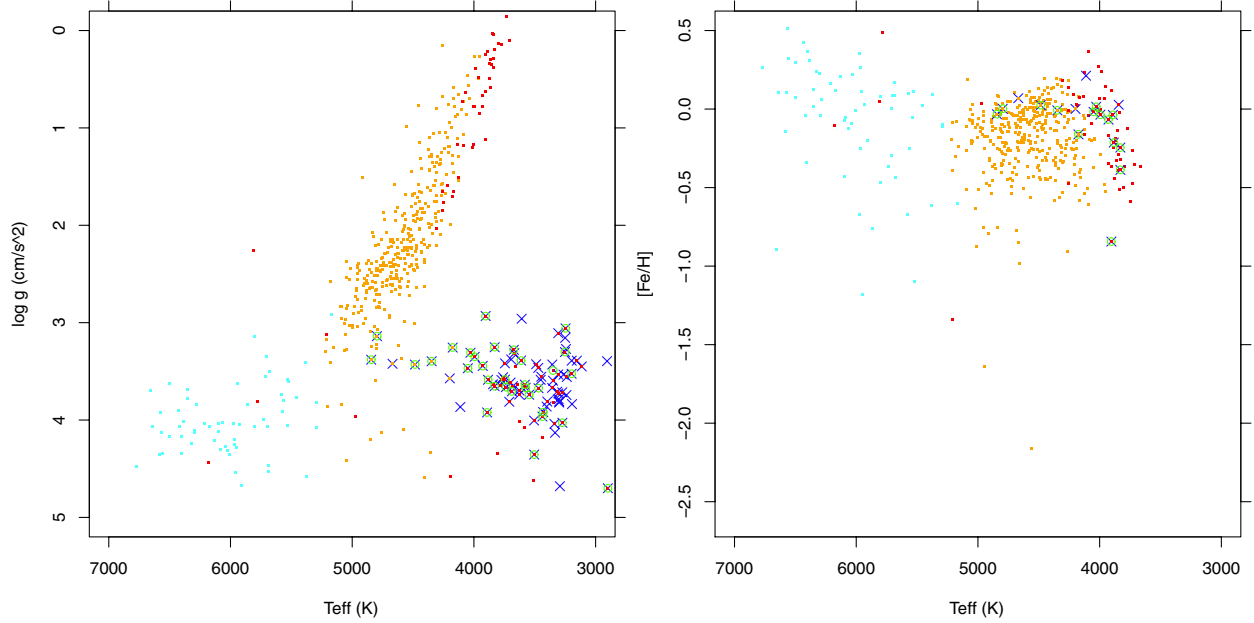
Fig. 58. Diagrams for Chamaeleon I: *left*: $(T_{eff}, \log g)$ diagram. *Right*: $(T_{eff}, [Fe/H])$ diagram. Symbols have the same meaning as in Fig. 1. Blue crosses are cluster members from Luhman (2007). The few datapoints with plotted color not matching their derived T_{eff} values are probable or confirmed peculiar stars.
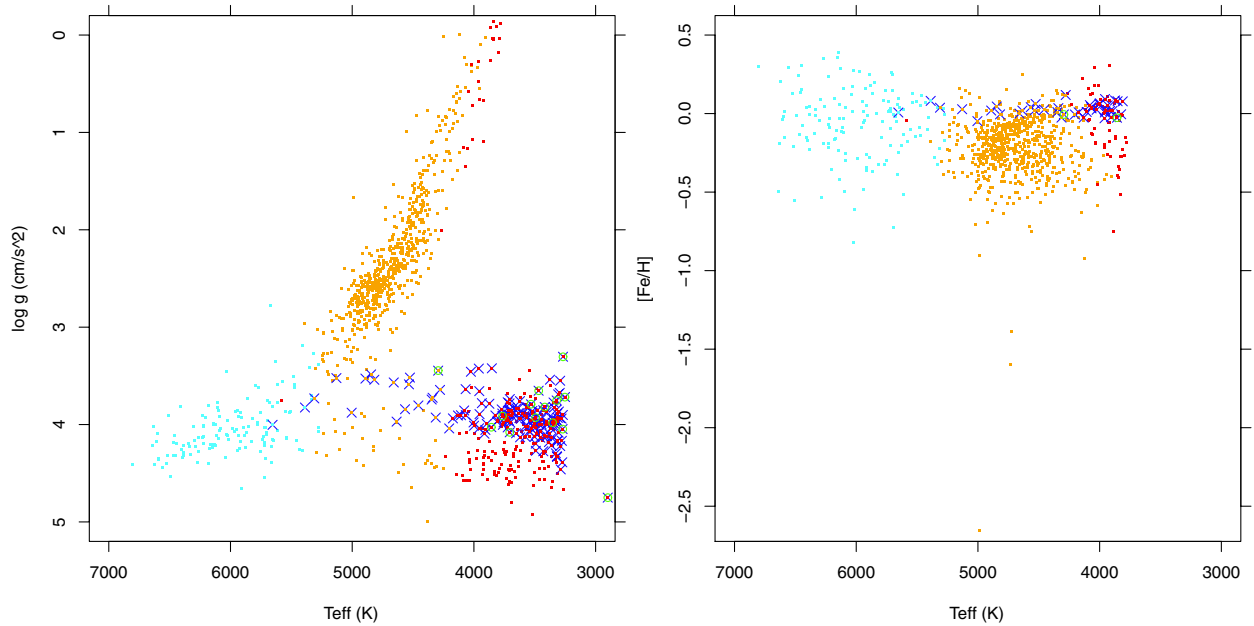
Fig. 59. Same as Fig. 58, for the γ Vel cluster. Symbols have the same meaning as in Fig. 58.

MS from PMS stars (at the γ Vel cluster age), and even more strongly from giant stars, through the intermediate- and low-mass range. This diagram is a new, useful diagnostic tool when applied to young PMS low-mass stars, both to assess membership, and as an empirical age indicator.

We have initially calibrated our τ index on the basis of the widely used KH95 calibrations and observed $V - I_c$ colors. For MS/PMS stars in the γ Vel dataset, the best-fit calibration yielded 1σ errors on T_{eff} on the order of 110 K for early-type stars (hotter than ~5500 K), 73 K for intermediate-type stars (4300–5500 K), and 50 K for late-type stars (colder than 4300 K).

Moreover, comparison with the literature stellar parameters of stars in the ELODIE dataset has enabled us to calibrate

quantitatively the temperature and gravity dependence of our indices in the general case, and to introduce a new composite index ζ, effective to measure stellar metallicity z. Limitations posed by the stellar composition of the ELODIE dataset remain for the low-mass stellar range, and the problem of calibrating our gravity index in the late-K and M-star range was therefore solved by using theoretical Siess et al. (2000) isochrones for γ Vel member stars.

Extensive tests using current *Gaia*-ESO Survey results from UVES observations of a large number of stars spanning a wide range of parameters, as well as using *Gaia*-ESO Survey benchmark stars, strengthen the validity of our calibrations. Typical 1σ errors on $\log g$ determinations were found to be of 0.2 dex,

and on metallicity [Fe/H] of 0.08 dex, for solar-like metallicities. The consistency of our calibrations was also checked against *Gaia*-ESO Survey observations of young clusters with very good results: the rms metallicity scatter for members is always found to be much less than the above 1σ error, derived using non-metallicity-homogeneous star samples as reference. We find that our method is able to provide gravity measurements for low-mass PMS stars, of sufficient accuracy to infer gravity-based ages for PMS clusters (or relative ages at least).

As a first test of the usefulness of our indices, we find that six stars in the γ Vel dataset, showing PMS characteristics and falling much nearer to the ZAMS in the CMD than the bulk of cluster members, are also characterized by a higher gravity than these latter according to our indices, supporting that they are older PMS stars. This conclusion is also strengthened by their systematically lower Li EW with respect to the bulk of cluster member stars, well compatible with an older age. We consider this a rather strong evidence of a previous generation of stars, now dispersed in the field.

We have also discussed areas of possible improvement in the technique, such as extension to higher-mass and older clusters, and a better understanding of the effect of veiling in CTTS.

References

Bagnulo, S., Jehin, E., Ledoux, C., et al. 2003, The Messenger, 114, 10
Biazzo, K., Randich, S., Palla, F., & Briceño, C. 2011, A&A, 530, A19
Boehm-Vitense, E. 1989, Introduction to Stellar Astrophysics (Cambridge, New York: Cambridge University Press), 1989
Briceño, C., Hartmann, L., Stauffer, J., & Martín, E. 1998, AJ, 115, 2074
D'Orazi, V., Randich, S., Flaccomio, E., et al. 2009a, A&A, 501, 973
D'Orazi, V., Magrini, L., Randich, S., et al. 2009b, ApJ, 693, L31
D'Orazi, V., Biazzo, K., Desidera, S., et al. 2012, MNRAS, 423, 2789
Gilmore, G., Randich, S., Asplund, M., et al. 2012, The Messenger, 147, 25
Girardi, L., Williams, B. F., Gilbert, K. M., et al. 2010, ApJ, 724, 1030
Gray, R. O., & Corbally, C. J. 2009, Stellar Spectral Classification, eds. R. O. Gray, & Ch. J. Corbally (Princeton University Press)
Hernández, J., Hartmann, L., Calvet, N., et al. 2008, ApJ, 686, 1195
Jaschek, C., & Jaschek, M. 1990, The Classification of Stars, eds. C. Jaschek, & M. Jaschek (Cambridge, UK: Cambridge University Press), 427
Jeffries, R. D., Oliveira, J. M., Barrado y Navascués, D., & Stauffer, J. R. 2003, MNRAS, 343, 1271
Jeffries, R. D., Naylor, T., Walter, F. M., Pozzo, M. P., & Devey, C. R. 2009, MNRAS, 393, 538
Jeffries, R. D., Jackson, R. J., Cottaar, M., et al. 2014, A&A, 563, A94
Jofré, P., Heiter, U., Blanco-Cuaresma, S., & Soubiran, C. 2013 [arXiv:1312.2943]
Jofré, P., Heiter, U., Soubiran, C., et al. 2014, A&A, 564, A133
Kenyon, S. J., & Hartmann, L. 1995, ApJS, 101, 117
Kirkpatrick, J. D., Henry, T. J., & McCarthy, D. W., Jr. 1991, ApJS, 77, 417
Lawson, W. A., Lyo, A.-R., & Bessell, M. S. 2009, MNRAS, 400, L29
Luhman, K. L. 2007, ApJS, 173, 104
Lyo, A.-R., Lawson, W. A., & Bessell, M. S. 2004, MNRAS, 355, 363
Lyo, A.-R., Lawson, W. A., & Bessell, M. S. 2008, MNRAS, 389, 1461
Marigo, P., Girardi, L., Bressan, A., et al. 2008, A&A, 482, 883
Mohanty, S., Basri, G., Jayawardhana, R., et al. 2004, ApJ, 609, 854
Padgett, D. L. 1996, ApJ, 471, 847
Pozzo, M., Jeffries, R. D., Naylor, T., et al. 2000, MNRAS, 313, L23
Prugniel, P., & Soubiran, C. 2001, A&A, 369, 1048
Reid, I. N., Hawley, S. L., & Gizis, J. E. 1995, AJ, 110, 1838
Riddick, F. C., Roche, P. F., & Lucas, P. W. 2007, MNRAS, 381, 1067
Santos, N. C., Melo, C., James, D. J., et al. 2008, A&A, 480, 889
Shkolnik, E., Liu, M. C., & Reid, I. N. 2009, ApJ, 699, 649
Siess, L., Dufour, E., & Forestini, M. 2000, A&A, 358, 593
Skumanich, A. 1972, ApJ, 171, 565
Spina, L., Randich, S., Palla, F., et al. 2014, A&A, submitted
Stauffer, J. R., Schild, R., Barrado y Navascues, D., et al. 1998, ApJ, 504, 805
Tomasella, L., Munari, U., & Zwitter, T. 2010, AJ, 140, 1758

[1] INAF – Osservatorio Astronomico di Palermo G.S.Vaiana, Piazza del Parlamento 1, 90134 Palermo, Italy
e-mail: damiani@astropa.inaf.it
[2] INAF – Osservatorio Astrofisico di Arcetri, Largo E. Fermi 5, 50125 Florence, Italy
[3] Institute of Astronomy, University of Cambridge, Madingley Road, Cambridge CB3 0HA, UK
[4] Centre for Astrophysics Research, STRI, University of Hertfordshire, College Lane Campus, Hatfield AL10 9AB, UK
[5] Astrophysics Group, Research Institute for the Environment, Physical Sciences and Applied Mathematics, Keele University, Keele, Staffordshire ST5 5BG, UK
[6] Royal Observatory of Belgium, 3 avenue circulaire, 1180 Brussels, Belgium
[7] Instituto de Astrofísica de Andalucía, Camino Bajo de Huétor 50, 18008 Granada, Spain
[8] Lund Observatory, Department of Astronomy and Theoretical Physics, Box 43, 221 00 Lund, Sweden
[9] INAF – Osservatorio Astronomico di Bologna, via Ranzani 1, 40127 Bologna, Italy
[10] Dipartimento di Fisica e Astronomia, Sezione Astrofisica, Università di Catania, via S. Sofia 78, 95123 Catania, Italy
[11] ASI Science Data Center, via del Politecnico SNC, 00133 Roma, Italy
[12] Laboratoire Lagrange (UMR 7293), Université de Nice Sophia Antipolis, CNRS, Observatoire de la Côte d'Azur, BP 4229, 06304 Nice Cedex 4, France
[13] European Southern Observatory, Karl-Schwarzschild-Str. 2, 85748 Garching bei München, Germany
[14] Department for Astrophysics, Nicolaus Copernicus Astronomical Center, ul. Rabiańska 8, 87-100 Toruń, Poland